GEORG-AUGUST-UNIVERSITÄT
GÖTTINGEN

Fakultät für
Physik

Master's Thesis

Rekonstruktionsoptimierung des Prozesses $H \to \tau\tau$ am ATLAS Experiment

Optimisation of the reconstruction of the $H \to \tau\tau$ process in the ATLAS experiment

prepared by

Lukas Weise

from Kassel

at the II. Physikalischen Institut

Thesis number: II.Physik-UniGö-MSc-2015/04

Thesis period: 1st April 2015 until 30th September 2015

First referee: Prof. Dr. Arnulf Quadt

Second referee: Prof. Dr. Stan Lai

Zusammenfassung

Der Massenrekonstruktionsalgorithmus Missing Mass Calculator (MMC) ist ein wichtiges Werkzeug für die Bestimmung der invarianten di-τ Masse im $H \to \tau\tau$ Prozess. In dieser Arbeit werden die zugrundeliegenden Winkelverteilungen des MMC neu parametrisiert. Dabei wird die Parametrisierung für die unterschiedlichen Zerfallskanäle des τ Leptons getrennt durchgeführt. Die neue Parametrisierung führt zu keiner Verbesserung der Auflösung der rekonstruierten Masse im Vergleich zur bisher genutzten Parametrisierung, verbessert aber den rekonstruierten Zentralwert dieser.
Weiterhin wird in dieser Arbeit der wichtige irreduzible Untergrund des $H \to \tau\tau$ Prozesses, $Z \to \tau\tau$, untersucht. Der Wirkungsquerschnitt dieses Untergrundes wird im semi-leptonischen Zerfallskanal bei einer Schwerpunktsenergie von $\sqrt{s} = 13\,\text{TeV}$ gemessen. Dazu werden die ersten Daten des Run II des LHC mit einer integrierten Luminosität von $\mathcal{L}_{int} = 85\,\text{pb}^{-1}$ verwendet. Das Ergebnis der Messung in einem MMC-Massenfenster von $60\,\text{GeV} \leq m_{MMC} \leq 140\,\text{GeV}$ ist $\sigma_{tot} = 2180 \pm 260\,\text{(stat.)}\,^{+500}_{-500}\,\text{(sys.)} \pm 250\,\text{(lumi.)}\,\text{pb}$ im Muon-Kanal und $\sigma_{tot} = 1990 \pm 170\,\text{(stat.)}\,^{+280}_{-280}\,\text{(sys.)} \pm 220\,\text{(lumi.)}\,\text{pb}$ im Elektron-Kanal. Die theoretische Vorhersage ist konsistent mit diesen Messwerten.

Abstract

The di-τ mass reconstruction algorithm Missing Mass Calculator (MMC) is crucial for any $H \to \tau\tau$ analysis. In this thesis a new parametrisation of one key component of MMC, the angular distributions, is presented. The parametrisation is performed separately for the different decay modes of the τ lepton. This new parametrisation is found to provide no improvement of the MMC mass resolution with respect to the previously used parametrisation. However, the peak position of the reconstructed mass is slightly better. Moreover, the cross section of $Z \to \tau\tau$, the most important irreducible background to $H \to \tau\tau$, is measured at $\sqrt{s} = 13\,\text{TeV}$ in the semi-leptonic channel. This measurement uses the first $\sqrt{s} = 13\,\text{TeV}$ data of LHC Run II, corresponding to an integrated luminosity of $\mathcal{L}_{int} = 85\,\text{pb}^{-1}$. The cross section results for a MMC mass window of $60\,\text{GeV} \leq m_{MMC} \leq 140\,\text{GeV}$ are $\sigma_{tot} = 2180 \pm 260\,\text{(stat.)}\,^{+500}_{-500}\,\text{(sys.)} \pm 250\,\text{(lumi.)}\,\text{pb}$ in the muon channel and $\sigma_{tot} = 1990 \pm 170\,\text{(stat.)}\,^{+280}_{-280}\,\text{(sys.)} \pm 220\,\text{(lumi.)}\,\text{pb}$ in the electron channel. The theoretical prediction is found to be consistent with these results.

Contents

Nomenclature

Variables

Variable	Meaning
$\vec{p}_T$	transverse momentum with respect to beam (z) axis, $p_T = \lvert\vec{p}_T\rvert$
$m^2 = E^2 - \vec{p}^{\,2}$	(squared) invariant mass for momentum $\vec{p}$ und energy E

Relations

γ,β:	$\gamma = (1-\beta^2)^{-1/2}$ with: $\beta = \lvert\vec{\beta}\rvert = \frac{\lvert\vec{v}\rvert}{c}$
Pauli matrices:	$\sigma_1 = \begin{pmatrix} 0 & 1 \\ 1 & 0 \end{pmatrix}$ $\sigma_2 = \begin{pmatrix} 0 & -i \\ i & 0 \end{pmatrix}$ $\sigma_3 = \begin{pmatrix} 1 & 0 \\ 0 & -1 \end{pmatrix}$
commutator:	$[\sigma_l, \sigma_k] = 2i \sum_{m=1}^{3} \epsilon_{lkm}\sigma_m$
anticommutator:	$\{\sigma_l, \sigma_k\} = 2\delta_{lk}\mathbb{1}_2$
γ matrices:	$\gamma^0 = \begin{pmatrix} \mathbb{1}_2 & 0 \\ 0 & -\mathbb{1}_2 \end{pmatrix}$ $\gamma^i = \begin{pmatrix} 0 & \sigma_i \\ -\sigma_i & 0 \end{pmatrix}$ with: $i \in \{1,2,3\}$
adjoint spinor:	$\overline{\psi} = \psi^t\gamma^0$

Indices

Greek indices	Lorentz indices 0,1,2,3 (summing convention)
Latin indices	Euclidean indices 1,2,3 (summing convention)

Abbreviations

Abbreviation	**Meaning**
MC	Monte Carlo
MMC	Missing Mass Calculator
SM	Standard Model
EM	electromagnetic
sys.	systematic
stat.	statistic
lumi.	luminosity
CERN	European Organization of Nuclear Research
LHC	Large Hadron Collider
LEP	Large Electron Positron Collider
SLAC	Stanford Linear Accelarator Center
SPS	Super Proton Synchrotron
HERA	Hadron-Elektron-Ring-Anlage
DESY	Deutsches Elektronen Synchrotron
L1	Level 1 trigger
2d	two-dimensional
HLT	High Level Trigger
BDT	Boosted Decision Tree
PDF	Parton Density Function
RMS	Root Mean Square
TES	Tau Energy Scale
JES	Jet Energy Scale
JER	Jet Energy Resolution
LO	leading order
NLO	next-to-leading order
NNLO	next-to-next-to-leading order
xpyn	τ lepton decay mode: x charged pions, y neutral pions
ℓ	electron or muon
Prob.	Probability

1. Introduction

The Higgs boson was discovered by ATLAS and CMS at the LHC in July 2012 [1, 2]. But the observed direct couplings were all bosonic. To test if the discovered particle is indeed the Standard Model Higgs boson, the establishment of the fermionic couplings is required. The most promising channel for an observation is $H \to \tau\tau$, since the QCD background is much smaller than for $H \to b\bar{b}$ and the Higgs branching ratio into $\tau\tau$ is the second largest among the accessible fermions. Using Run I data, ATLAS reached a significance of 4.5σ (observed) [3]. After the upgrade phase of LHC and ATLAS, and the start of Run II an early observation of this decay is expected. The fermionic coupling is only the first of various Standard Model tests that need to be performed and can possibly lead to new physics.

Because of the change of center-of-mass energy, the detector and the analysis framework for Run II, tools used already in Run I have to be prepared for Run II. For example mass reconstruction algorithms need to be adjusted to the new conditions. This is one focus of this thesis.

A good understanding of the $H \to \tau\tau$ backgrounds, especially the irreducible ones, is a requirement for a $H \to \tau\tau$ analysis. Therefore, these backgrounds have to be studied at 13 TeV . The most important $H \to \tau\tau$ background is $Z \to \tau\tau$. Consequently, a $Z \to \tau\tau$ analysis is performed in the semi-leptonic channel to provide a fiducial cross section measurement on the first recorded data.

2. Theory

2.1. Standard Model

The Standard Model (accompanied by the Higgs mechanism) describes all (observed) fundamental particles and their interactions except for gravity. Those particles are shown in Figure 2.1.

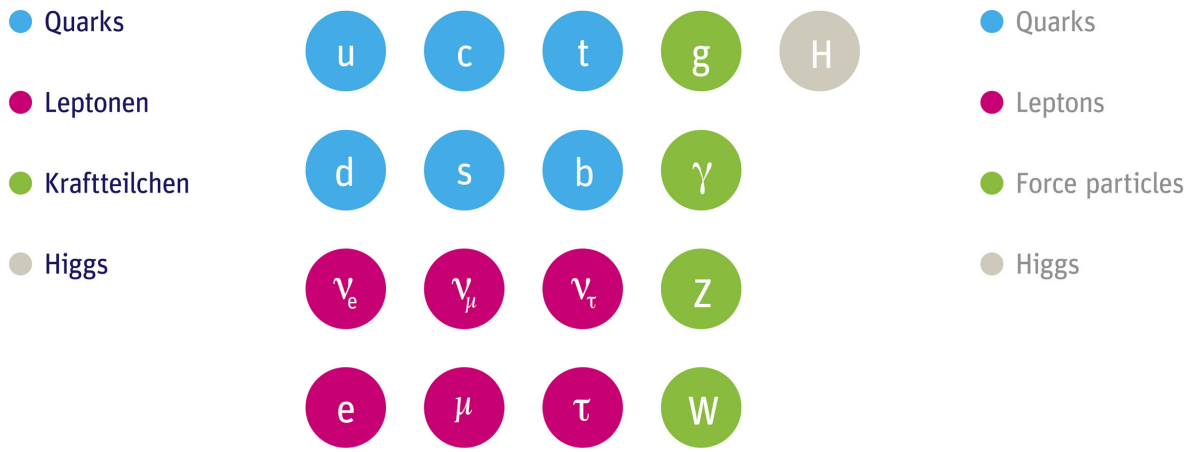

Figure 2.1.: SM fundamental particles.

Particles with half-integer spin (fermions) such as quarks and leptons are grouped into three generations (first three colums in Figure 2.1), which differ only by mass. The left-handed (eigenvalue -1 of $\gamma^5 = i\gamma^0\gamma^1\gamma^2\gamma^3$) component of charged and uncharged lepton as well as the left-handed component of up-type and down-type quark can be grouped into isospin doublets. For every particle there is an antiparticle with opposite sign of electromagnetic charge, but same mass and spin. Interactions between particles are mediated by gauge bosons which carry integer spin.

Strong interaction: The strong interaction is mediated by eight massless gluons (g) and acts between particles with colour charge. Those are quarks (colours red, green and blue), antiquarks (colours antired, antigreen, antiblue) and the gluons themselves carrying

one colour and one anticolour. Since only colourless particles can be observed, the quarks form bound states (hadrons): baryons (three quarks or three antiquarks) or mesons (quark and antiquark).

Electromagnetic interaction: All particles, that carry electric charge, interact via the electromagnetic force mediated by the massless and neutral photon γ. While up-type quarks carry a charge of $^2/_3$ and down-type quarks $^{-1}/_3$, the charged leptons electron (e^-), muon (μ^-), tau (τ^-) have a charge of -1.

Weak interaction: All fundamental fermions including neutrinos ν interact via the weak interaction. The gauge bosons of this interactions are the electrically neutral Z^0 boson and the charged $W^\pm$ bosons. All of the weak gauge bosons are massive.

2.2. Local gauge invariance

Quantum field theory uses the Langrangian formalism to infer the equations of motion of particle fields. The action S is defined like in classical mechanics

$$S = \int \mathrm{d}t L \quad , \tag{2.1}$$

where L denotes the Lagrange function and is given by

$$L = \int \mathrm{d}^3 x \mathcal{L}(\phi, \partial_\mu \phi) \quad . \tag{2.2}$$

However, the Lagrangian density $\mathcal{L}$ (called Lagrangian from now on) depends on the field ϕ and its derivatives.
The equations of motion (Euler Lagrange equations) for the field ϕ can then be deduced by minimizing S

$$0 = \partial_\mu \left(\frac{\partial \mathcal{L}}{\partial(\partial_\mu \phi)} \right) - \frac{\partial \mathcal{L}}{\partial(\phi)} \quad . \tag{2.3}$$

If the Lagrangian depends on multiple fields, one obtains such an equation for every field. As in classical mechanics Noether's theorem provides a conserved quantity for every continuous symmetry of the action $\phi \to \phi + \alpha \Delta\phi$.
If local gauge invariance is postulated, meaning invariance under the transformation $\phi \to \phi + \alpha(x)\Delta\phi$ with space-time dependent α, an interaction mediating gauge field is needed. This is illustrated by the following example.

Photon example The Lagrangian $\mathcal{L}_{Dirac}$ of the free fermion field is [4]

$$\mathcal{L}_{Dirac} = \bar{\psi}(i\gamma^\mu \partial_\mu - m)\psi \quad . \tag{2.4}$$

This is obviously invariant under the global transformation $\psi \to \exp(i\alpha)\psi$, but not under the local one $\psi \to \exp(i\alpha(x))\psi$. But this local gauge invariance can be induced if one replaces the partial derivative ∂_μ by the covariant $D_\mu = \partial_\mu - ig_e A_\mu$. The gauge field A_μ has to transform in the following way: $A_\mu \to A_\mu + 1/g_e \partial_\mu \alpha(x)$. Inserting this in the Lagrangian (2.4) one obtains the Lagrangian of quantum electrodynamics (QED) $\mathcal{L}_{QED}$. Additionally a kinetic term $\mathcal{L}_A = -1/4 F^{\mu\nu}F_{\mu\nu}$ for the gauge boson A_μ with the field strength tensor $F_{\mu\nu} = \partial_\mu A_\nu - \partial_\nu A_\mu$ is needed

$$\mathcal{L}_{QED} = \mathcal{L}_{Dirac} - \frac{1}{4}F^{\mu\nu}F_{\mu\nu} + \bar{\psi} g_e \gamma^\mu A_\mu \psi \quad . \tag{2.5}$$

The third term of equation (2.5) describes the actual electromagnetic interaction, the interaction of the photon A_μ with the fermion ψ.

The weak interaction arises if one postulates invariance under $\psi \to \exp(i\alpha(x)\tau_j)\psi$ with $\tau_j = 1/2\ \sigma_j$ [4]. The τ_j matrices generate the group SU(2). Accordingly, this group is called gauge group of the weak interaction. The gauge group of the strong interaction (quantum chromodynamics QCD) is SU(3), generated by the Gell-Mann matrices [4]. Since the gauge group of QED is U(1), the Standard Model in short notation reads SU(3)⊗SU(2)⊗U(1).
Because mass terms would spoil the concept of local gauge theory, the Standard model cannot explain the particles masses. This is done by the Higgs mechanism (see section 2.5).

2.3. Quantum chromodynamics

The Lagrangian of Quantum Chromodynamics is of the same form as the QED one [4]

$$\mathcal{L}_{QCD} = \sum_q \overline{\psi}_q (\gamma^\mu D_\mu - m)\psi_q - \frac{1}{4} G^a_{\mu\nu} G^{\mu\nu}_a \quad . \tag{2.6}$$

The covariant derivative is here $D_\mu = \partial_\mu - ig_s \lambda_a \mathcal{A}^a_\mu$ with the gluon fields $\mathcal{A}^a_\mu$, the Gell-Mann matrices λ_a ($a \in \{1, 2, ..., 8\}$) and the three dimensional vectors of colour charged

spinors ψ. $G_{\mu\nu}$ denotes the field strength tensor of QCD, which in contrast to the QED one is $G^a_{\mu\nu} = \partial_\mu \mathcal{A}^a_\nu - \partial_\nu \mathcal{A}^a_\mu + g_s f^{abc} \mathcal{A}^b_\mu \mathcal{A}^c_\nu$ with f^{abc} being the structure constants of SU(3) given by $[\lambda^a, \lambda^b] = i f^{abc} \lambda_c$. This additional term reflects the non-Abelian structure of SU(3) and leads to cubic and quartic gluon couplings.
Since higher (than tree level) processes usually lead to divergences, the measured couplings and the masses of particles are assumed to already account for these processes, so that the bare quantities diverge. Therefore, the coupling constant is energy dependent. For the strong coupling $\alpha_s = \frac{g_s^2}{4\pi}$, the leading order dependence is [4]

$$\alpha_s = \frac{\alpha_s(\mu^2)}{1 + \frac{(33-2n_f)\alpha_s(\mu^2)}{12\pi} \ln \frac{Q^2}{\mu^2}} \quad , \tag{2.7}$$

where n_f is the number of accessible quark flavours at the momentum transfer Q and μ is the renormalisation scale. For six or less quark flavours the coupling decreases in Q. This behaviour is caused by the different impact of quark and gluon loops.
The energy dependence of the coupling leads to asymptotically free quarks at small distances or high energies. For large distances or low energy the potential of the interaction grows, so that the creation of a new $q\overline{q}$ becomes energetically favoured. This effect is called confinement.
As a consequence perturbation theory cannot be applied for small Q. Thus, phenomenological models are needed to describe QCD processes at low energies. For example the splitting of high energetic quarks or gluons can only be calculated pertubatively down to a particular energy scale. The further fragmentation or hadronisation then relies on models for combining partons (quarks, gluons) into colourless hadrons. Important fragmentation models are string and cluster fragmentation. The measurable object arising from this shower of QCD particles is then called jet.

2.4. Electroweak interaction

Electrodynamics and weak interaction can be combined in a unified theory [5]. For this purpose one starts with four gauge fields W_1^μ, W_2^μ, W_3^μ and B^μ[1] and the Lagrangian [4]

$$\mathcal{L}_{EW} = \overline{\Psi_L}(\gamma^\mu D^L_\mu - m)\Psi_L + \overline{\psi_R}(\gamma^\mu D^R_\mu - m)\psi_R - \frac{1}{4} W^j_{\mu\nu} W_j^{\mu\nu} - \frac{1}{4} B^j_{\mu\nu} B_j^{\mu\nu} \quad . \tag{2.8}$$

[1] Those fields are not exactly the fields of the electroweak gauge bosons, see section 2.5.

The fields W_i^μ only couple to left-handed isospin doublets Ψ_L, whereas B^μ couples to right-handed singlets ϕ_R, too. The covariant derivative is defined as

$$D_\mu = \partial_\mu - igW_\mu^a \tau_a - i\frac{g'}{2}B_\mu \quad , \tag{2.9}$$

where g and g' are different coupling constants.
Since the quarks' mass eigenstates are different from the weak eigenstates, the quark type (flavour) can change in a charged weak interaction. The relationship of mass eigenstates q and weak ones q' is described by the Cabibbo-Kobayashi-Maskawa (CKM) matrix

$$\begin{pmatrix} d' \\ s' \\ b' \end{pmatrix} = \begin{pmatrix} V_{ud} & V_{us} & V_{ub} \\ V_{cd} & V_{cs} & V_{cb} \\ V_{td} & V_{ts} & V_{tb} \end{pmatrix} \begin{pmatrix} d \\ s \\ b \end{pmatrix} \quad , \tag{2.10}$$

where $V_{q_1 q_2}$ denotes the coupling coefficient of the quarks q_1 and q_2.

2.5. Higgs mechanism

The Higgs mechanism was developed by Peter Higgs and others in 1964 [6]. It introduces a doublet $\Phi = \begin{pmatrix} \phi^+ \\ \phi^0 \end{pmatrix}$ of complex scalar fields with potential $\mathcal{V} = -\mu^2 \Phi^\dagger \Phi + {}^{\lambda}\!/_{2}(\Phi^\dagger \Phi)^2$. For $\mu^2 < 0$ this potential has minima at $\Phi^\dagger \Phi = {}^{v^2}\!/_{2} = {}^{-\mu^2}\!/_{2\lambda}$, whereas at $\Phi^\dagger \Phi = 0$ it has a local maximum. In order to get a stable solution, Φ can be expanded at a minimum

$$\Phi_0 = \begin{pmatrix} 0 \\ {}^{v}\!/_{\sqrt{2}} \end{pmatrix} \tag{2.11}$$

and the fluctuations from the vacuum value Φ_0 expressed in terms of the fields $\theta_{1,2,3}(x)$ and $H(x)$

$$\Phi = \begin{pmatrix} \theta_2 + i\theta_1 \\ {}^{1}\!/_{\sqrt{2}}(v + H) - i\theta_3 \end{pmatrix} \quad . \tag{2.12}$$

At lowest order in the fields one finds

$$\Phi = \exp(i\theta_a {}^{\tau_a}\!/_{v}) \begin{pmatrix} 0 \\ {}^{1}\!/_{\sqrt{2}}(v + H) \end{pmatrix} \quad . \tag{2.13}$$

Since the potential is gauge invariant, the exponential can be canceled by a $SU(2)$ gauge transformation, so that

$$\Phi = \begin{pmatrix} 0 \\ 1/\sqrt{2}(v+H) \end{pmatrix} \quad . \tag{2.14}$$

This gauge is called unitary gauge. While the potential is gauge invariant, choosing a particular ground state breaks gauge invariance. This is called spontaneous symmetry breaking.

Masses of the electroweak gauge bosons: Now one can expand the kinetic term $|D_\mu \Phi|^2$ of the scalar field Φ at the minimum Φ_0 using the electroweak covariant derivative specified in expression (2.9)

$$|D_\mu \phi|^2 = \frac{1}{2}(\partial_\mu \phi)^2 + \frac{1}{2}\frac{(v+H)^2}{4}\left(g^2(W_\mu^1)^2 + g^2(W_\mu^2)^2 + (-gW_\mu^3 + g'B_\mu)^2\right) \quad . \tag{2.15}$$

Choosing the following linear combinations of W_1^μ, W_2^μ, W_3^μ, B^μ to be the gauge fields of the electroweak bosons, one obtains the mass terms of the bosons ($\frac{1}{2}m_P^2(\overline{P}_\mu P^\mu)$ with antiparticle $\overline{P}_\mu$ for boson P_μ)

$$\begin{array}{lcc} \text{W bosons:} & W_\mu^\pm = \frac{1}{\sqrt{2}}(W_\mu^1 \mp iW_\mu^2) & m_W = \frac{gv}{2} \\ \text{Z boson:} & Z_\mu = \frac{1}{\sqrt{g^2+g'^2}}(gW_\mu^3 - g'B_\mu) & m_Z = \sqrt{g^2+g'^2}\frac{v}{2} \\ \text{photon:} & A_\mu = \frac{1}{\sqrt{g^2+g'^2}}(g'W_\mu^3 + gB_\mu) & m_\gamma = 0 \end{array}$$

The photon is the orthogonal to Z boson and as intended massless. The linear combinations of W_μ^3 and B_μ can also be described as a rotation by the Weinberg angle θ_W among those fields, so that photon and Z boson can be written as

$$\begin{pmatrix} Z \\ A \end{pmatrix} = \begin{pmatrix} \cos\theta_W & -\sin\theta_W \\ \sin\theta_W & \cos\theta_W \end{pmatrix} \begin{pmatrix} W \\ B \end{pmatrix} \quad . \tag{2.16}$$

With this angle, the mass relation of W and Z boson is $m_Z \cos\theta_W = m_W$ and the coupling constants are connected by $g_e = g\sin\theta_W = g'\cos\theta_W$.
Since the masses of the weak bosons are large, the coupling strength of these bosons is dominated by the propagator. The energy dependence of the electromagnetic coupling constant, however, is similar to the one of the strong coupling. In contrast to the latter, only fermion loops are possible (Abelian structure of QED). Thus, the coupling constant

increases with the energy.

The rest of equation (2.15) describes the Higgs field and the coupling of this to the electroweak bosons. Expanding the potential at the minimum results in $V(\Phi) = \lambda v^2 H^2 + \lambda v H^3 + \frac{\lambda}{4} H^4$. From the quadratic term in H one can read off the Higgs mass $m_H = \sqrt{2\lambda} v$, whilst cubic and quartic terms describe Higgs self interaction. Whereas the vacuum expectation value $v = (\sqrt{2} G_F)^{-1/2}$ is constrained by the Fermi constant G_F, the Higgs mass is a free parameter.
To reach equation (2.14), a SU(2) gauge transformation has been performed. The remaining degrees of freedom, seeming to disappear in this step, are absorbed in the longitudinal polarisation of the massive gauge bosons.

2.5.1. Yukawa couplings

To generate fermion (spinor f) mass terms of the form

$$m\overline{f}f = \frac{m}{4} f^\dagger((1-\gamma^5) + (1+\gamma^5))\gamma^0((1-\gamma^5) + (1+\gamma^5))f \tag{2.17}$$

$$= m\overline{f}_L f_R + m\overline{f}_R f_L \quad , \tag{2.18}$$

one can add terms of the following type to the Langrangian [7]

$$-\lambda_e \overline{E}_L \Phi e_R - \lambda_d \overline{Q}_L \Phi d_R - \lambda_u \overline{Q}_L i\sigma^2 \Phi^* u_R + h.c. \quad , \tag{2.19}$$

where E and Q are lepton and quark doublet spinors and e, u and d the respective singlets. λ is the Yukawa coupling of the respective fermion. Expanding around the minimum Φ_0 obtains, for example for the τ lepton,

$$\frac{-\lambda_\tau}{\sqrt{2}} \begin{pmatrix} \overline{\nu}_\tau & \overline{\tau}_L \end{pmatrix} \begin{pmatrix} 0 \\ v+H \end{pmatrix} \tau_R + h.c. = \frac{-\lambda_\tau}{\sqrt{2}} (v+H) \overline{\tau}_L \tau_R + h.c. \tag{2.20}$$

$$\Rightarrow m_\tau = \lambda_\tau \frac{v}{\sqrt{2}} \quad . \tag{2.21}$$

2.6. Pertubation theory

If the coupling constant α of an interaction is smaller than one, processes with a large number of interaction vertices contribute less than the ones with a small number of vertices since every interaction vertex contributes one factor of α. Therefore, the calculation of an observable can be ordered in powers of α so that every term in the series contributes

less than the previous one. The leading order (LO) contribution is the first non-zero term in this series. Analogous next-to-leading order (NLO) and next-to-next-to-leading order (NNLO) corrections are calculated. Because of the rapidly increasing complexity, corrections are only calculated up to finite order.

2.7. Hadron collider physics

2.7.1. Cross sections

At hadron colliders, the hard interaction takes place between the constituents (partons) of the hadrons. Thus, knowledge on the structure of the hadron is required to calculate the cross section for the complete interaction. This knowledge is encoded in parton density functions $f(x_i, \mu)$. These functions describe the probability to find a parton i with momentum fraction x_i of the hadrons momentum. μ is the energy at which the measurement of the PDF was performed. Among many other measurements fixed target experiments, deep inelastic scattering measurements at the ep collider HERA at DESY [8] and inclusive jet cross section measurements at the TEVATRON [9] contribute to the determination of the parton density functions for protons. With the a hard scattering cross section $\hat{\sigma}_{ij\to XY}$ of partons i and j the cross section of the process $pp \to XY$ is given by the convolution with the PDFs

$$\sigma(pp \to XY) = \sum_{ij} \int \mathrm{d}x_i \int \mathrm{d}x_j f(x_i, \mu) f(x_j, \mu) \hat{\sigma}_{ij\to XY}(x_i, x_j, s x_i x_j, \alpha_s(\mu), \mu) \tag{2.22}$$

where $\sqrt{s}$ is the center-of-mass energy. This formula is also known as the QCD factorisation theorem.
If processes are simulated at a small order (SO) in QCD, the cross section can be corrected to a higher order (HO) by applying a k-factor to scale the event rate

$$k = \frac{\sigma_{HO}}{\sigma_{SO}} \quad . \tag{2.23}$$

This combines a more accurate cross section with a simpler and hence faster event simulation.

2.7.2. Pile-up and underlying event

In one bunch crossing of hadron bunches multiple interactions can take place. This effect is called in-time pile-up for interactions from the same bunch crossing and out-of-time pile-

up for interactions from neighbouring bunch crossings. In ATLAS, the pile-up is simulated by Monte Carlo (MC) generators. However, the mean number of interactions per bunch crossing is not constant. Therefore MC samples need to be reweighted according to the actual mean number of interactions. This procedure is called pile-up reweighting.
Further interactions, that are not part of the hard scattering process, are called underlying event. This includes multi-parton interaction, interaction with beam remnants. Phenomenological models are necessary to describe the underlying event. The multi-parton interaction model, for example, is tuned to data.

3. Phenomenology

3.1. τ lepton

The τ lepton was discovered 1975 at SLAC in $e^+e^- \to \mu^+e^-$ events [10]. It decays within $\tau_\tau = (290.6 \pm 1.0) \cdot 10^{-15}$ s [11] via the weak interaction. Due to its large mass ($m_\tau = (1776.82 \pm 0.16)$ MeV [11]) not only leptonic but also hadronic decays into light mesons (pions and kaons) are possible. The branching fraction of the most important decay modes are given in Table 3.1. Hadronic decay modes are categorised according to the number of charged particles into "1 prong" and "3 prong". All of the decay modes involve at least one neutrino.

Decay mode		Branching ratio [%]
leptonic	$\nu_\tau\nu_\mu\mu^-$	17.41 ± 0.04
	$\nu_\tau\nu_e e^-$	17.83 ± 0.04
1 charged hadron "1 prong"	$\nu_\tau\pi^-$	10.83 ± 0.06
	$\nu_\tau\pi^-\pi^0$	25.52 ± 0.09
	$\nu_\tau\pi^-2\pi^0$	9.30 ± 0.11
3 charged hadron "3 prong"	$\nu_\tau2\pi^-\pi^+$	8.99 ± 0.06
	$\nu_\tau2\pi^-\pi^+\pi^0$	4.62 ± 0.06

Table 3.1.: Most dominant τ^- decay modes [11].

3.2. Higgs boson production

The Higgs boson production cross sections at the LHC at 13 TeV are given in Table 3.2. The dominant production modes are the gluon fusion (ggH, Figure 3.1a) and the vector boson fusion (VBF, Figure 3.1b). Associated production, together with W/Z boson or $t\bar{t}$, is less dominant. While gluon fusion has the highest cross section, vector boson fusion exhibits some nice features. In the case of VBF, two quarks from different protons emit a vector boson (W or Z), which fuse to produce the Higgs boson. Because the quarks do not interact strongly, there is no colour connection between those. For this reason, the quarks form independent, very forward jets leaving a gap with almost no central jet

activity. These features are very helpful from the analysis point of view since one can search for two very forward jets with a gap containing the signal decay products.

Production process	Cross section [pb]
Gluon fusion	$43.92^{+4.51}_{-4.36}$
VBF	$3.748^{+0.123}_{-0.123}$
WH	$1.380^{+0.032}_{-0.027}$
ZH	$0.8696^{+0.0382}_{-0.0382}$
$t\bar{t}H$	$0.5085^{+0.0534}_{-0.0652}$

Table 3.2.: Dominant Higgs boson production cross sections at $\sqrt{s} = 13$ TeV at LHC for $m_H = 125$ GeV . The cross sections are derived as described in [12]. Uncertainties arise from the QCD scale, the PDF of the proton and α_s.

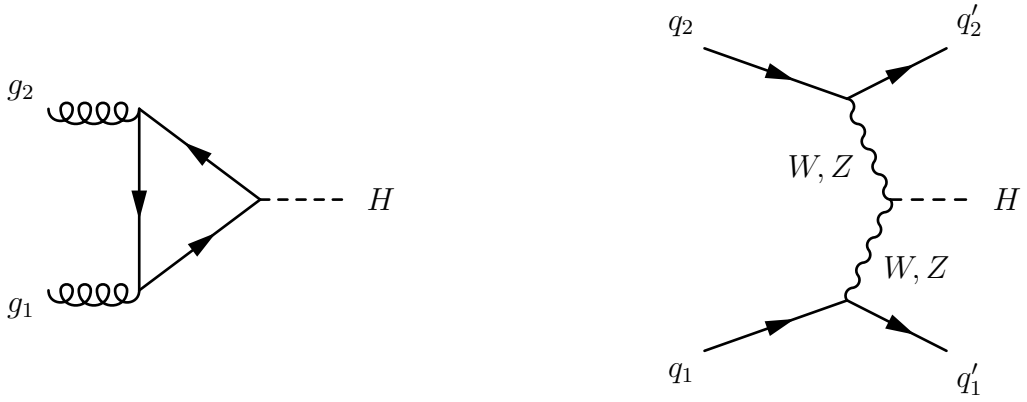

(a) Gluon fusion. ***(b)*** Vector boson fusion.

Figure 3.1.: Leading order Feynman diagrams for Higgs boson production.

3.3. Higgs boson decay

The Higgs boson decay modes with their branching ratio are depicted in Figure 3.2. At a mass of $m_H = 125$ GeV the most dominant one is the decay into a pair of b-quarks, $b\bar{b}$. At the LHC, this final state is experimentally difficult to observe because of the large QCD-multi-jet background. The decay modes WW and ZZ have been used to directly infer the bosonic Higgs coupling. Since the photon cannot couple to the Higgs boson directly in the SM, the observed signal strength of H $\rightarrow \gamma\gamma$ can only be explained, if one assumes fermionic Higgs coupling in an intermediate fermionic loop. However, this is only an indirect evidence. The most promising decay channel for the observation of direct fermionic couplings is therefore the decay into a pair of τ leptons.
Unfortunately the mass reconstruction for a decay into more than one τ lepton is difficult because the τ lepton decays involve at least one neutrino in the final state. In

order to resolve the ambiguity in such an underconstrained system, sophisticated mass reconstruction algorithms are needed (see section 7.1).

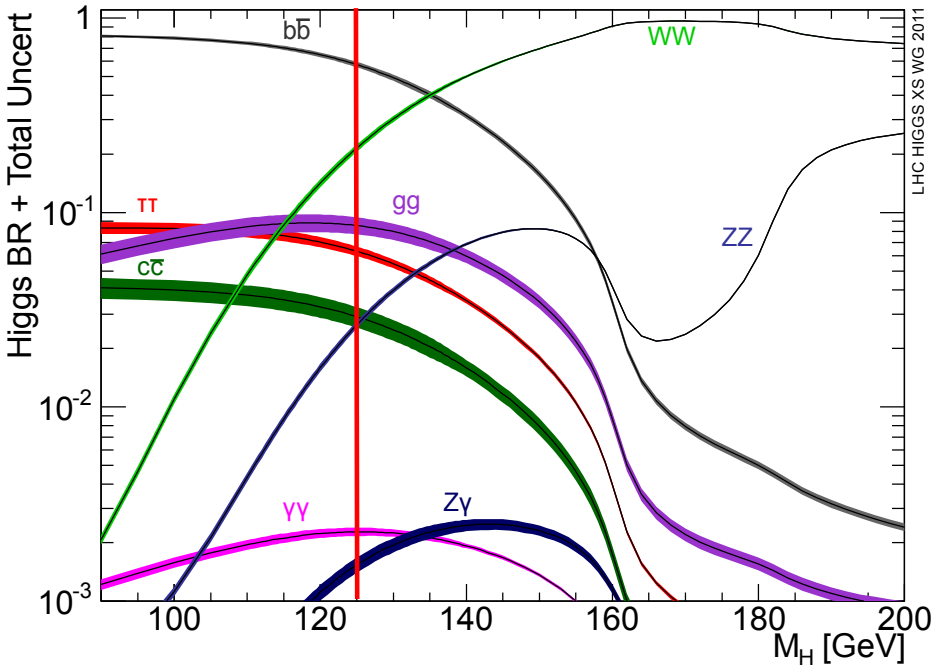

Figure 3.2.: Higgs decay modes in the SM [13]. The error bands visualize the higher order corrections and the vertical line the mass $m_H = 125\,\text{GeV}$ of the observed Higgs boson.

3.4. Z boson

The Z boson was discovered 1983 at the SPS after it had been upgraded to a proton-antiproton collider [14]. Its mass and decay width were measured precisely by LEP. Today the world's best fit for these values is [11]

$$m_Z = (91.1876 \pm 0.0021)\ \text{GeV}$$
$$\Gamma_Z = (2.4952 \pm 0.0023)\ \text{GeV}$$

At hadron colliders, the Z boson is produced at leading order via quark antiquark annihilation (DRELL-YAN process). DRELL-YAN processes can also be mediated by a photon (see Figure 3.3).

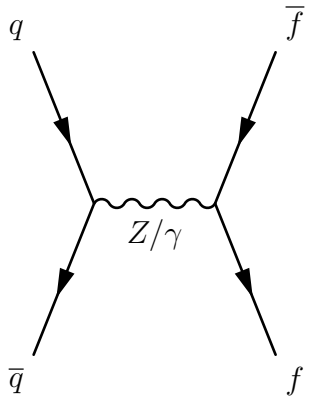

Figure 3.3.: Leading order Z production at hadron colliders.

Next-to leading order QCD corrections include the production of a quark or gluon, which forms a jet (see Figure 3.4). A Feynman diagram illustrating the virtual correction is given in Figure 3.5.

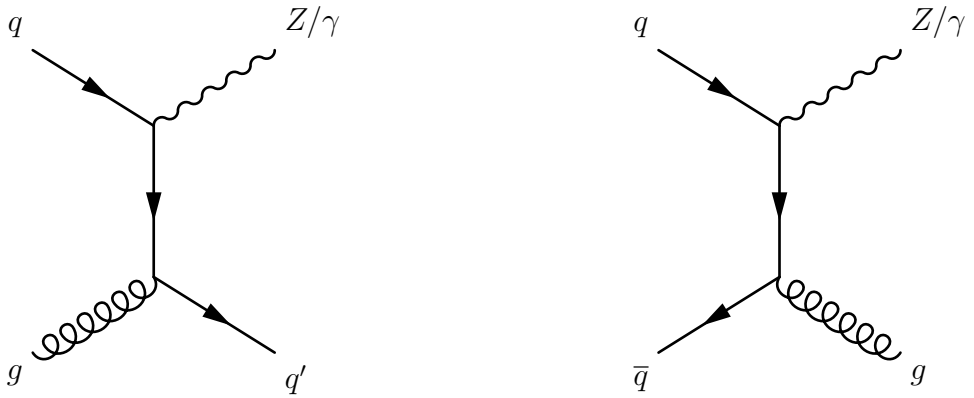

Figure 3.4.: Next-to leading order QCD correction for the Z production at hadron colliders.

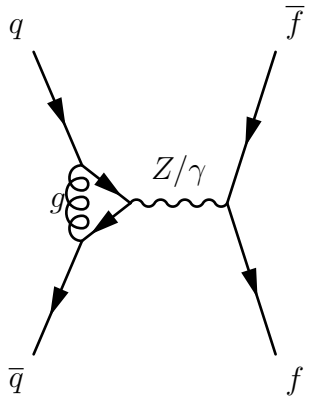

Figure 3.5.: Virtual correction to the Z production at hadron colliders.

Because of missing electric and colour charge the Z boson does not couple to photons and

gluons. Therefore, the decay into those particles is impossible. However, it can decay into all other weakly interacting particles, that are kinematically allowed (excludes W boson and top quark). Due to the V-A (vector-axial vector) structure of the Z-coupling the partial decay width for a decay into fermion f and antifermion $\overline{f}$ is at tree level [15]

$$\Gamma_f = \frac{g_Z^2 m_Z}{48\pi}\left(c_{A,f}^2 + c_{V,f}^2\right) \quad \text{with: } g_Z = \frac{g_W}{\sin\theta_W} \quad . \tag{3.1}$$

Vector and axial vector coupling $c_{A,f}$ and $c_{V,f}$ can be calculated using the electric charge Q and the third component T^3 of the weak isospin of the fermion

$$c_{V,f} = T^3 - 2Q\sin^2\theta_W \tag{3.2}$$

$$c_{A,f} = T^3 \quad . \tag{3.3}$$

Because of identical final states the process $Z \to \tau\tau$ is an irreducible background for $H \to \tau\tau$. Hence, the former process has to be understood precisely before the latter one can be measured.

4. Experimental Setup

4.1. LHC

The Large Hadron Collider (LHC), located at CERN, is a synchrotron colliding two proton beams at center-of-mass energies of $\sqrt{s} = 7,8$ TeV in Run I and 13 TeV in Run II. The input of the LHC is provided by several pre-accelerators depicted in Figure 4.1. The LHC was built into the tunnel of the Large Electron Positron Collider (LEP) and has a circumference of 27 km. Protons are accelerated in superconducting cavities. The beams are bent by superconducting (cooled down to 2 K) dipole magnets with a magnetic field of up to 8 T and focused by quadrupole magnets [16]. In order to avoid continuous interactions at the eight intersection points of the beams, these are separated into bunches. The number N of interactions for a process with cross section σ depends on the main machine parameter, the (instantaneous) luminosity $\mathcal{L}$

$$\frac{\mathrm{d}N}{\mathrm{d}t} = \sigma\mathcal{L} \quad . \tag{4.1}$$

The luminosity is given by [16]

$$\mathcal{L} = \frac{N_b^2 n_b \gamma f_{rev}}{4\pi\epsilon\beta^*} \quad , \tag{4.2}$$

where N_b is the number of protons per bunch, n_b the number of bunches per beam, γ the relativistic γ-factor, f_{rev} the revolution frequency. The emittance ϵ and the β-function β^* characterize the transverse beam size. This instantaneous luminosity is measured in well-known processes. A datasets size is usually specified by its integrated luminosity $\mathcal{L}_{int} = \int \mathcal{L}\mathrm{d}t$.

At four of the intersection points the main detectors ATLAS, CMS, LHCb and ALICE are located. As this study utilizes ATLAS data, an overview of the ATLAS detector is given in the next section (see also Figure 4.2).

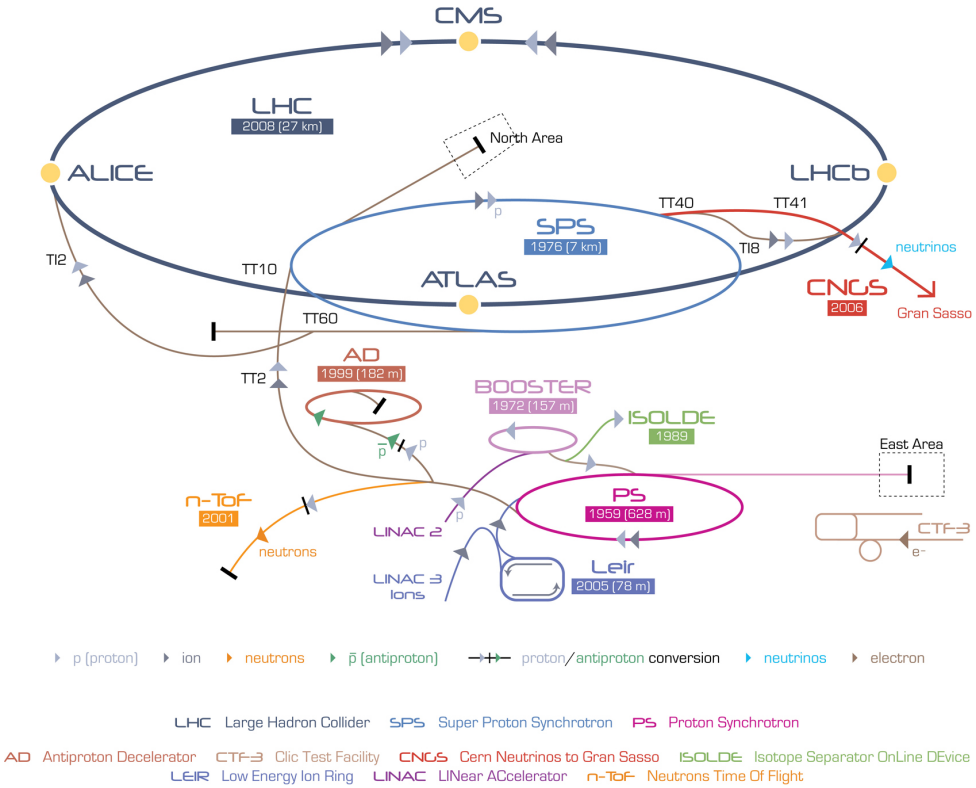

Figure 4.1.: The CERN accelerators; pre-accelerated by LINAC2, BOOSTER, PS and SPS the protons are injected into the LHC.

4.2. ATLAS detector

ATLAS is designed as a multi purpose detector. All subdetectors are arranged in an onion-like structure around the intersection point and divided into the central part (barrel) and the end-caps. The inner detector records the tracks of charged particles and is surrounded by the electromagnetic and the hadronic calorimeter. The outmost subdetector, the muon system, detects charged particles, which should be mainly muons. In order to measure the momentum based on tracks, a magnetic field, that bends the trajectories of charged particles, is needed. For the inner detector a solenoid field of 2 T strength is used, while the muon system is provided with a toroidal field. In both cases, superconducting magnets create the fields [17].

Coordinate system: The coordinate center is located at the intersection point and a right-handed coordinate system is defined by the x-axis pointing towards the center of the accelerator, y-axis pointing upwards and z-axis along the beam pipe. Because the detectors have cylindrical shape, the azimuthal angle (in the transverse plane) and the

pseudorapidity η are used

$$\eta = -\ln \tan\left(\frac{\theta}{2}\right) \quad , \tag{4.3}$$

where θ is the angle between the considered direction and the z-axis. Angular distances are often measured in R

$$R = \sqrt{\eta^2 + \phi^2} \quad . \tag{4.4}$$

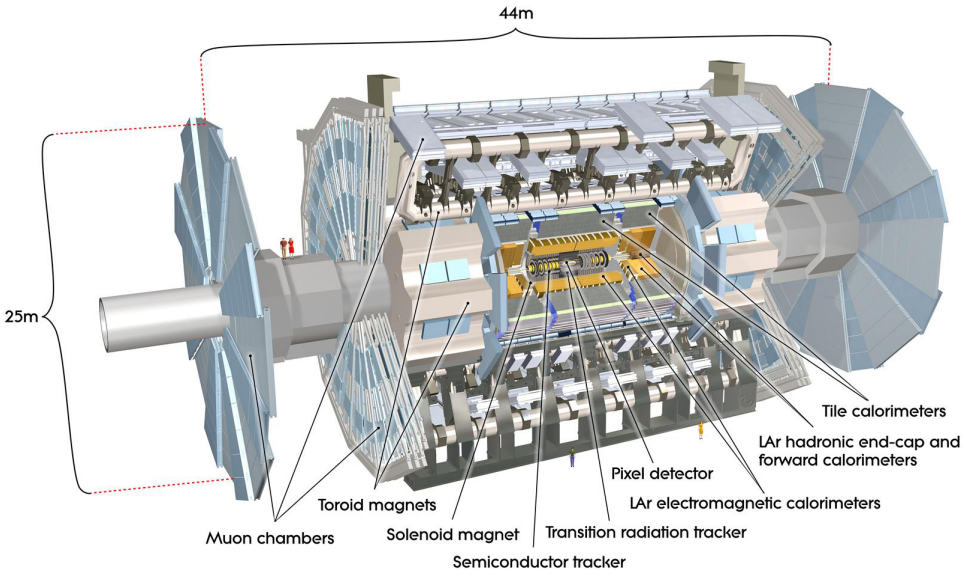

Figure 4.2.: The ATLAS detector [17].

4.2.1. Inner detector

The innermost part, the pixel detector, consists of four layers of silicon pixel detectors in the barrel region and 2x3 disks in the end-cap region. Traversing charged particles create charges in the semiconductor, which produce the signal. This type of detector has a good position resolution and is very important for b-tagging (identification of jets originating from a b-quark). The pixel detector is followed by four layers of silicon strip detectors (SCT) for the barrel region and 2x9 disks for the end-cap region. This detector type is more cost-efficient but less precise. Those detectors cover a pseudorapidity range of $|\eta| < 2.5$ [17].

The outmost part of the inner detector is the transition radiation tracker (TRT), which consists of 4 mm diameter straw tubes in a gas mixture (mainly Ar and CO_2). Charged

particles emit light in transitions between different media. Since this radiation depends on the Lorentz boost factor γ of the particle, this detector provides an additional possibility of particle identification [17].

4.2.2. Calorimeter

In the electromagnetic calorimeter, charged particles produce new particles via bremsstrahlung and pair production, so that a particle shower is created. The calorimeter is designed to completely absorb the energy of the particles in this way and provide an energy measurement based on the deposited energy. In ATLAS, the electromagnetic calorimeter is a sandwich calorimeter, consisting of alternating lead (copper for the forward calorimeter) plates for particle absorption and liquid Argon for detection. To ensure full ϕ coverage, absorber and active material are arranged in an accordion shape.
In the hadronic calorimeter, showers are created via the strong interaction. For the barrel region steel and a scintillator is used. The absorber of the end-cap calorimeter is copper and tungsten in the forward calorimeter and the active material liquid Argon. The calorimeter covers $|\eta| < 4.9$ [17].

4.2.3. Muon system

Because all particles except for muons (minimum ionising) and neutrinos should be absorbed in the calorimeter, charged particles detected in the muon system are most likely muons. The barrel of the muon system consists of Monitored Drift Tubes (MDT), gas-filled drift chambers, and resitive plate chambers (RPC). The latter ones are parallel metal plates with a large voltage applied. If a charged particle traverses the gas-filled gap, a spark along the track is produced. In the end-cap region thin gap chambers (TGC) and cathode strip chambers (CSC), multi-wire proportional chambers, are used. While MDT and CSC provide momentum measurements, TGC and RPC are used for fast muon triggers. The coverage of the muon system is $|\eta| < 2.7$ [17].

4.2.4. Trigger system

For a bunch spacing of 50 ns (early Run II), the collision rate is 20 MHz. Hence, triggers are used to select only interesting events before they are saved [16, 17]:

- **Hardware based L1 trigger:** Based on information from the muon system and the calorimeter, events are filtered for: objects with high transverse energy or high missing momentum $\not{p}_T$ (see section 4.2.5) for the whole event. This trigger reduces

the event rate to 75 kHz. It also defines regions of interest (ROI) for further investigation.

- **Software based L2 trigger:** Seeded by the ROI information, the L2 trigger utilizes all detector information separately to further reduce to 3.5 kHz.
- **Event filter:** More complex algorithms using the full event information reduce the event rate down to 200 Hz.

For Run II, L2 trigger and event filter are combined to a single level, the high level trigger (HLT).

4.2.5. Neutrinos

Since neutrinos only interact weakly, they travel (most likely) through the whole detector without any interaction. Hence, neutrinos or other similarly interacting particles beyond the SM can only be detected indirectly via the momentum conservation. Typically, only one quark or gluon per proton takes part in the hard scattering and the rest of the proton is forward and therefore undetected. Thus, the momentum balance can only be used in the transverse plane with the missing momentum $\vec{\not{p}}_T$ having only a transverse component

$$\vec{\not{p}}_T = -\sum_{particles} p_{T,i} \quad . \tag{4.5}$$

Obviously, this variable picks up all the uncertainties of the individual momentum measurements. Note that the absolute value $\not{p}_T$ of the missing transverse momentum is usually referred to as missing E_T or MET in Atlas.

5. Event simulation

Monte Carlo (MC) simulations are used to model statistical processes and accordingly in particle physics to simulate events. First the scattering process is simulated based on cross section calculations. This includes final and initial state radiation as well as the hard scattering process, decays and hadronisation (formation of hadrons out of hard scattering quarks). In this step the particle kinematics are calculated. However, detector effects are not considered yet. Consequently, this information is called truth information. Detector simulation is typically done by GEANT [18]. After the detector simulation, the simulated events have the same format as the recorded ones and undergo the same reconstruction procedure.
A short description of the MC generators used for this thesis is given below.

Pythia: PYTHIA is a general purpose MC generator. Besides the capability of simulating hard scattering processes at LO, it can also simulate soft interaction, initial and final state parton shower, multiple parton-parton interactions, interactions with beam remnants, hadronisation and decays. A string fragmentation model is used for hadronisation. Furthermore, PYTHIA can read the output of other generators, such as NLO QCD generators [19, 20].

PowHeg: POWHEG is a NLO QCD generator, that generates the hardest radiation first. It can be combined with the PYTHIA generator to simulate the parton shower and the underlying event [21].

6. Reconstruction

6.1. Jets

Jet reconstruction starts from Calorimeter clusters. The anti-k_t algorithm [22] combines clusters if a criterion based on the distance parameter $\Delta R = 0.4$ is fulfilled. Afterwards, the calorimeter response has to be related to the energy of the hadrons that constitute the jet. This is done via the jet energy scale (JES) that has to correct for the different response to electromagnetic and hadronic showers, calorimeter leakage, dead material, pile-up and energy deposits below the noise threshold. The calibration procedure is performed similar to the one in [23, 24].

6.2. Electron candidates

Electron reconstruction clusters in the EM calorimeter are formed by a sliding-window algorithm. Tracks from the inner detector with $p_T > 0.5\,\text{GeV}$ are extrapolated to the calorimeter and matched to those candidates. An electron candidate has to have at least one matched track. In case of ambiguity, tracks with pixel or SCT hits are prioritised. The matching is only possible for $|\eta| < 2.5$. For other electron candidates only calorimeter-based reconstruction can be used so that distinction from photons is difficult [25]. The electron identification is based on a likelihood method, which uses different sets of discriminating variables for the working points loose, medium and tight [26]. This analysis requires tight electrons.

6.3. Muon candidates

There are four different types of reconstructed muons [27]:

- Standalone: Muons are reconstructed based on the track in the muon system. The track is extrapolated back to the beam line and the energy of the candidate is corrected for the loss in the calorimeter.

- Combined: The independently reconstructed tracks in the inner detector and the muon system are matched to each other.
- Segment-tagged: The track in the inner detector is matched to at least one track fragment in the Monitored Drift Tube Chambers or the Cathode Strip Chambers.
- Calorimeter-tagged: A minimum ionizing particle in the calorimeter is matched to a inner detector track.

While combined muons have the highest purity, other muons can be used to increase the acceptance.
Only combined and standalone muons that pass the medium quality criterion are used in this thesis. A further restriction to $|\eta| < 2.42$ exclude standalone muons [28].

6.4. Hadronic τ candidates

τ leptons with leptonic final states are not reconstructed as τ leptons but as leptons. Because neutrinos remain undetected, the reconstructed τ lepton can only be the visible τ lepton. Therefore, reconstructed τ refers to the reconstructed visible hadronically decaying τ lepton.
The hadronic τ reconstruction is based on jets formed by the anti-k_t-algorithm with a distance parameter $\Delta R = 0.4$. τ seeds have to pass $p_T > 10\,\text{GeV}$ and $\eta < 2.5$. A barycenter of the clusters of the seed is calculated. All clusters in a cone of $\Delta R = 0.2$ around the barycenter are used to calculate the intermediate axis, the direction of the τ candidate. Tracks in the core region ($\Delta R < 0.2$ with respect to the intermediate axis) with $p_T > 1$ GeV , ≥ 2 hits in the pixel detector, ≥ 7 hits in pixel and SCT layers combined are associated to the τ candidate if the distance of closest approach (with respect to the τ vertex) fulfills the following criteria. In the transverse plane the distance of the track satisfies $d_0 < 1$ mm and the longitudinal distance z_0 satisfies $|z_0 \sin\theta| < 1.5$ mm. Tracks in the isolation region ($0.2 < \Delta R < 0.4$) are not associated, but counted as they provide input for the identification. This identification and discrimination against jets is based on a variety of track and calorimeter based variables. Those variables are combined to form a boosted decision tree (BDT) that provides separation between jets and τ leptons (JetBDT). For example, the track radius R_{track}, the p_T-weighted R-distance of all tracks in the core and isolation region, is expected to be much smaller for τ leptons than for jets [29]. The JetBDT working points are defined such that the signal efficiency is independent of the true visible hadronic τ lepton p_T. For the loose, medium and tight working points the signal efficiencies are 0.6, 0.55 and 0.45 in the 1 prong case and 0.5,

0.4 and 0.3 in the 3 prong case [30].
For Run II, substructure reconstruction of τ_{had} leptons becomes accessible, meaning neutral pions in τ decays can be reconstructed. A sketch of this reconstruction procedure is presented here, for a detailed description see [31]. Seeded by the hadronic τ candidate, π^0 candidates are built by reclustering the EM energy in the core region. Then the $\pi^\pm$ energy is subtracted from the energy of the closest π^0 candidate. The $\pi^\pm$ energy can be estimated using the track-based energy $E^{EM}_{\pi^\pm}$ and the energy deposit $E^{HAD}_{\pi^\pm}$ in the hadronic calorimeter associated to the $\pi^\pm$

$$E^{EM}_{\pi^\pm} = E^{track}_{\pi^\pm} - E^{HAD}_{\pi^\pm}.$$

In order to reduce the number of π^0 candidates originating from pile-up a p_T threshold has to be passed. The remaining background are then $\pi^\pm$ remnants. These contributions can be decreased by requiring the π^0 candidates to pass a BDT threshold that relies on the shower shape.

6.5. MET

The missing transverse momentum is calculated by utilizing momentum conservation in the transverse plane. All reconstructed particles and jets enter the calculation. Furthermore, the soft term $\vec{p}_{T,soft}$ accounts for tracks in the inner detector or energy deposits in the calorimeter that are not associated to an object

$$\vec{\not{p}}_T = -\sum_e \vec{p}_T - \sum_\mu \vec{p}_T - \sum_\tau \vec{p}_T - \sum_\gamma \vec{p}_T - \sum_{jets} \vec{p}_T - \vec{p}_{T,soft} \quad .$$

The correct soft term handling reduces the impact of pile-up on MET. Therefore, multiple MET definitions with different treatment of the soft term exist. This analysis uses the MET TST (track soft term) definition [32]

$$\vec{p}_{T,soft} = \sum_{soft\ tracks} \vec{p}_T \quad ,$$

where soft tracks are tracks with $p_T > 0.5$ GeV not associated to any of the hard scattering objects.

7. Optimisation of the Missing Mass Calculator

The mass reconstruction of a di-τ system is of central relevance for $H \to \tau\tau$ searches because it is an important variable to distinguish Z from H processes. Therefore, an improvement of the mass resolution is desirable.

7.1. Missing Mass Calculator

The reconstruction of the invariant mass of the Higgs boson in $H \to \tau\tau$ events involves the treatment of MET due to the production of at least two neutrinos in the final state. One possibility is the collinear approximation, which assumes that the neutrinos are parallel to the visible decay products. However, this algorithm has some disadvantages:

- Since the system of equations that describe the event cannot be solved in the degenerated case, not all events can be reconstructed (up to 25%).
- As shown in Figure 7.1, the mass reconstructed using the collinear approximation has a long tail for high masses caused by mis-reconstructed events due to mismeasurements of the missing momentum $\not{p}_T$.

A more robust mass reconstruction is provided by the Missing Mass Calculator (MMC) [33]. A system of two hadronic τ leptons can be completely described in terms of visible and invisible decay products by four equations as follows,

$$\begin{aligned}
\not{p}_x &= p_{miss_1} \sin\vartheta_{miss_1} \cos\phi_{miss_1} + p_{miss_2} \sin\vartheta_{miss_2} \cos\phi_{miss_2} \\
\not{p}_y &= p_{miss_1} \sin\vartheta_{miss_1} \sin\phi_{miss_1} + p_{miss_2} \sin\vartheta_{miss_2} \sin\phi_{miss_2} \\
m^2_{\tau_1} &= m^2_{miss_1} + m^2_{vis_1} + 2\sqrt{p^2_{vis_1} + m^2_{vis_1}}\, p_{miss_1} - 2p_{miss_1} p_{vis_1} \cos\Delta\theta_1 \\
m^2_{\tau_2} &= m^2_{miss_2} + m^2_{vis_2} + 2\sqrt{p^2_{vis_2} + m^2_{vis_2}}\, p_{miss_2} - 2p_{miss_2} p_{vis_2} \cos\Delta\theta_2 \quad .
\end{aligned}$$

The indices *miss* and *vis* refer to the neutrinos and visible decay products of the considered τ lepton, $\Delta\theta$ is the angle between the visible and invisible decay products. In the

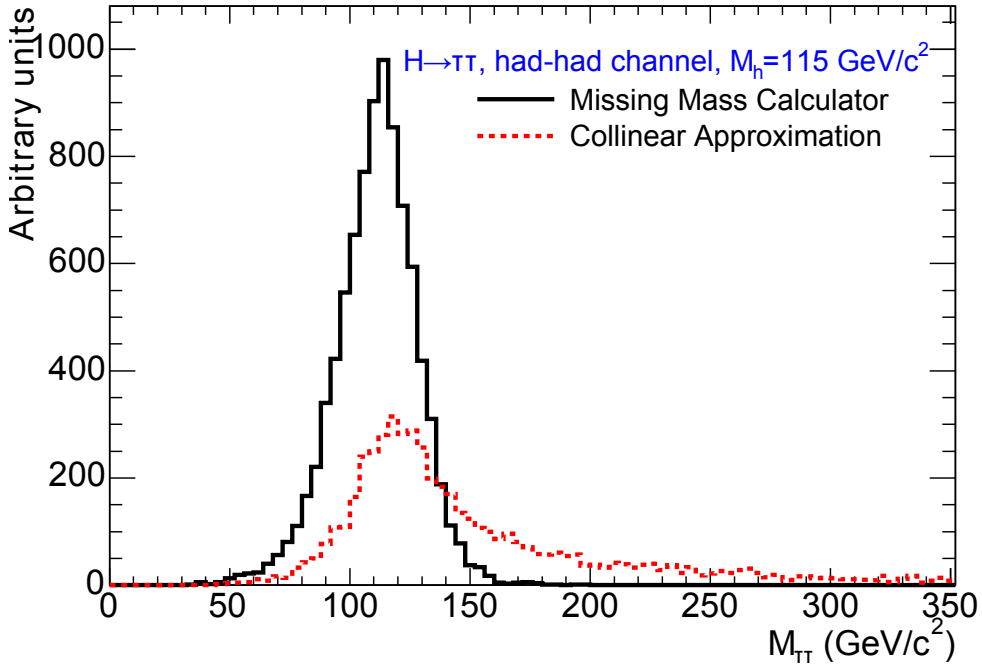

Figure 7.1.: Reconstructed invariant of the Higgs boson in H $\rightarrow \tau\tau$ using collinear approximation and MMC [33].

case of two hadronic τ leptons, which this study focuses on, there are six unknowns (for example the ones highlighted in red), all other variables are known or can be deduced from the others. Correspondingly, there are seven or eight unknowns in the case of $\tau_{lep}\tau_{had}$ and $\tau_{lep}\tau_{lep}$. Therefore, one needs additional information to solve the system. This information can be provided if one knows the distribution of, for example, the opening angle $\Delta\theta$ (see Figure 7.4). The calculated mass is then weighted with the probability of the angles and the best estimate based on these probabilities is chosen.

Those distributions can only be produced based on MC samples since one needs the truth information for the neutrinos, where "truth" means generated particles before detector effects are simulated. Starting with reconstructed (visible) τ leptons this, of course, needs a matching to a truth τ. This is performed by searching for truth τ leptons in a ΔR cone of 0.2 around the reconstructed one. Angular distributions for MMC were already produced for Run I [33]. As in Run II the τ substructure (information on neutral π) becomes accessible, one expects an improved MMC mass resolution if the angular distributions are separately produced for all (hadronic) decay modes. Hence, the aim is to produce the distributions for the truth decay modes 1p0n, 1p1n, 1p2n, 3p0n and 3p1n (xpyn stands for x prong/charged pions and y neutral pions) as a function of the truth τ-momentum p_{truth} and parametrize these.

For the production of the distributions a sample[1] of 20 million $Z \rightarrow \tau\tau$ events at $\sqrt{s} = 13$ TeV with 50 ns bunch spacing is used. This sample is generated by POWHEG [21] interfaced with PYTHIA using the AZNLO tune [34] and the CTEQ6L1 PDF set [35]. The τ decay is simulated by TAUOLA [36].

Figure 7.2 shows a 2d histogram of p_{truth} and $\Delta\theta$. For this application, $\Delta\theta$ is calculated using reconstructed τ and neutrino. This illustrates that the distributions are p_{truth} dependent. For large momenta the boost of the τ is large, such that the decay products are collimated and the peak of the angular distribution is shifted towards smaller angles.
One-dimensional comparisons of the different decay mode distributions can be seen in Figures 7.3a and 7.3b. The distributions are normalised to unity so that they describe a probability density function. The difference between the distributions motivates the separate parametrization of the decay modes. Resolving the different peaks of the distributions should improve the mass resolution. In general, the distributions in the 3 prong case tend to be more similar than in the 1 prong case, which is expected. When going from four to five particles, the kinematics should not change in such a drastic way as for the transition from two to three. The difference becomes smaller for higher truth momenta (see Figures 7.3c and 7.3d) and the peak is shifted towards smaller angles since the boost of the τ lepton starts to dominate the kinematics.

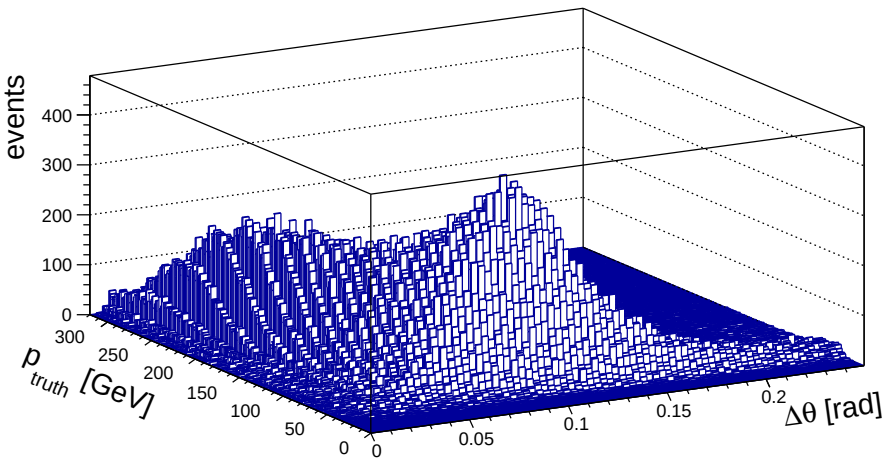

Figure 7.2.: 2d distribution of $\Delta\theta$ and p_{truth}.

[1] mc15_13TeV.361108.PowhegPythia8EvtGen_AZNLOCTEQ6L1_Ztautau.merge.AOD.e3601_s2576_s2132_r6630_r6264

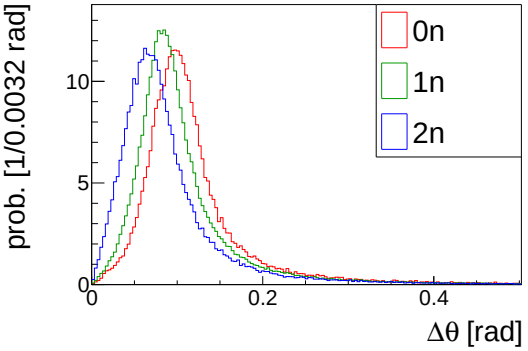

(a) 1 prong, 40 GeV $\leq p_{truth} \leq$ 45 GeV .

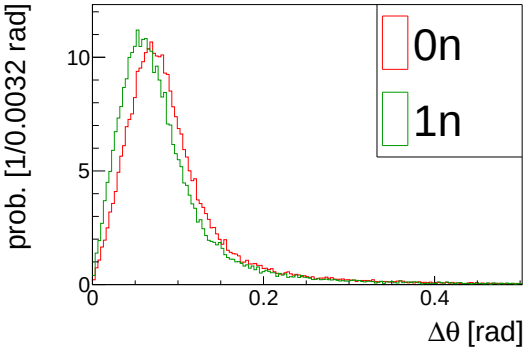

(b) 3 prong, 40 GeV $\leq p_{truth} \leq$ 45 GeV .

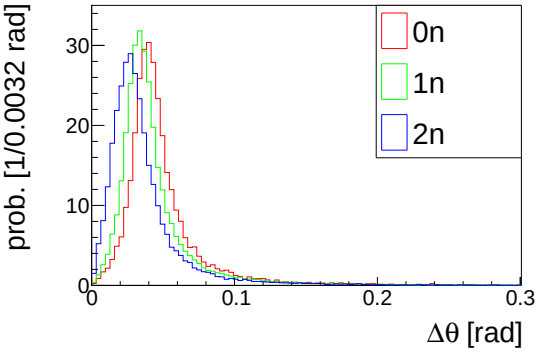

(c) 1 prong, 100 GeV $\leq p_{truth} \leq$ 105 GeV .

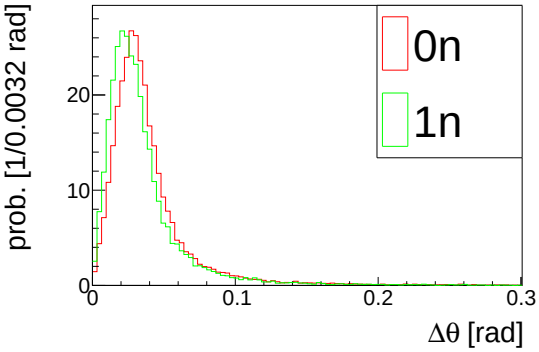

(d) 3 prong, 100 GeV $\leq p_{truth} \leq$ 105 GeV .

Figure 7.3.: Angular distributions of $\Delta\theta$ (angle between visible τ and ν). The underlying $Z \rightarrow \tau\tau$ sample is generated with PowHeg and Pythia at $\sqrt{s} = 13$ TeV with 50 ns bunch spacing.

7.2. α distributions

Since a simple analytical description of the distribution exists for the angle α between truth τ and ν, this is more useful for the parametrisation. Via energy and momentum conservation $\cos\alpha$ fixes the absolute value of the neutrino momentum p_ν

$$p_\nu = \frac{m_{vis}^2 - m_\tau^2}{2p_\tau \cos\alpha - 2\sqrt{m_\tau^2 + p_\tau^2}} \quad ,$$

where p_τ is the truth τ momentum and m_{vis} and m_τ are the invariant masses of the visible and the truth τ. Since two sides and the enclosed angle are fixed by α, the momentum triangle shown in Figure 7.4 is fully specified. As a result, $\Delta\theta$ is uniquely defined for every angle α. Thus, parametrising α distributions is equivalent to a $\Delta\theta$ parametrisation.

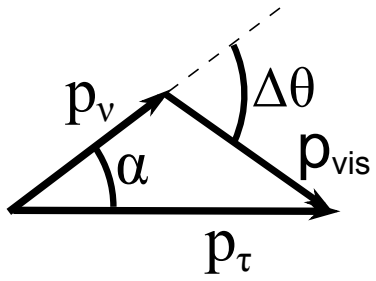

Figure 7.4.: Sketch of the momentum balance in hadronic τ decays.

The analytic description of the α distributions can be found in the following way. In the rest frame of the τ lepton the distribution is flat

$$\mathrm{d}N = \frac{1}{2}|\mathrm{d}(\cos\alpha_0)| \quad ,$$

where α_0 is the angle between the direction of the truth τ and the neutrino in the rest frame of the τ lepton.
The relation between α and α_0 can be found by applying a boost into the lab frame with $\gamma^{-2} = 1 - \beta^2$

$$\tan\alpha = \frac{\sqrt{1-\beta^2}\sin\alpha_0}{\beta + \cos\alpha_0} \quad .$$

This can be solved for $\cos\alpha_0$

$$\cos\alpha_0 = \frac{-\beta\sin^2\alpha \pm \cos\alpha(1-\beta^2)}{1-\beta^2\cos^2\alpha} \quad .$$

Depending on the sign one chooses, the following α distributions are obtained

$$\frac{\mathrm{d}N}{\mathrm{d}\alpha} = \frac{\sin\alpha(1-\beta^2)}{2(1-\beta\cos\alpha)^2} \tag{7.1}$$

$$\frac{\mathrm{d}N}{\mathrm{d}\alpha} = \frac{\sin\alpha(1-\beta^2)}{2(1+\beta\cos\alpha)^2} \quad . \tag{7.2}$$

Because there are no assumptions on the other daughter particles, this distribution should hold for all decay modes if no bias is introduced by selection cuts.

The α distributions are shown in Figure 7.5 for different momenta. For high momenta the distributions for the different decay modes are quite similar, for low momenta they differ slightly. This difference can be explained by different reconstruction efficiencies at small angles α. Since for small angles visible and invisible decay products are almost collinear,

it is probably easier to identify a τ lepton that decays into more pions. For high momenta the difference becomes smaller because the boost dominates the variation due to different numbers of daughter particles.

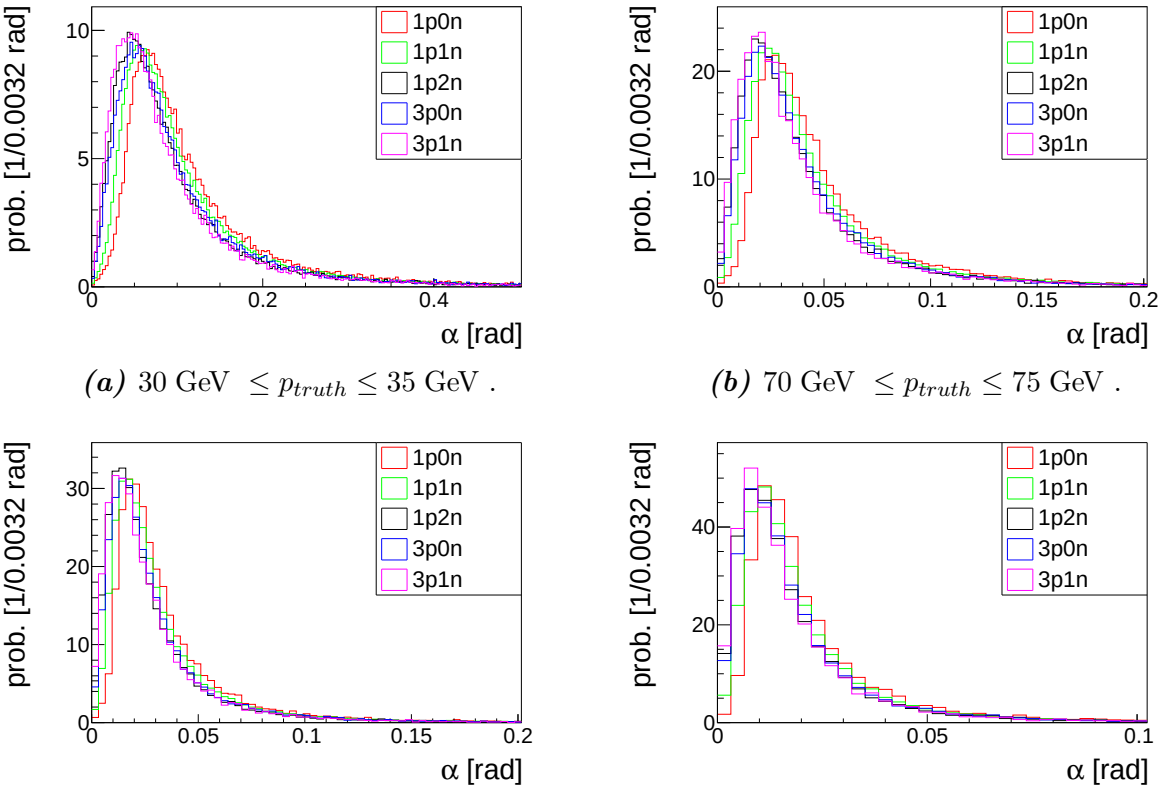

(a) 30 GeV $\leq p_{truth} \leq$ 35 GeV .

(b) 70 GeV $\leq p_{truth} \leq$ 75 GeV .

(c) 100 GeV $\leq p_{truth} \leq$ 105 GeV .

(d) 150 GeV $\leq p_{truth} \leq$ 155 GeV .

Figure 7.5.: α distributions (without selection cuts). The underlying $Z \to \tau\tau$ sample is generated with PowHeg and Pythia at $\sqrt{s} = 13$ TeV with 50 ns bunch spacing.

If one introduces selection cuts for the seeding reconstructed τ, a large bias of the α distributions is introduced. In order to account for typical cuts in later analyses, a $p_T >$ 20 GeV cut is applied and the τ lepton is required to pass the loose JetBDT working point (see section 6). Figure 7.6 depicts the impact of these cuts and also the difference between the loose and medium BDT working points.

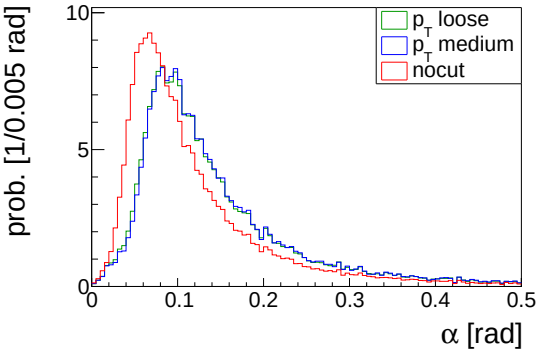

(a) 1p0n, 30 GeV $\leq p_{truth} \leq$ 35 GeV .

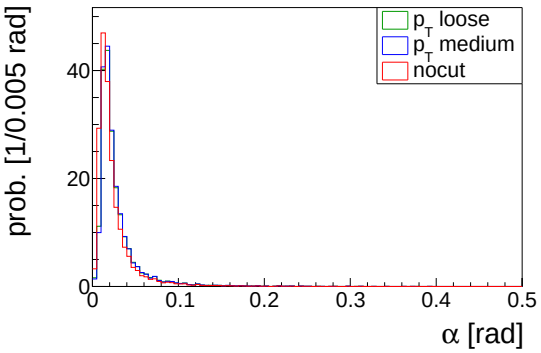

(b) 1p0n, 150 GeV $\leq p_{truth} \leq$ 155 GeV .

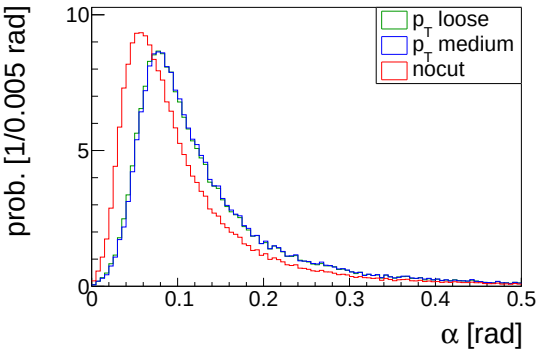

(c) 1p1n, 30 GeV $\leq p_{truth} \leq$ 35 GeV .

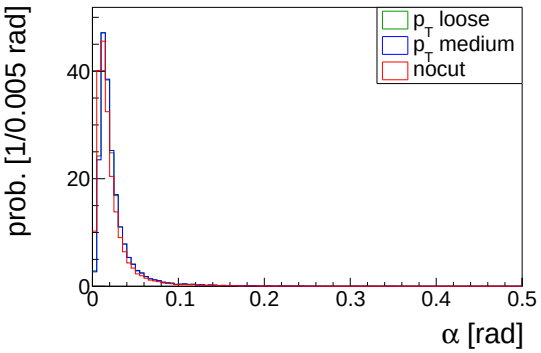

(d) 1p1n, 150 GeV $\leq p_{truth} \leq$ 155 GeV .

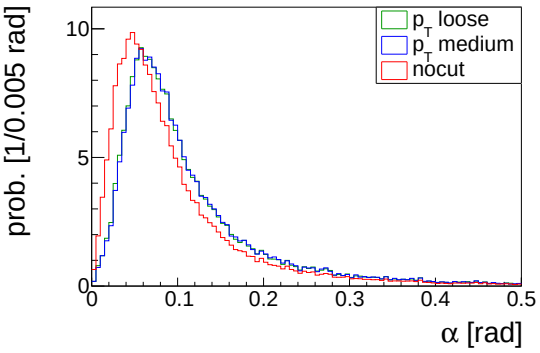

(e) 1p2n, 30 GeV $\leq p_{truth} \leq$ 35 GeV .

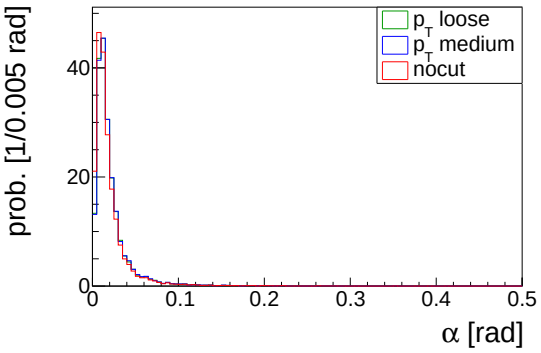

(f) 1p2n, 150 GeV $\leq p_{truth} \leq$ 155 GeV .

Figure 7.6.: α distributions comparing impact of selection cuts: nocut, $p_T > 20$ GeV + BDT loose, $p_T > 20$ GeV + BDT medium. The underlying $Z \to \tau\tau$ sample is generated with PowHeg and Pythia at $\sqrt{s} = 13$ TeV with 50 ns bunch spacing.

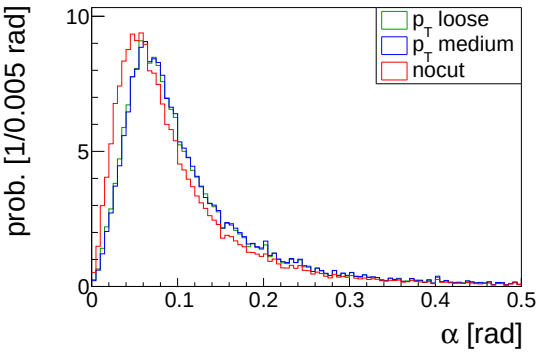

(g) 3p0n, 30 GeV $\leq p_{truth} \leq$ 35 GeV .

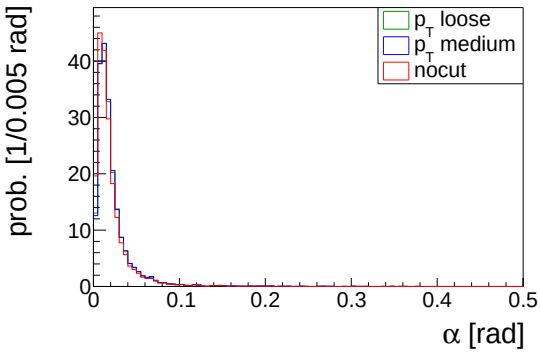

(h) 3p0n, 150 GeV $\leq p_{truth} \leq$ 155 GeV .

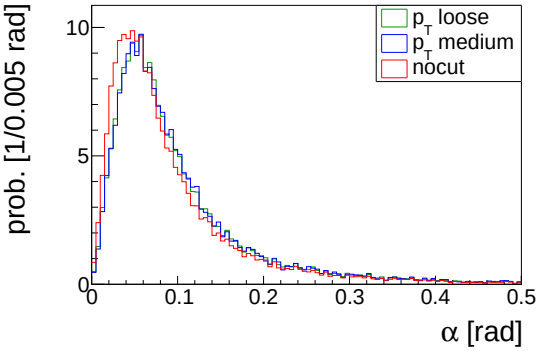

(i) 3p1n, 30 GeV $\leq p_{truth} \leq$ 35 GeV .

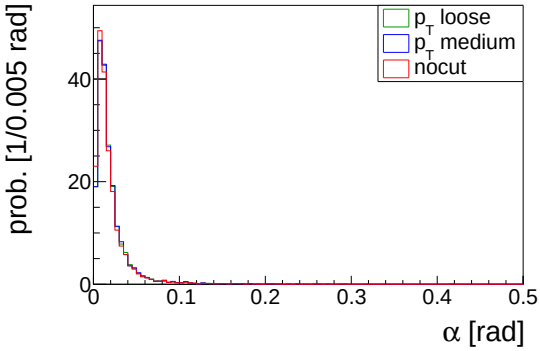

(j) 3p1n, 150 GeV $\leq p_{truth} \leq$ 155 GeV .

Figure 7.6.: α distributions comparing impact of selection cuts: nocut, $p_T > 20$ GeV + BDT loose, $p_T > 20$ GeV + BDT medium. The underlying $Z \to \tau\tau$ sample is generated with PowHeg and Pythia at $\sqrt{s} = 13$ TeV with 50 ns bunch spacing.

Whereas the difference between the loose and medium cut is very small, the cuts in general introduce considerable bias, especially for low momenta, resulting in a shift of the peak. At small angles, the truth τ is almost collinear to the decay products so that the p_T cut forces the truth τ into the transverse plane. Thus, the loss of events at small angles implies that many τ are forward. An additional observation is that the bias differs from one decay mode to another. Hence, the variation between distributions of different decay modes becomes larger due to the cuts.

Since the medium BDT cut biases the distributions only slightly more than the loose cut, one can stick to the loose cut for the following fits to get better statistics. However, the analytic formula as in equation (7.2) does not describe the biased distributions seen in Figure 7.6. So the fit function needs to be modified: It turns out that the left-hand side of the distributions peak is described sufficiently well by a Gaussian. The right-hand side

can be described by the analytic formula, if β (or $1-\beta^2$) is a free parameter and a shift parameter is introduced. The physical value of $1-\beta^2$ cannot be used because for low momenta the physical values differ much from the best fit values (see Figure 7.7b). Both parts of the fit function are matched at the maximum.
Example fit results are presented in Figure 7.8. For low momenta there are minor deviations at small angles while for higher momenta the function fits almost perfectly.

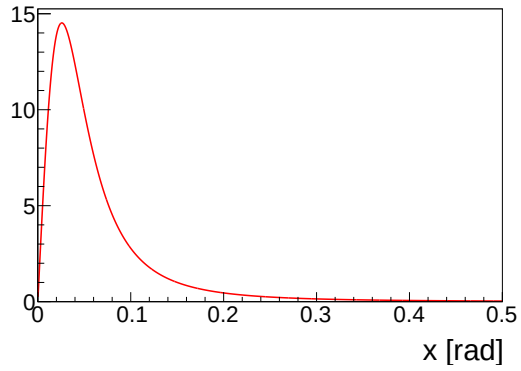

(a) Theoretical $\alpha = x$ distribution as in equation (7.2).

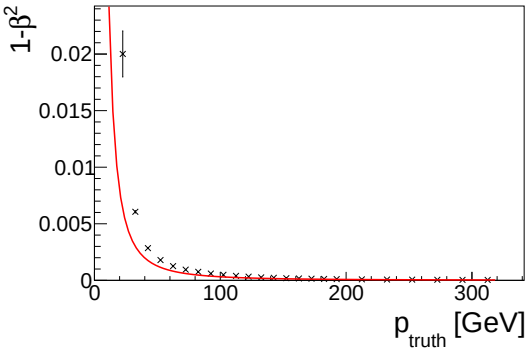

(b) Physical value of $1-\beta^2$ (1p1n), mean for the considered momentum interval $[p_L, p_H]$ and τ mass m_τ: $\frac{m_\tau}{p_H - p_L}\left[\arctan\left(\frac{p}{m_\tau}\right)\right]_{p_L}^{p_H}$.

Figure 7.7.: Analytic description of α and physical value of $1-\beta^2$.

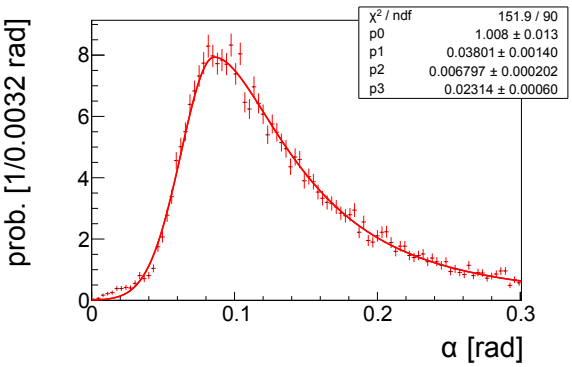

(a) 1p0n, 30 GeV $\leq p_{truth} \leq$ 35 GeV

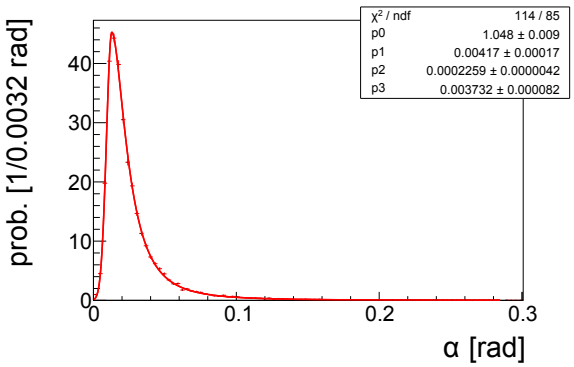

(b) 1p1n, 140 GeV $\leq p_{truth} \leq$ 145 GeV

Figure 7.8.: Fits for α distributions with parameters normalisation (p_0), shift (p_1), $1-\beta^2$ (p_2) and (Gaussian) sigma (p_3). The underlying $Z \to \tau\tau$ sample is generated with PowHeg and Pythia at $\sqrt{s} = 13$ TeV with 50 ns bunch spacing.

The momentum dependence of the fit parameters $1-\beta^2$ and sigma is determined by

independent fits (see Figure 7.9). By performing these fits independently, the correlations between fit parameters are neglected. Since the results of the whole procedure describe the distributions sufficiently well (see for example Figure 7.11), this treatment is justified. The momentum dependences of $1 - \beta^2$ and sigma are then used to fix these parameters in a second fit to the angular distributions, leaving the shift and normalisation parameter as free fit parameters. In this way the fit of the shift parameter is stabilised. Afterwards momentum dependence of the shift parameter is extracted (see Figure 7.9). The momentum dependence of the normalisation does not need to be modelled because the implementation of the MMC does not care about the absolute normalisation.
The best description for the $1 - \beta^2$ parameter involves singularities around 20 GeV . In order to avoid such problems above 20 GeV , the singularities are fixed to 19 GeV . The resulting description fits quite well in the momentum range of the fit. Nevertheless, it provides unreasonable angular distributions for high momenta (see for example Figure 7.10). Therefore a fit to the distribution in an overflow bin [320 GeV , 2000 GeV] is performed. Because the momentum distribution in this overflow bin is not flat, the angular distributions are weighted with the inverse probability of this momentum $p^{-1}(p_{truth})$ to equally account for all angular distributions in the overflow bin. In this high momentum region the analytic formula in equation (7.2) with free fit parameter $1 - \beta^2$ is sufficient. The results are given in Table 7.1.

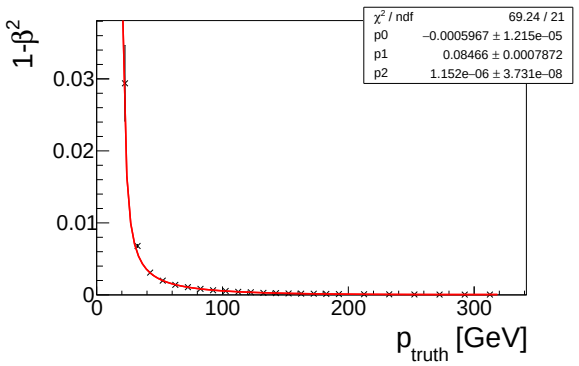

(a) $1-\beta^2$, fit function $p_0 + \frac{p_1}{x-19\ \mathrm{GeV}} + p_2 x$

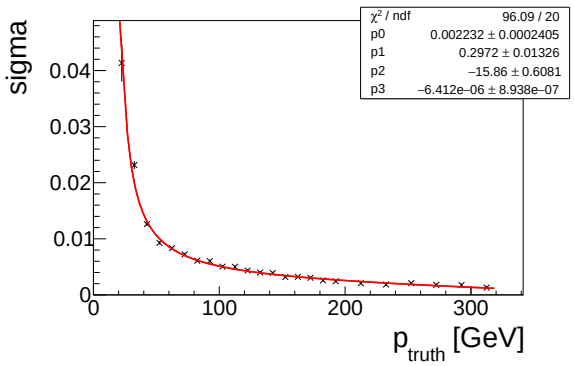

(b) Sigma, fit function $p_0 + \frac{p_1}{x+p_2} + p_3 x$

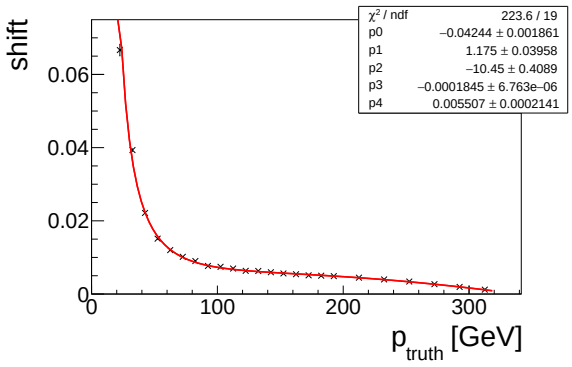

(c) Shift, fit function $p_0 + \frac{p_1}{x+p_2} + p_3 x + p_4\sqrt{x}$

Figure 7.9.: Momentum dependence of the fit parameters for the α distributions (1p0n). For the other decay modes see Figures A.1 to A.4. The underlying $Z \to \tau\tau$ sample is generated with PowHeg and Pythia at $\sqrt{s} = 13$ TeV with 50 ns bunch spacing.

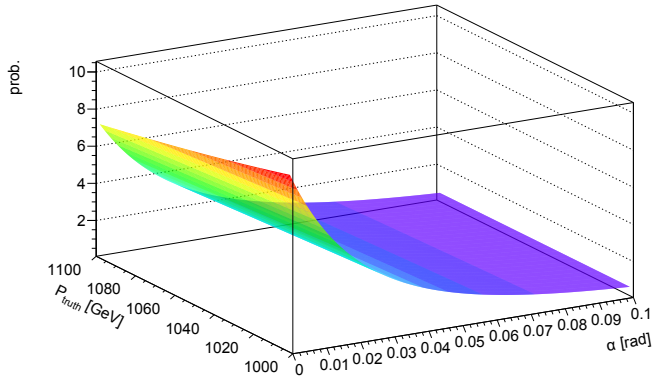

Figure 7.10.: High momentum extrapolation of the angular distributions (1p0n). The angular distribution is much wider than for smaller momenta. Thus, the fit results cannot be extrapolated to arbitrary high momenta. The underlying $Z \rightarrow \tau\tau$ sample is generated with PowHeg and Pythia at $\sqrt{s} = 13$ TeV with 50 ns bunch spacing.

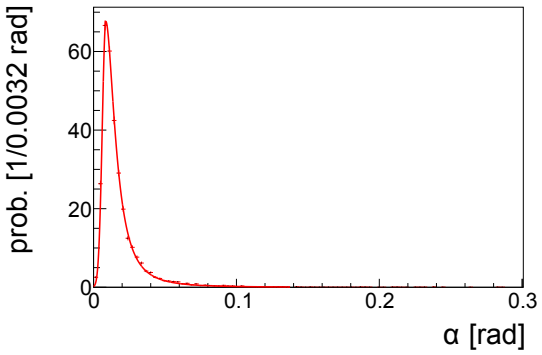

Figure 7.11.: Angular description yielded by the fitting procedure compared to the angular distribution (1p1n). The Momentum bin [200 GeV , 205 GeV] is in between the momentum values used to determine the momentum dependence. The underlying $Z \rightarrow \tau\tau$ sample is generated with PowHeg and Pythia at $\sqrt{s} = 13$ TeV with 50 ns bunch spacing.

Decay mode	$1-\beta^2$ $[10^{-5}]$
1p0n	1.80 ± 0.11
1p1n	1.05 ± 0.06
1p2n	0.95 ± 0.07
3p0n	1.08 ± 0.07
3p1n	1.07 ± 0.08

Table 7.1.: Results of the fits in the overflow bin [320 GeV , 2000 GeV].

7.3. Test of the parametrisation

In order to test the new parametrisation, the MMC mass distributions are compared for the Run I (2012) and the new (2015) parametrisation using 13 TeV MC samples. However, MMC calculates three different masses. To understand the differences, an overview of the algorithm is necessary. MMC uses a Markov Chain [37] to scan the parameter space for solutions. If a solution is found, its probability p_0 is calculated based on the angular distributions. Starting from this solution, the MMC scans for further solutions. These are accepted with probability $\min(1, {}^{p_1}/_{p_0})$, where p_1 is the probability of the new solution.

- MMC0: Uses the most likely solution and the corresponding mass.
- MMC1: Fills all masses weighted with the probability of the solution into a histogram and determines the most likely mass. In this case MMC cannot provide information on the neutrino momentum.
- MMC2: The mass is calculated based on the most likely neutrino four-vectors.

Another important factor for the mass reconstruction is the MET treatment. The MET resolution σ_{MET} is parametrised as a function of $\sum_{objects} E_T$. The standard configuration of MMC constrains the solution to lie in the $4\sigma_{MET}$ region around the MET value. However, in the case of zero jets (with $p_T > 30$ GeV) MPT is used instead of MET because of a better resolution. MPT is calculated using the visible decay products 1 and 2

$$\vec{p}_T^{\,MPT} = -\vec{p}^{\,1}_{T,vis} - \vec{p}^{\,2}_{T,vis} \quad .$$

Thus, the zero jet and non-zero jet category have to be distinguished in the parametrisation comparison. Additionally, the decay modes of the hadronic τ leptons are distinguished to see the impact of the distinct parametrisation of the decay modes. The first comparison

is performed on the dataset that was used for the parametrisation. This provides a validation of the fitting procedure. Examples of comparisons can be found in Figure 7.12. These comparisons show that the peak position for the new parametrisation in the non-zero jet category is closer to the Z mass than for the old one. However, differences in the width of the distribution (standard deviation σ used as estimate) are small for MMC1 and MMC2. For MMC0 the new parametrisation results in a wider mass distribution in the non-zero jet category. For the zero jet category the distributions for the parametrisations hardly differ. Since MMC is provided with the reconstructed decay modes while the parametrisation uses truth decay modes, the reason for this missing resolution improvement could be decay mode misclassification. If another test, that provides MMC with the truth decay mode, reveals better resolution, the angular distributions for different truth decay modes can be combined according to the misclassification rate to correct for it. However, this second test (see Figure 7.13) shows no improvement of the resolution difference between old and new parametrisation.
Further investigation with a parametrisation with randomly changed parameters (with respect to the 2012 parametrisation) reveals a significant shift of the peak (see Figure 7.14) but only a relative small difference in the width of the mass distribution. This MMC behaviour suggests the MMC mass resolution is dominated by other effects. One possible effect could be the MET resolution. To study the impact of the MET resolution, the MMC solutions are constrained to $0.5\sigma_{MET}$ around the truth MET value. The results (see Figure 7.15) are a better peak position of the old parametrisation with respect to the standard $4\sigma_{MET}$ constraints and a slightly better resolution for the new parametrisation compared to the old parametrisation. Consequently, the MET resolution does not dominate the mass resolution. So either another effect, which has not been thought of, dominates the resolution or the differences among the decay modes are to small to recognize an improvement of the mass resolution. The improved width of the distributions with $0.5\sigma_{MET}$ compared to the standard $4\sigma_{MET}$ setting might falsely imply that $0.5\sigma_{MET}$ should be used as a default but the failure rate of MMC in $Z \to \tau\tau$ processes increases from 0.75 % to 13.7 % for both parametrisations.
In order to check the peak position in another sample, a parametrisation comparison is produced for a gluon fusion Higgs ($m_H = 125$ GeV) sample[2] at $\sqrt{s} = 13$ TeV with 50 ns bunch spacing. Using the PDF set CT10 [38], the sample is generated by PowHeg [21] and Pythia with the ANZLO [34] tune. The comparison (Figure 7.16) reveals a better peak position and a slightly worse width for the new parametrisation in the non-zero jet

[2] mc15_13TeV.341124.PowhegPythia8EvtGen_CT10_AZNLOCTEQ6L1_ggH125_tautauhh.merge.AOD.e3935_s2608_s2183_r6630_r6264

category. In the zero jet category there is almost no difference between the different sets of parametrisations. Because of small statistics the decay modes cannot be distinguished. In summary, a working parametrisation of the angular distributions of MMC has been achieved. The resulting reconstructed mass differs only slightly from the Run I parametrisation. Therefore, other sources than the MMC mass resolution have to be studied in order to reduce the resolution.

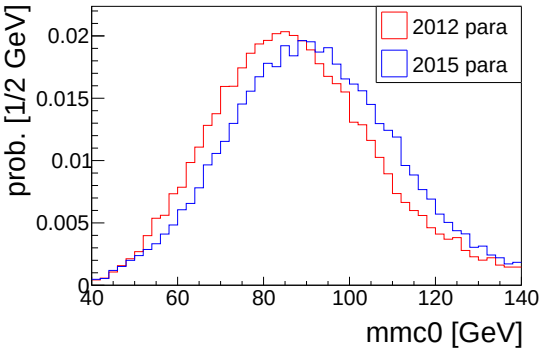

(a) >0-jet, $\sigma_{2012} = 18.6768$, $\sigma_{2015} = 19.0076$

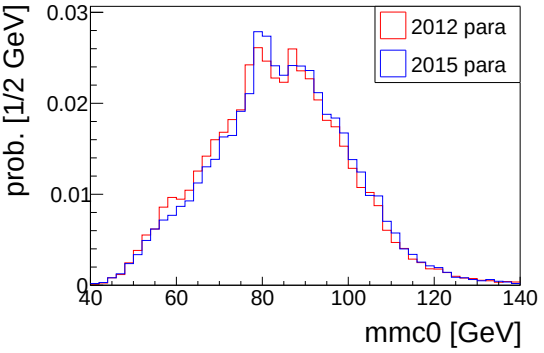

(b) 0-jet, $\sigma_{2012} = 15.9844$, $\sigma_{2015} = 15.8829$

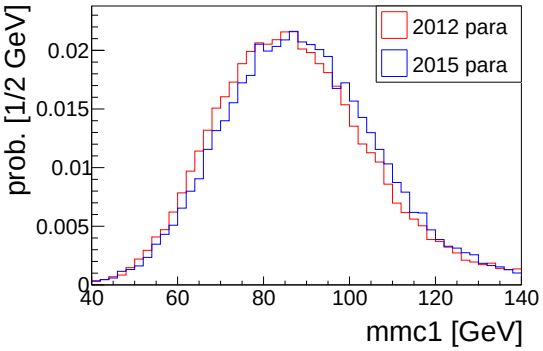

(c) >0-jet, $\sigma_{2012} = 17.7138$, $\sigma_{2015} = 17.6941$

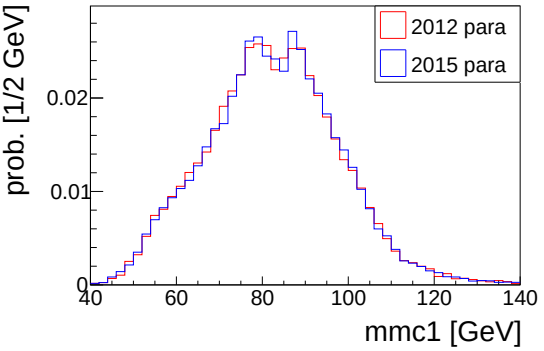

(d) 0-jet, $\sigma_{2012} = 15.3523$, $\sigma_{2015} = 15.3568$

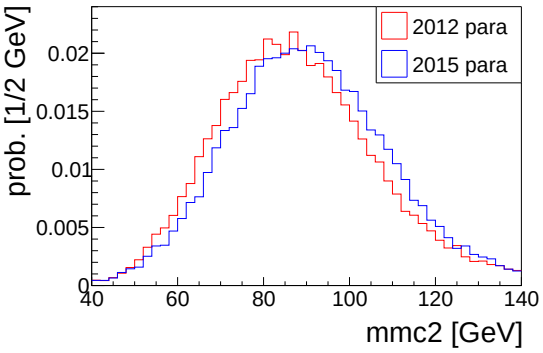

(e) >0-jet, $\sigma_{2012} = 18.0847$, $\sigma_{2015} = 18.0752$

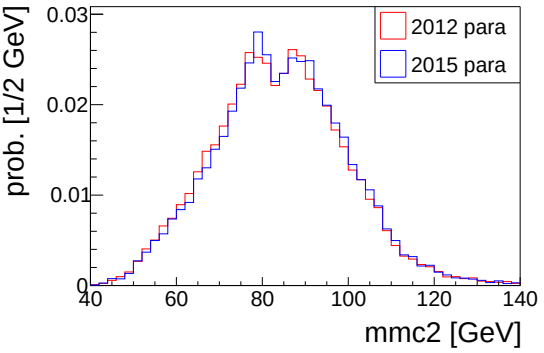

(f) 0-jet, $\sigma_{2012} = 15.3788$, $\sigma_{2015} = 15.2798$

Figure 7.12.: MMC mass distributions for reconstructed decay mode 1p0n for the first τ lepton and 1p1n for the second. The underlying $Z \to \tau\tau$ sample is generated with POWHEG and PYTHIA at $\sqrt{s} = 13$ TeV with 50 ns bunch spacing. The peak position of the new parametrisation is better in the non-zero jet category, but the width does not improve.

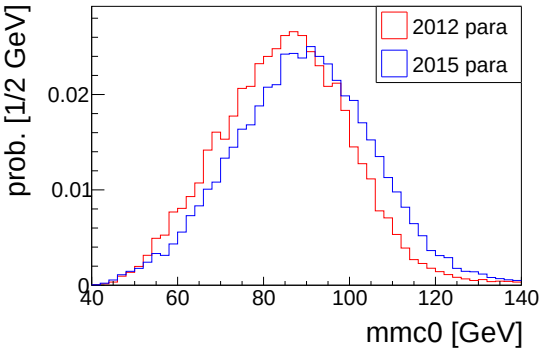

(a) >0-jet, $\sigma_{2012} = 15.1371$, $\sigma_{2015} = 16.2186$

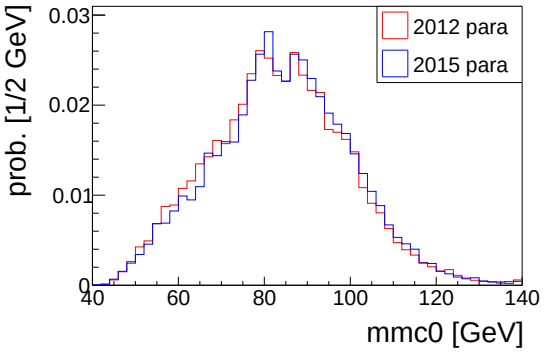

(b) 0-jet, $\sigma_{2012} = 16.0028$, $\sigma_{2015} = 15.9124$

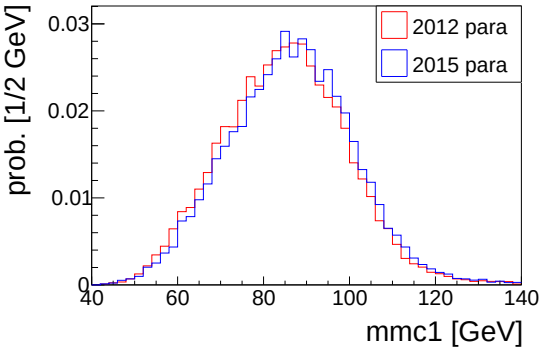

(c) >0-jet, $\sigma_{2012} = 14.3385$, $\sigma_{2015} = 14.406$

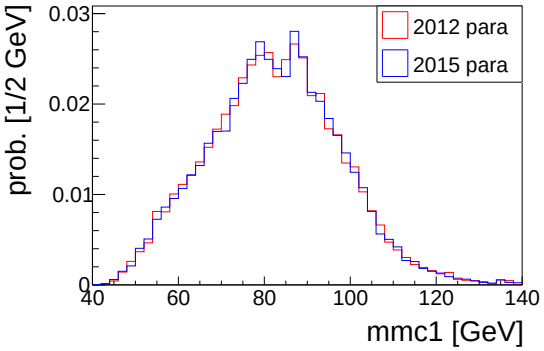

(d) 0-jet, $\sigma_{2012} = 15.3871$, $\sigma_{2015} = 15.3281$

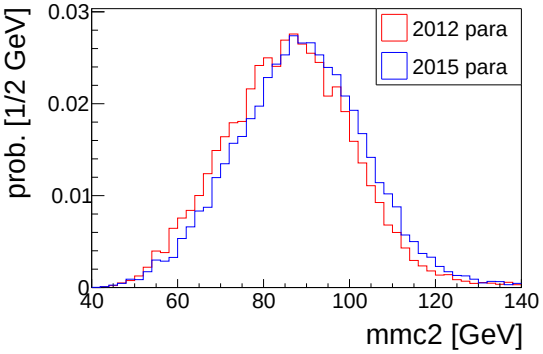

(e) >0-jet, $\sigma_{2012} = 14.7605$, $\sigma_{2015} = 15.0108$

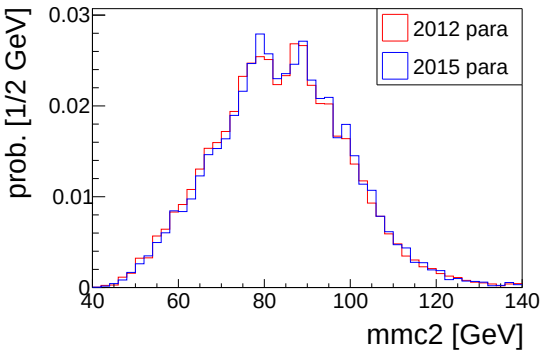

(f) 0-jet, $\sigma_{2012} = 15.414$, $\sigma_{2015} = 15.3164$

Figure 7.13.: MMC mass distributions for truth decay mode 1p0n for the first τ lepton and 1p1n for the second. The underlying $Z \to \tau\tau$ sample is generated with POWHEG and PYTHIA at $\sqrt{s} = 13$ TeV with 50 ns bunch spacing. The width of the distributions decreases with respect to distributions for reconstructed decay modes, but still there is only a small difference among the parametrisations.

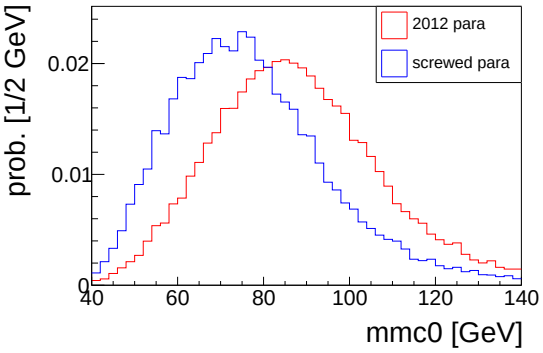

(a) >0-jet, $\sigma_{2012} = 18.6768$, $\sigma_{\text{screw}} = 18.0378$

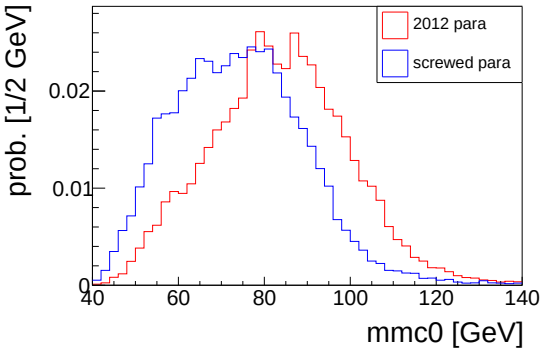

(b) 0-jet, $\sigma_{2012} = 15.9844$, $\sigma_{\text{screw}} = 15.1781$

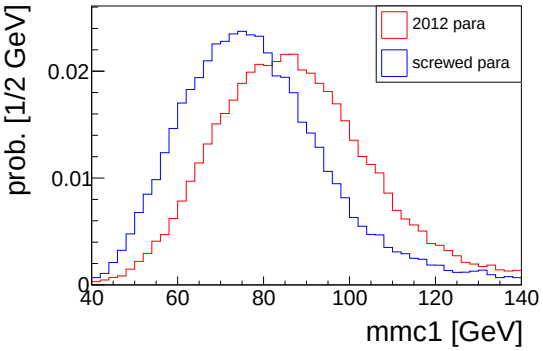

(c) >0-jet, $\sigma_{2012} = 17.7138$, $\sigma_{\text{screw}} = 17.1597$

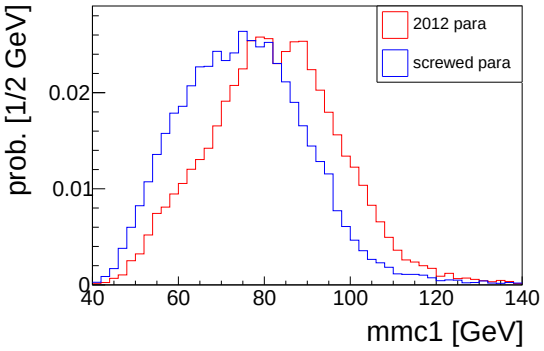

(d) 0-jet, $\sigma_{2012} = 15.3523$, $\sigma_{\text{screw}} = 14.7109$

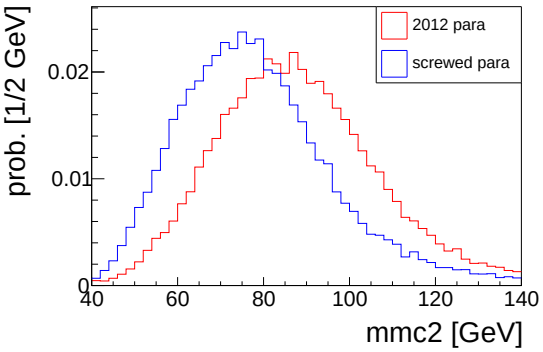

(e) >0-jet, $\sigma_{2012} = 18.0847$, $\sigma_{\text{screw}} = 17.5919$

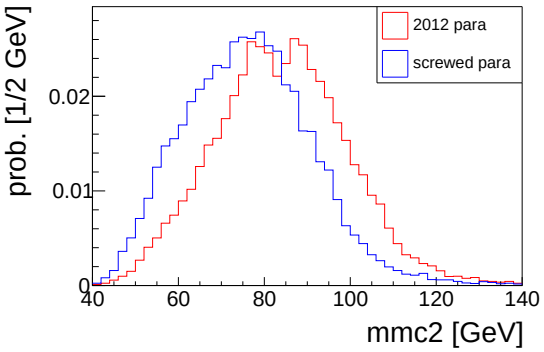

(f) 0-jet, $\sigma_{2012} = 15.3788$, $\sigma_{\text{screw}} = 14.7755$

Figure 7.14.: MMC mass distributions for reconstructed decay mode 1p0n for the first τ lepton and 1p1n for the second. The underlying $Z \to \tau\tau$ sample is generated with POWHEG and PYTHIA at $\sqrt{s} = 13$ TeV with 50 ns bunch spacing. The "screwed" parametrisation is a 2012 parametrisation with random parameters changed. The parameter change affects mainly the peak position and not the width.

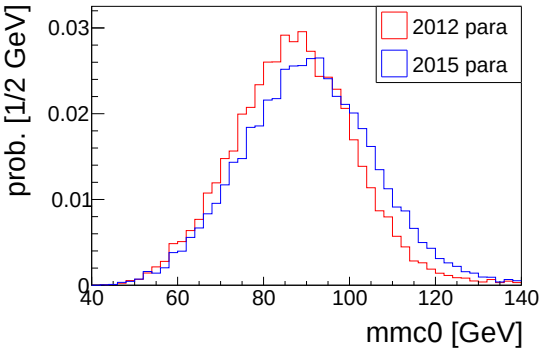

(a) >0-jet, $\sigma_{2012} = 14.0205$, $\sigma_{2015} = 15.2423$

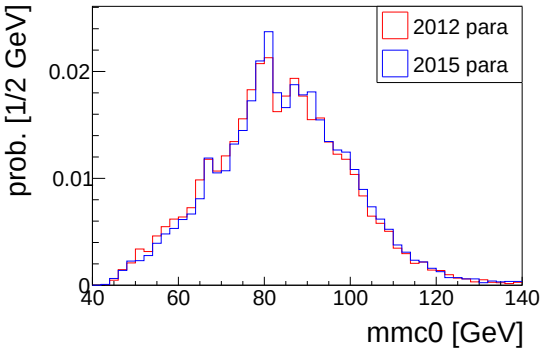

(b) 0-jet, $\sigma_{2012} = 15.7524$, $\sigma_{2015} = 15.6582$

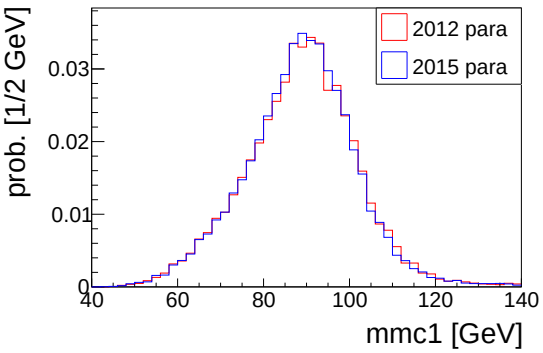

(c) >0-jet, $\sigma_{2012} = 12.9721$, $\sigma_{2015} = 12.7825$

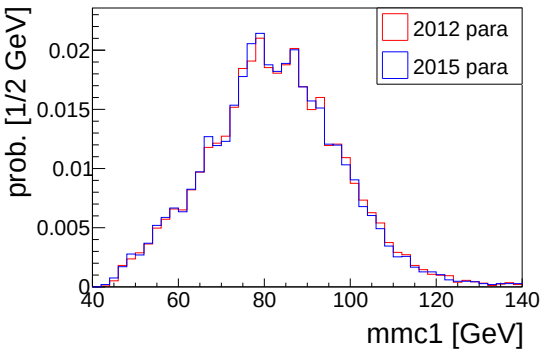

(d) 0-jet, $\sigma_{2012} = 15.4335$, $\sigma_{2015} = 15.3771$

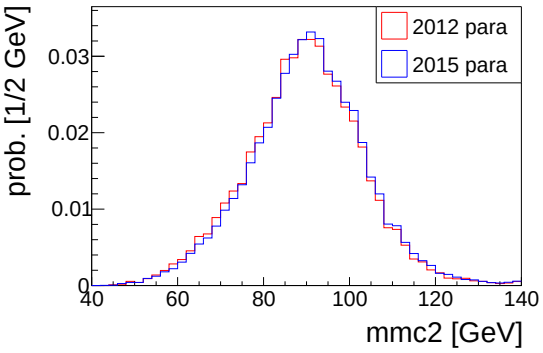

(e) >0-jet, $\sigma_{2012} = 13.4035$, $\sigma_{2015} = 13.3828$

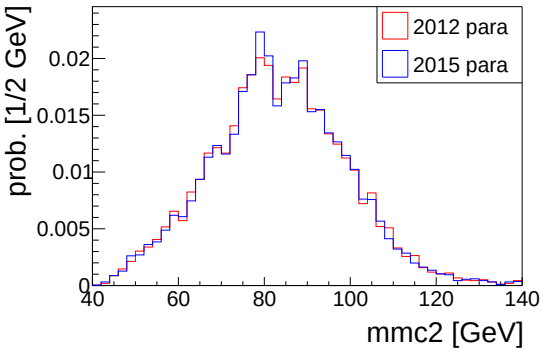

(f) 0-jet, $\sigma_{2012} = 15.7378$, $\sigma_{2015} = 15.6213$

Figure 7.15.: MMC mass distributions for $0.5\sigma_{MET}$ and truth decay mode 1p0n for the first τ lepton and 1p1n for the second. The underlying $Z \to \tau\tau$ sample is generated with POWHEG and PYTHIA at $\sqrt{s} = 13$ TeV with 50 ns bunch spacing. Constraining the parameter space to $0.5\sigma_{MET}$ results in a slightly better width for the new parametrisation.

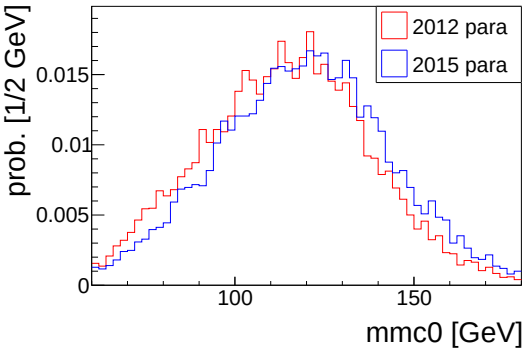

(a) >0-jet, $\sigma_{2012} = 22.9181$, $\sigma_{2015} = 23.3397$

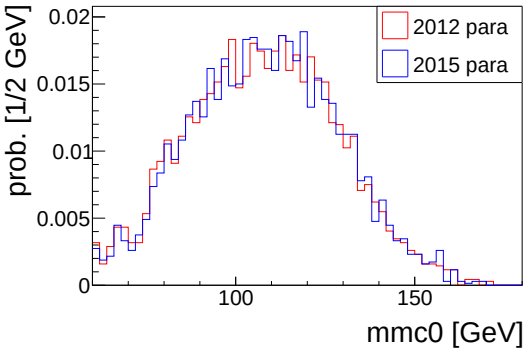

(b) 0-jet, $\sigma_{2012} = 20.6086$, $\sigma_{2015} = 20.3885$

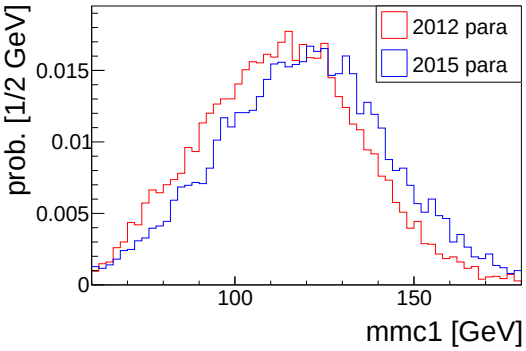

(c) >0-jet, $\sigma_{2012} = 22.078$, $\sigma_{2015} = 23.3397$

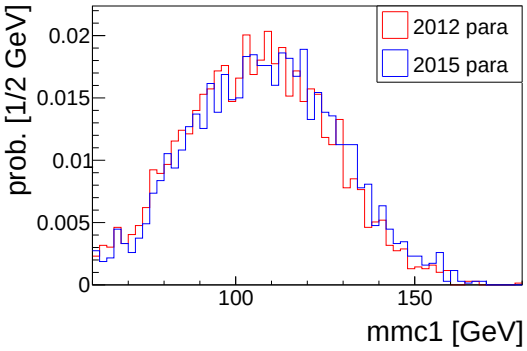

(d) 0-jet, $\sigma_{2012} = 19.9334$, $\sigma_{2015} = 20.3885$

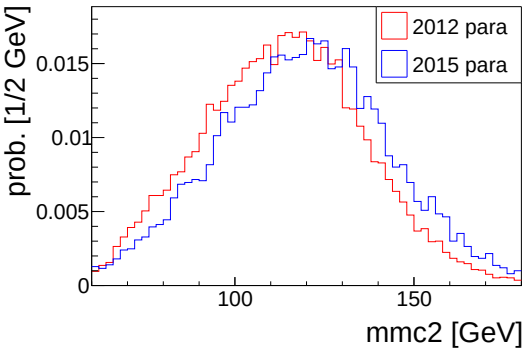

(e) >0-jet, $\sigma_{2012} = 22.2642$, $\sigma_{2015} = 23.3397$

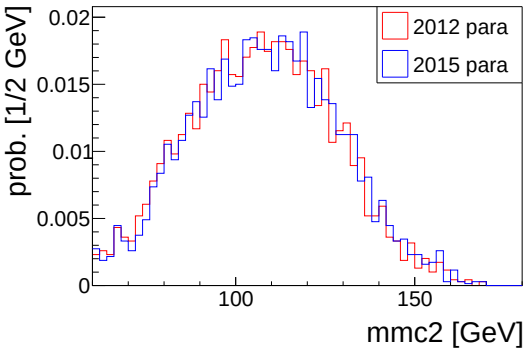

(f) 0-jet, $\sigma_{2012} = 20.2496$, $\sigma_{2015} = 20.3885$

Figure 7.16.: MMC mass distributions for gluon fusion Higgs events. The underlying $H \to \tau\tau$ sample is generated with POWHEG and PYTHIA at $\sqrt{s} = 13$ TeV with 50 ns bunch spacing. The new parametrisation yields a more accurate peak position for this Higgs process.

8. $Z \to \tau\tau$ analysis

$Z \to \tau\tau$ is the main irreducible background for $H \to \tau\tau$ searches and as such detailed studies are required towards understanding it further and eventually suppressing its contribution. The aim of the second part of this thesis is to study this background in the semi-leptonic (one leptonically and one hadronically decaying τ lepton) channel at $\sqrt{s} = 13$ TeV and measure the cross section of the $Z \to \tau\tau$ process. The samples used during this analysis are given in Table B.2.

8.1. First Run II data

After the long upgrade phase a beam energy of 6.5 TeV was reached at the end of May and first 13 TeV collisions were observed at the beginning of June. At the end of June the LHC started operation with 50 ns bunch spacing. In the following weeks the beam intensity was increased, such that the integrated luminosity strongly increased (see Figure 8.1). At the end of July LHC was stopped again and 25 ns bunch spacing was prepared.

This analysis uses 50 ns data recorded between the 13th of June and the 16th of July, corresponding to the runs 267639, 270806, 270953, 271048, 271298, 271421, 271516, 271595, 271744 and 267638. Data samples are filtered according to the Good Run List (GRL) which marks recorded luminosity blocks as good if the data quality requirements (detector performance and beam status) are fulfilled. Taking this filtering into account, the integrated luminosity of the analysed data is $\mathcal{L}_{int} = 85$ pb^{-1}.

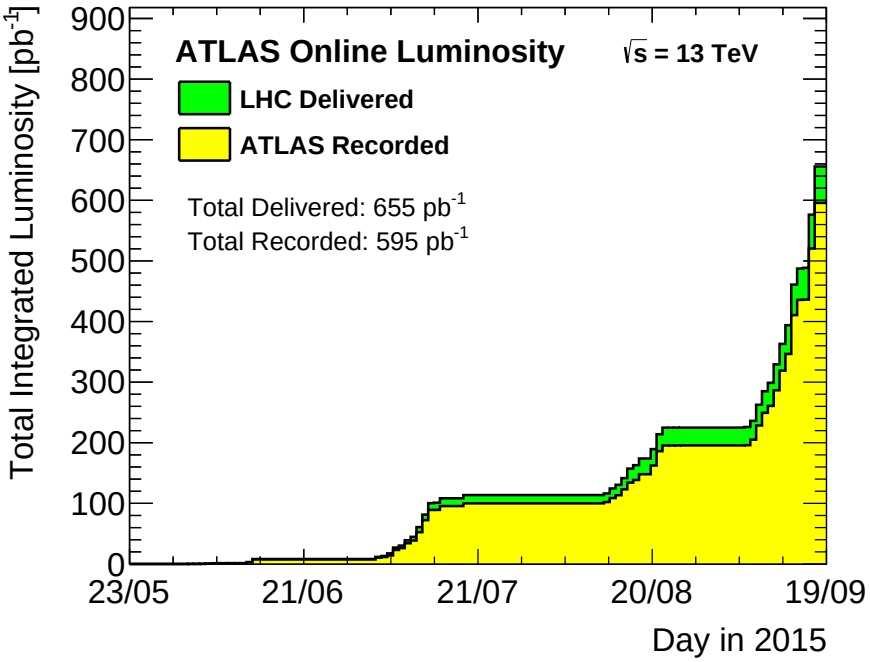

Figure 8.1.: Integrated luminosity versus date [39].

8.2. Derivations

Since data or MC samples containing all events and all of their information are really large in terms of disk space consumption (e. g. 10 TB for 20 M events), one tries to reduce the size of the samples in several ways:

- **Skimming:** Not all events are interesting for the considered analysis, so that size can be reduced by throwing away all uninteresting events.
- **Slimming:** For a particular analysis not all information or all particles are needed. Thus, deleting unnecessary containers or variables shrinks the sample.
- **Thinning:** Similarly objects which fulfill certain criteria (e. g. low p_T tracks) can be removed from the event.

Another advantage of skimming is the decreased computing time because fewer events have to be processed. The shrinked samples are called derivations. The event selection cuts of the HIGG4D2 derivation, that is used in this thesis, are listed in Table 8.1.

channel	cut
Skimming cut	$\#(\tau_{had}) \geq 1 \wedge \#(\mu) + \#(e) \geq 1$
τ_{had}	$(p_T(\tau) \geq 18$ GeV $\wedge \#(tracks) \in \{1, 3\}$
μ	$p_T(\mu) \geq 13$ GeV $\wedge$ DFCommonGoodMuon
e	$p_T(e) \geq 15$ GeV $\wedge$ (isEMedium $\vee$ LHMedium)

Table 8.1.: Skimming cuts for the HIGG4D2 derivations. $\#(\tau_{had})$ means number of hadronic τ leptons, "isEMedium" and "LHMedium" specify quality criteria for electrons and "DFCommonGoodMuon" is a combination of η, quality and IDHits (number of hits in the inner detector) criteria. For electron and muon identification see [25–28].

8.3. Object definition for the $Z \to \tau\tau$ analysis

Electrons: Electrons are required to pass a cut on the transverse momentum of $p_T > 25$ GeV and match the tight likelihood-based identification (see section 6). Furthermore, the electron has to be in a pseudorapidity range of $|\eta| < 2.47$ excluding the crack region of the calorimeter $1.37 < |\eta| < 1.52$.

Muons: The p_T threshold for muons is 21 GeV . Additionally, $|\eta| < 2.42$ and a medium quality is required (see section 6). Moreover, the muon track has to pass some quality cuts specified in [27].

Hadronic τ leptons: Hadronically decaying τ leptons are required to pass $p_T > 20$ GeV and $|\eta| < 1.37$ or $1.52 < |\eta| < 2.5$. Further cuts are $|q| = 1$ and $N_{tracks} \in \{1, 3\}$, where q is the charge of the τ candidate. A JetBDT working point is not required at this stage because all τ candidates are needed to construct the multi-jet fake estimate (see section 8.7), but τ leptons in the signal region have to pass the medium JetBDT working point (see section 6).
To reliably reject electrons faking τ leptons, an electron overlap removal is used. For this method the candidate is reconstructed as an electron and a 1 prong hadronic τ lepton in parallel. If the electron likelihood exceeds a value dependent on p_T and η, the hadronic τ candidate is dismissed.

Overlap removal: If a muon overlaps ($\Delta R < 0.2$) with an electron, the electron is dropped. The same applies for a τ lepton that overlaps ($\Delta R < 0.4$) with a muon and jets overlapping ($\Delta R < 0.2$) with muons, electrons or τ leptons.

8.4. Triggers

Triggers are used to select interesting collision events (see section 4.2.4). In order properly define the subset that is used in an analysis, a trigger or a combination of triggers has to be used. To reduce the trigger rate, triggers can be prescaled, meaning the trigger fires only in a certain fraction of events that would pass the trigger requirements. This changes the effective luminosity of the sample.
This analysis uses the lowest unprescaled single lepton triggers (as of September 2015). The muon is required to pass the HLT_mu20_iloose_L1MU15 trigger. "HLT" indicates a high level trigger, "mu20" encodes the p_T threshold of the muon, "iloose" specifies the isolation criterion (see section 8.6 for the isolation variable) and "L1MU15" the L1 trigger, that seeds this HLT trigger. HLT_e24_lhmedium_iloose_L1EM20VH is used in the electron channel, where "lhmedium" refers to the likelihood-based quality of the electron and L1EM20VH is the seeding L1 trigger. "H" refers to hadronic core isolation and "V" to η-dependent thresholds (accounts for energy loss).

8.5. Backgrounds

Feynman diagrams for all considered backgrounds can be found in Figures 8.2 to 8.4. As described below all depicted final states can be (mis-)identified as signal final state.

$Z \to \ell^+\ell^-$: This background shares some properties like the negative charge correlation of the decay products with the signal $Z \to \tau_{had}\tau_{lep}$. Since the leptons do not originate from decays inside a jet, the leptons from this background are isolated (small activity close to the lepton). An important difference from the signal is the di-leptonic final state of this background. Electrons, however, can fake 1 prong decays of τ leptons. In the case of muons, a jet can fake a hadronic τ lepton and one of the muons remains undetected.

W+jets: Leptonic W decays can mimic the signal topology if a jet fakes a hadronic τ lepton. Furthermore, the W boson can decay into a hadronic τ lepton while a jet fakes an electron or muon. The suppression of such background events is described in section 8.6.

$t\bar{t}$ and single top: Because the top quark decays via a W boson, in $t\bar{t}$ events and single top events with associated W boson production the final state of the signal can be reproduced if one W boson decays into a hadronically decaying τ lepton and the other

one into an electron or muon. Thus, this is an important irreducible background. For other single top events a jet can fake the hadronic τ lepton or the electron. While the $t\bar{t}$ process is an important process, the cross sections of the single top processes ($\mathcal{O}(10\text{ nb})$) are small compared to the signal cross section ($\mathcal{O}(1000\text{ nb})$). For completeness both are considered.

Multi-jet: QCD multi-jet events can fake signal events if two jets are misidentified as lepton and hadronic τ lepton. The high cross section for this background compensates the small probability of those multiple fakes. Consequently, multi-jets constitute an important background contribution. While the other backgrounds and the signal are described by simulation, this is not possible for the multi-jet background because of large theoretical uncertainties. Thus, a data-driven estimate is used (see section 8.7).

Further backgrounds: Di-boson processes and the Higgs process $H \to \tau\tau$ contribute as backgrounds. Their cross sections are so small ($\mathcal{O}(10\text{ nb})$) that they are neglected.

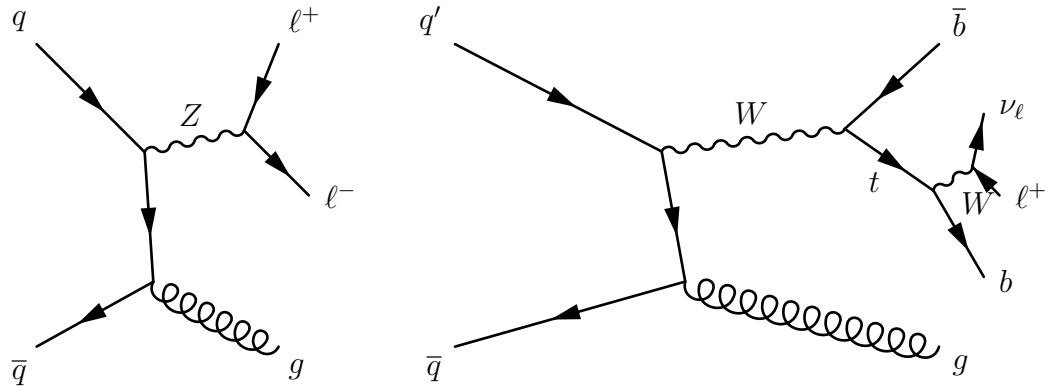

Figure 8.2.: $Z \to \ell^+\ell^-$ Feynman diagram (left) and single top Feynman diagram (right).

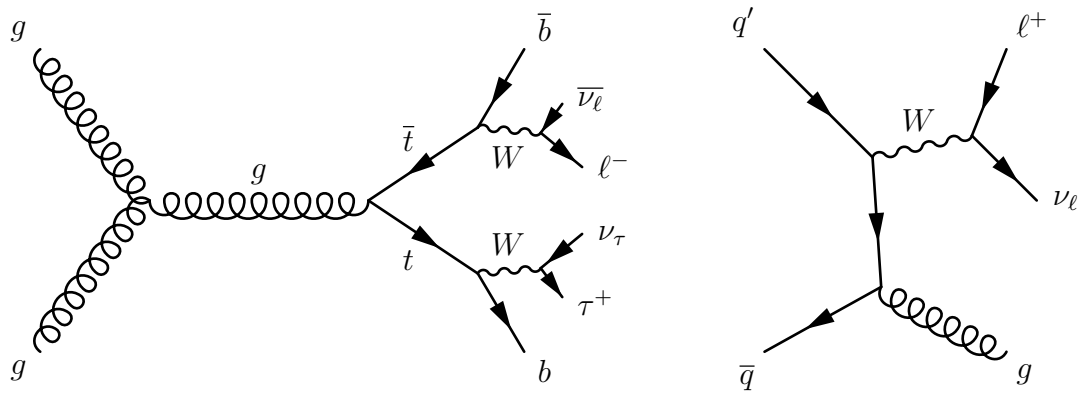

Figure 8.3.: $t\bar{t}$ Feynman diagram (left) and W+jets Feynman diagram (right).

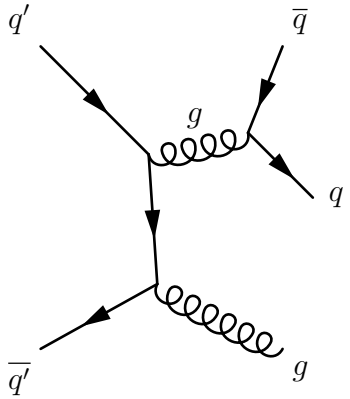

Figure 8.4.: Example of a multi-jet Feynman diagram.

8.6. Selection cuts

First of all, events have to pass the skimming cuts of the HIGG4D2 derivation (see Table 8.1). Then at least one hadronic τ and a lepton, that pass the definitions described in section 8.3, are required. This $\tau_{lep}\tau_{had}$ selection is a tighter collection of cuts than the skimming cuts. Additionally, at least one primary interaction vertex has to be identified and the respective electron or muon trigger has to be passed. Afterwards the following cuts are applied to reject background events and construct the signal region.

Opposite Sign (OS): The hadronic τ lepton and the lepton are required to have opposite charge. This suppresses multi-jet background with positive charge correlation, while Z boson decays with negative charge correlation should pass the filter (see Figure 8.5). Furthermore, a fraction ($\approx 1/3$) of W+jets is rejected.

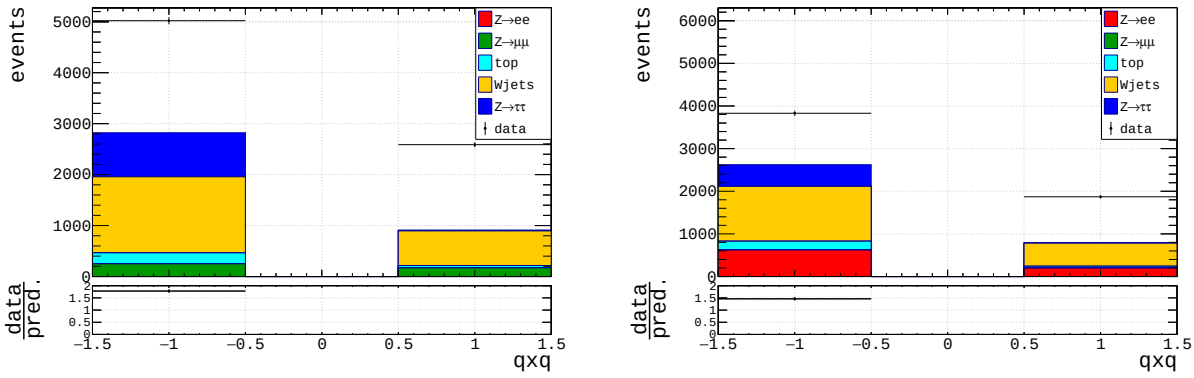

(a) Muon channel *(b)* Electron channel

Figure 8.5.: Product of charges before OS selection and right after the basic $\tau_{lep}\tau_{had}$ selection. The dots correspond to data, the histograms represent the MC prediction simulated with POWHEG and PYTHIA. Multi-jet background is expected to fill the gap between data and MC.

Di-lepton veto (2LV): The di-lepton veto is directed at $Z \to \ell^+\ell^-$ ($\ell \in \{e, \mu\}$) events. Additionally, it rejects di-leptonic decays stemming from $Z \to \tau\tau$ events (see Figure 8.6).

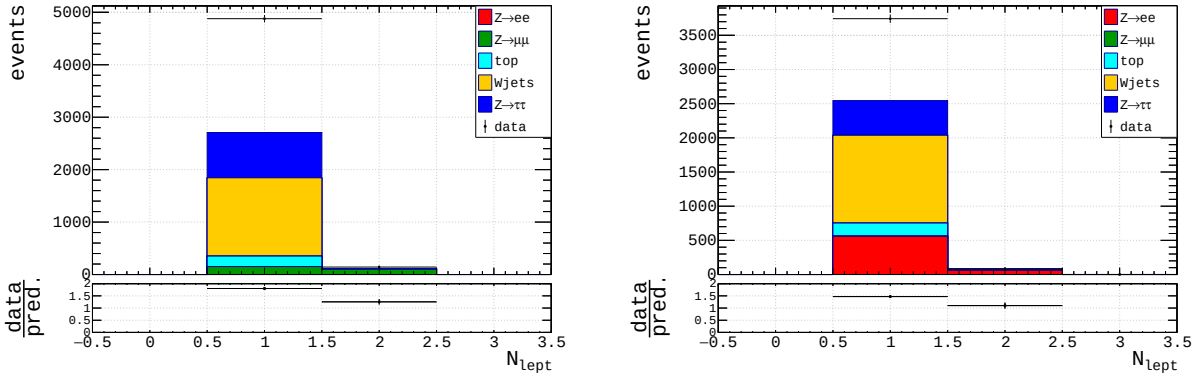

(a) Muon channel *(b)* Electron channel

Figure 8.6.: Number of leptons (μ, e) before the di-lepton veto and right after the OS selection. The other details are the same as in Figure 8.5.

Isolation (Iso): The isolation of a lepton is calculated using the tracks (or the calorimeter cells) in a ΔR cone around the lepton track. The p_T sum of the tracks (the transverse energy of the cells) is divided by the p_T (transverse energy) of the lepton. This ratio has to be smaller than an upper threshold. Here a tight isolation working point corresponding to signal efficiency of 95 % is chosen. The isolation cut suppresses events with jets, that contain a lepton from hadron decays (see Figure 8.7).
The trigger isolation requirement "iloose" is $\frac{\text{ptcone20}}{p_T} < 0.10$ for electrons and $\frac{\text{ptcone20}}{p_T} < 0.12$

for muons where ptcone20 is the p_T sum in a $\Delta R = 0.2$ cone around the lepton track excluding the lepton track itself.

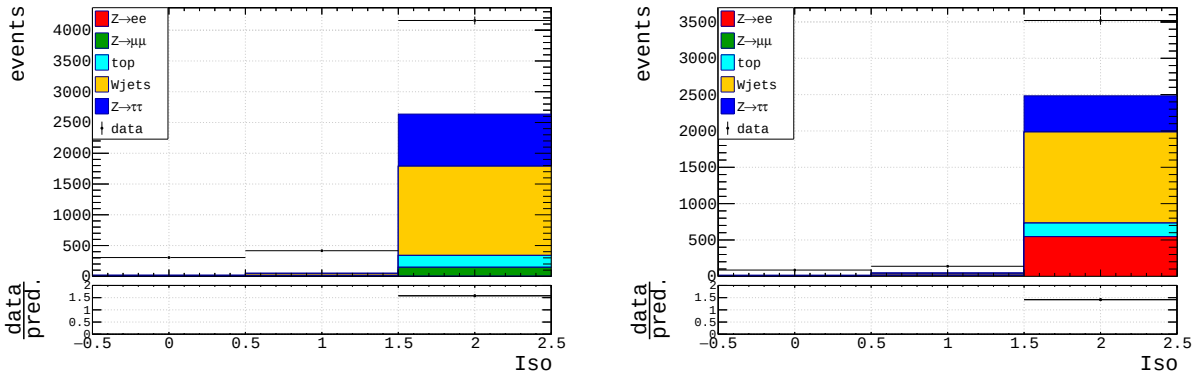

(a) Muon channel ***(b)*** Electron channel

Figure 8.7.: Lepton isolation before isolation cut and right after the di-lepton veto. A value of zero means no isolation working point is passed, a value of one stands for "loose" isolation only and two for "tight" isolation. The other details are the same as in Figure 8.5. Multi-jet background is expected to fill the gap between data and MC.

Sum of the cosines of azimuthal distances to MET $\sum_{i=\tau,\ell} \cos\Delta\phi(i, \vec{\not{p}}_T)$: In $Z \to \tau\tau$ events the neutrinos are most likely emitted close to the direction of the visible decay products. Therefore, $\vec{\not{p}}_T$ is expected to lie in between the visible decay products (in the transverse plane). Hence, $\sum_{i=\tau,\ell} \cos\Delta\phi(i, \vec{\not{p}}_T)$ should be close to or larger than zero for signal events. In W+jets events a jet typically fakes the hadronic τ lepton. This jet has to balance with lepton and neutrino in the transverse plane (see Figure 8.8). Thus $\sum_{i=\tau,\ell} \cos\Delta\phi(i, \vec{\not{p}}_T)$ is typically negative in W+jets events (see Figure 8.9). In order to keep as many signal events as possible, a cut of $\sum_{i=\tau,\ell} \cos\Delta\phi(i, \vec{\not{p}}_T) > -0.15$ is applied.

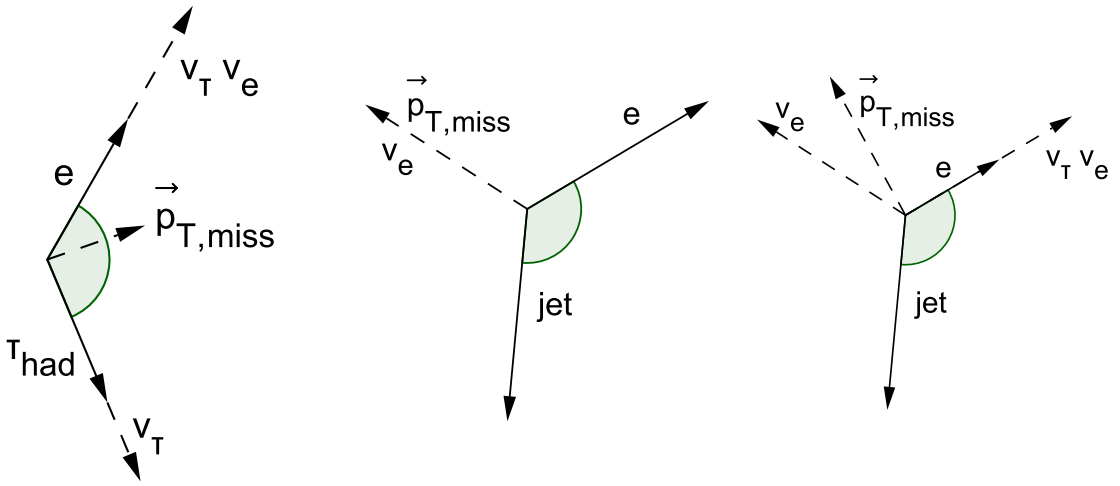

(a) $Z \to \tau_{had}\tau_{lep}$ *(b)* $W \to \nu_\ell \ell$ *(c)* $W \to \nu_\tau \tau_{lep}$

Figure 8.8.: Typical angular configurations in the transverse plane for $Z \to \tau\tau$ and W+jets. The sketches are labeled for electrons but apply for muons too.

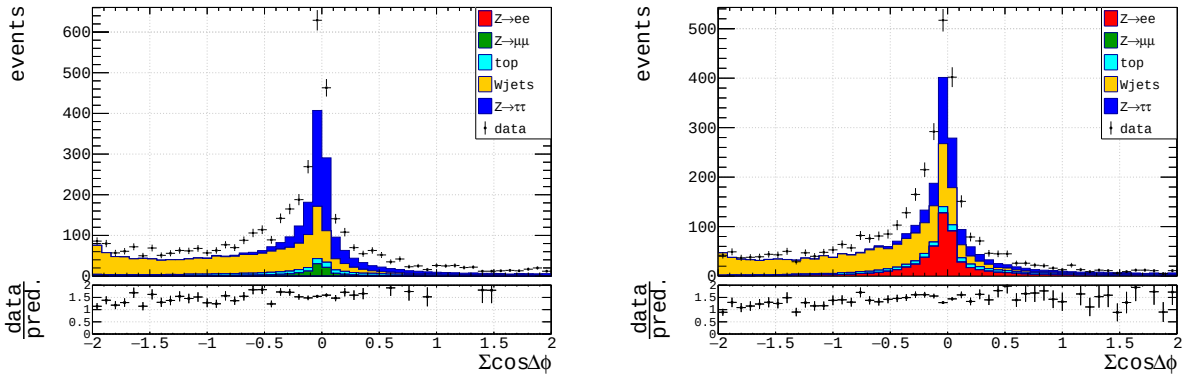

(a) Muon channel *(b)* Electron channel

Figure 8.9.: $\sum_{i=\tau,\ell} \cos\Delta\phi(i, \vec{\not{p}}_T)$ variable before applying a cut on this variable and right after the application of the isolated lepton cut. The other details are the same as in Figure 8.5.

Transverse mass m_T: In leptonic ($\ell \in \{e, \mu\}$) W decays the upper bound of the transverse mass $m_T = \sqrt{2p_T^\ell \not{p}_T (1 - \cos\Delta\phi(\vec{p}_T^{\,\ell}, \vec{\not{p}}_T))}$ is m_W in the absence of energy or momentum smearing effects. If the decay products completely lie in the transverse plane, $\vec{\not{p}}_T$ is the complete neutrino momentum and $\vec{p}_T^{\,\ell}$ the complete lepton momentum. In this case the upper bound is reached. Because of the detector resolution this upper bound is smeared out. Processes, that involve virtual W bosons (momentum transfer $q^2 \neq m_W^2$), do not have this constraint but are suppressed by propagator. Thus, one expects a high

transverse mass ($\sim$ 80 GeV) for W+jets events. Since m_T is smaller for $Z \to \tau\tau$ events (see Figure 8.10), a cut of $m_T < 50$ GeV is applied.

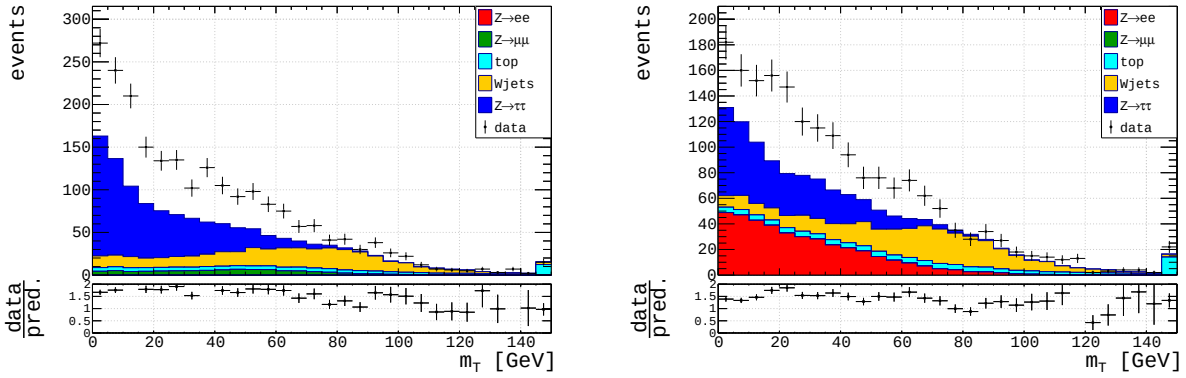

(a) Muon channel ***(b)*** Electron channel

Figure 8.10.: Transverse mass before applying a cut on this variable and right after the application of the $\sum_{i=\tau,\ell} \cos\Delta\phi(i, \not{p}_T)$ cut. Last and first bin contain additionally the contribution of overflow bin and underflow respectively. The other details are the same as in Figure 8.5.

Azimuthal distance $\Delta\phi(\ell, \tau)$: As shown in Figure 8.11 the signal distribution peaks at large $\Delta\phi(\ell, \tau)$. Consequently, a cut $\Delta\phi(\ell, \tau) > 1.57$ is introduced.

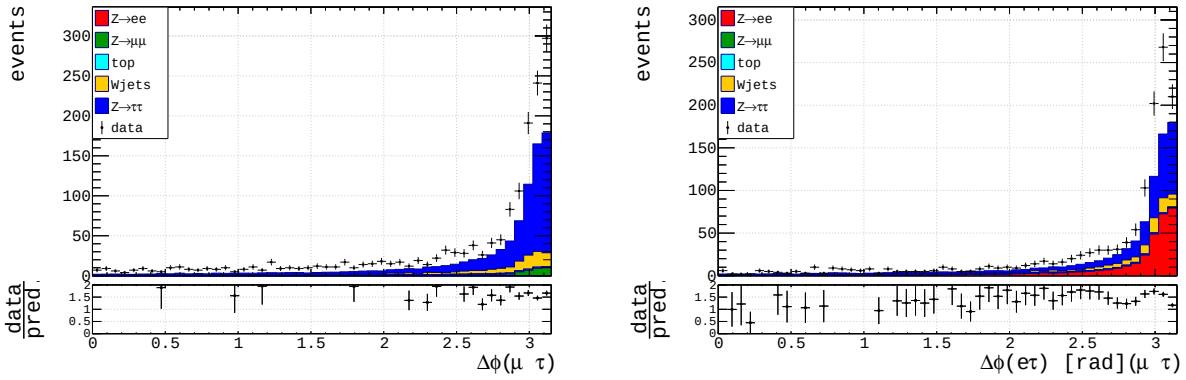

(a) Muon channel ***(b)*** Electron channel

Figure 8.11.: $\Delta\phi(\ell, \tau)$ variable before applying a cut on this variable and right after the application of the m_T cut. The other details are the same as in Figure 8.5.

The invariant mass m_{vis} calculated from the visible decay products (Figure 8.12) shows a significant $Z \to ee$ contribution in the electron channel. This contribution is probably caused by electrons faking hadronic τ leptons since the visible mass of the electron and the τ candidate peaks at the Z mass. A jet faking a τ lepton is not expected to be correlated to an electron in such a way that the invariant mass peaks at the Z mass. Thus, the

electron τ fakes do not seem to be completely understood. However, this large $Z \to ee$ contribution is also present for 3 prong τ leptons. But it is very unlikely, that an electron with a single track can fake a object with three tracks. Such a behaviour could be caused by incorrectly associated tracks and has to be studied further. However, such studies are outside the scope of this analysis.
In order to suppress the $Z \to ee$ contribution for the cross section measurement, an additional cut of $m_{vis} < 80$ GeV is introduced.

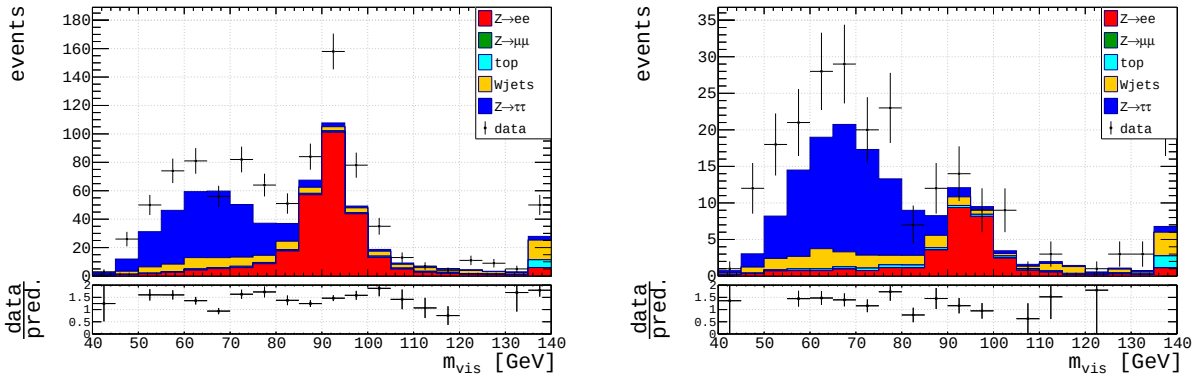

(a) 1 prong τ ***(b)*** 3 prong τ

Figure 8.12.: m_{vis} distribution in the signal region of the electron channel. The other details are the same as in Figure 8.5.

8.6.1. Event cutflow

The cutflow is summarised in the Tables 8.2 and 8.3. For every cut the fraction of signal events passing the cuts (signal efficiency) and the fraction of simulated background events failing the cuts (background rejection) is given there. Besides the efficiency and rejection of every single cut the total efficiency and rejection is provided for every step in the cutflow.
Since the QCD background is estimated for the signal region, it is missing in the previous steps of the cutflow. Therefore, the calculation of the significance $Z = \frac{S}{\sqrt{B}}$ where S and B are the number of signal and background events would be unreasonable.

Cut	Tot. Back. rej.	Tot. sig. eff.	Back. rej.	Sig. eff.
lephad selection	0.999479(10)	0.00534(18)	0.999479(10)	0.00534(18)
OS	0.999642(9)	0.00524(18)	0.314(9)	0.980(5)
2LV	0.999663(8)	0.00523(18)	0.058(6)	0.9992(10)
Isolation	0.999673(8)	0.00513(18)	0.030(4)	0.981(5)
$\sum_{i=\tau,\ell} \cos\Delta\phi(i, \not{p}_T)$	0.999893(5)	0.00436(15)	0.672(11)	0.849(13)
m_T	0.9999578(28)	0.00392(14)	0.606(21)	0.900(12)
$\Delta\phi(\ell, \tau)$	0.9999643(26)	0.00371(13)	0.155(24)	0.945(9)

Table 8.2.: Background rejection of the MC simulated background and signal efficiency for every cut in the cutflow of the muon channel and total rejection and efficiency at each step. The quoted errors of the efficiencies ϵ are binomial errors $\sigma_\epsilon = \sqrt{\epsilon(1-\epsilon)/N}$, where N is the number in the denominator of ϵ.

Cut	Tot. Back. rej.	Tot. sig. eff.	Back. rej.	Sig. eff.
lephad selection	0.999471(10)	0.00315(14)	0.999471(10)	0.00315(14)
OS	0.999614(9)	0.00308(14)	0.270(9)	0.977(7)
2LV	0.999628(9)	0.00307(14)	0.036(5)	0.9989(15)
Isolation	0.999637(9)	0.00302(14)	0.026(4)	0.982(6)
$\sum_{i=\tau,\ell} \cos\Delta\phi(i, \not{p}_T)$	0.999841(6)	0.00255(12)	0.563(12)	0.844(17)
m_T	0.999910(5)	0.00225(10)	0.432(17)	0.886(16)
$\Delta\phi(\ell, \tau)$	0.999918(4)	0.00208(10)	0.091(13)	0.924(14)
m_{vis}	0.9999831(18)	0.00183(9)	0.793(20)	0.880(18)

Table 8.3.: Background rejection of the MC simulated background and signal efficiency for every cut in the cutflow of the electron channel and total rejection and efficiency at each step. The quoted errors of the efficiencies ϵ are binomial errors $\sigma_\epsilon = \sqrt{\epsilon(1-\epsilon)/N}$, where N is the number in the denominator of ϵ.

8.7. Estimating the fake τ lepton background

To construct a data-driven multi-jet estimate, one should not use data events from the actual signal region. Otherwise, all the potential difference between data and simulated events would be absorbed in the fake estimate. The idea of the fake factor method is to estimate the multi-jet contribution in the region of τ leptons that pass the medium jet BDT cut (ID region) using (data) events that fail the BDT cut (denoted as anti-ID or

!ID). The multi-jet estimate is determined by inverting the BDT cut but keeping all other signal region cuts. The anti-ID region is expected to contain more multi-jet events (see Figure 8.13) because the cut on a BDT that is trained to reject QCD jets is inverted. The expected fraction of other backgrounds are subtracted from the data. This yields the shape of the estimate.
The transition from anti-ID to ID region is then performed using fake factors FF. These are calculated as the ratio of ID and anti-ID events (N_{ID} and $N_{!ID}$) in a multi-jet enriched region

$$\mathrm{FF} = \frac{N_{ID}}{N_{!ID}} \quad ,$$

where the numbers N_{ID} and $N_{!ID}$ are corrected for the remaining contribution of other backgrounds.
A multi-jet enriched region is defined by inverting the tight lepton isolation cut (see Figure 8.14). Nevertheless, the looser isolation cuts of the triggers are still applied. Again contributions of other backgrounds are subtracted from data. Since the τ identification is p_T-dependent, the fake factors are binned in $p_T(\tau)$.
The fake factors as a function of the τ lepton's p_T are shown in Figure 8.15 and the fake estimate in Figures 8.17 to 8.24. In order to verify the fake factor method, it is tested in another region with large multi-jet contribution. This fake estimate validation region is constructed by inverting the OS criterion and retaining the other signal region cuts. While $q\overline{q}$ events exhibit a negative charge correlation, qg events do not have any charge correlation. Thus, the fraction of multi-jet events in the same sign (SS) region is similar in size as in the OS region, whereas contributions from $Z \to \tau\tau$ are suppressed (see Figure 8.16). The validation of the fake estimate is performed using fake factors obtained from the SS, anti-isolated region (see Figure 8.16). Since the description by the fake estimate is good for the muon channel, the method can be applied in this channel. The remaining non-closure in the SS region is accounted for as a systematic error of the fake estimate (see section 8.8.1).
The non-closure in the electron channel is much larger. This could be an additional contribution from electrons faking hadronic τ leptons, which are not yet well understood in 2015 Atlas data. Additionally, the number of selected events in the electron channel is much smaller (see Figure 8.14) because of the higher p_T threshold of the electron trigger. The non-closure will be accounted for by the systematic error of the fake estimate. This does not correct the central value of calculations performed in the electron channel but will enlarge the errors to account for the imperfect fake estimate.

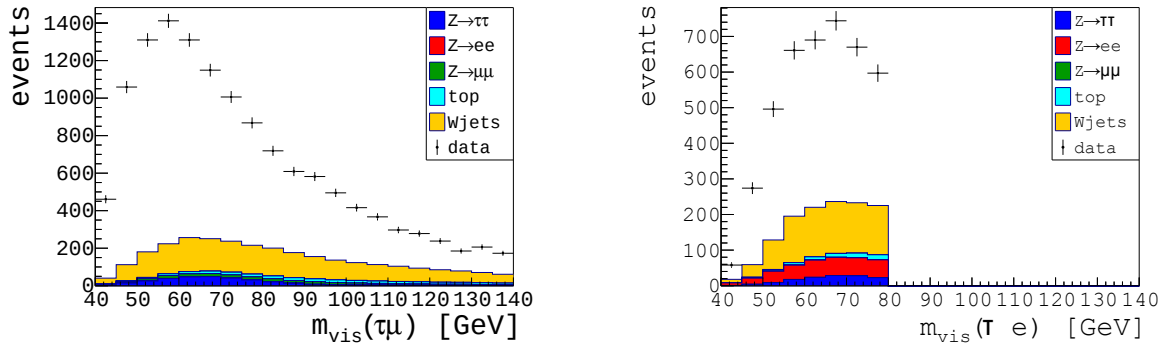

(a) Muon channel *(b)* Electron channel

Figure 8.13.: Visible mass in the isolation, !ID region. The dots correspond to data and the histograms represent the MC estimation simulated with POWHEG and PYTHIA. The multi-jet contribution dominates in this region. Therefore, the fake estimate is based on events from this region.

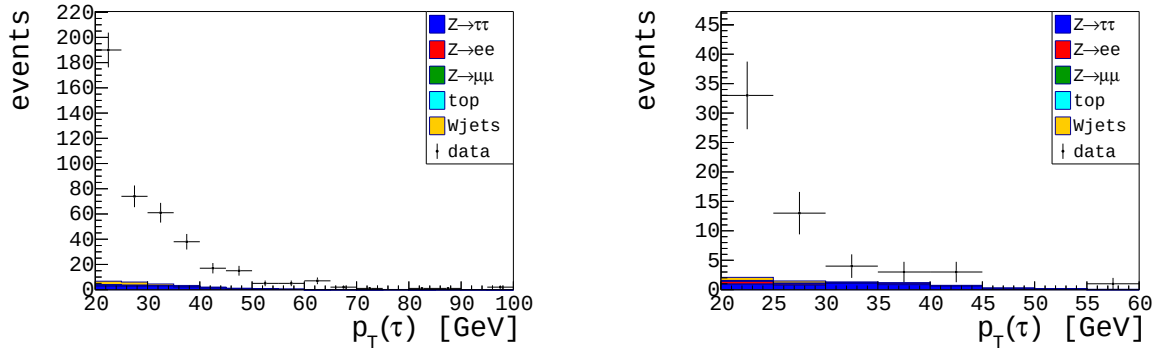

(a) Muon channel *(b)* Electron channel

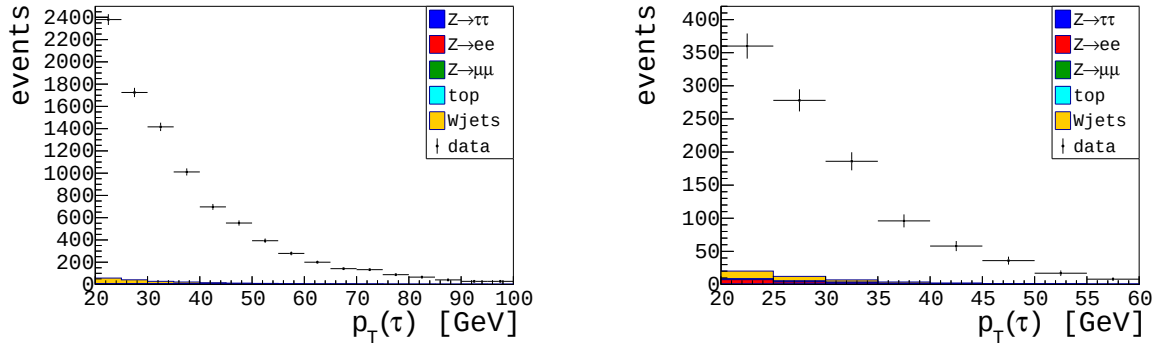

(c) Muon channel *(d)* Electron channel

Figure 8.14.: Inverted isolation region for ID and !ID selection. The dots correspond to data and the histograms represent the MC estimation simulated with POWHEG and PYTHIA. As intended the multi-jet contribution dominates.

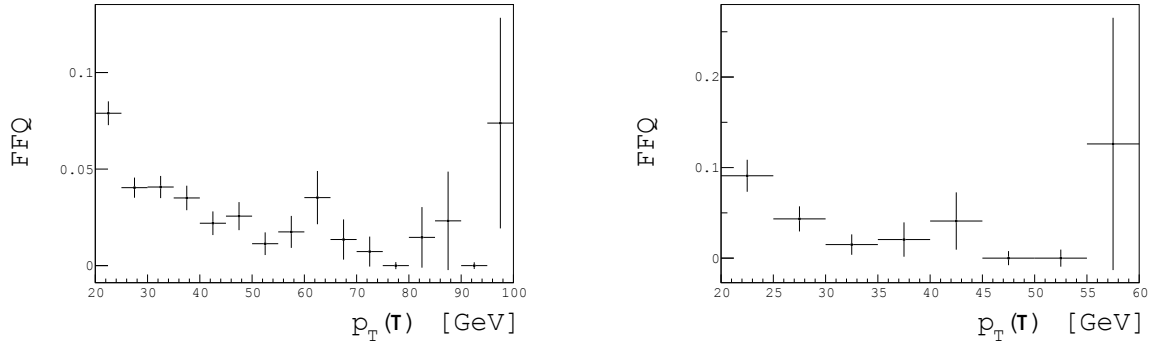

(a) Muon channel ***(b)*** Electron channel

Figure 8.15.: OS fake factors.

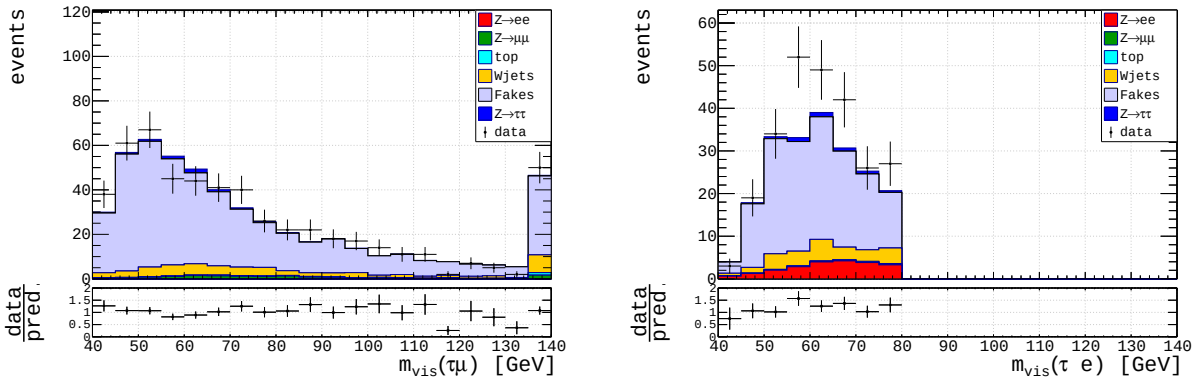

(a) Muon channel ***(b)*** Electron channel

Figure 8.16.: Visible mass distribution in the fake estimate validation region (SS). The first and the last bin contain the under- and overflow. The dots correspond to data and the histograms represent the prediction, of which the MC estimation is simulated with POWHEG and PYTHIA. The multi-jet contribution dominates in this region. The fake estimate is constructed using fake factors obtained from the SS, anti-isolated region. At this stage only the statistical uncertainties on the data are shown by error bars. Other variable distributions are shown in Figures A.5 to A.11.

8.8. Uncertainties

8.8.1. Systematic uncertainties

To evaluate the effect of the systematic uncertainties, the parameter which introduces the uncertainty is varied by $\pm 1\sigma$. The resulting change of the considered distribution determines the size of the uncertainty for this parameter. A list of all uncertainties is given in Table 8.4 and Table 8.5. Moreover, the relative change of the number of simulated events due to the systematic variation is presented since this is used in the cross section calculation in section 8.10.

Efficiencies: The uncertainties on the electron, muon and τ efficiencies are evaluated by varying the scale factors, which correct the efficiency of triggers, identification and isolation selection cuts and reconstruction in MC with respect to data, within the uncertainties provided by the respective performance groups.

τ energy scale (TES): The TES relates the measured energy to the real energy of the τ lepton and is measured by the Tau Working Group and its uncertainties are given in bins of p_T and η [30]. To apply the systematic variation the hadronic τ momentum is scaled upwards and downwards. Since this scale affects all τ momentum dependent variables, the TES is an important source of systematic uncertainty.

Muon and electron energy scale and resolution: Similar to the TES the energy scales of muons and electrons are important systematic uncertainties.
The energy resolution of muons and electrons in MC is smeared to match the resolution in data. From this smearing additional systematic uncertainties arise. In the case of muons, the smearing in the inner detector and the muon system is treated separately.

Jet energy scale (JES) and jet energy resolution (JER): Since MMC behaves differently for different number of jets (with $p_t > 30$ GeV), JES and JER uncertainties have to be considered. Furthermore, the jet calibration heavily affects MET hard term reconstruction. Jet calibration involves corrections of the jet direction and energy and accounts for pile-up. Additionally, a correction using in-situ calibration is applied to data. For this in-situ calibration momentum balance of jets against well measured objects like Z or γ bosons is used.
The analysis of uncertainties of the jet calibration is performed similar to the procedure in [23]. By diagonalising the covariance matrix of the 65 JES uncertainties the three main

sources of JES uncertainties are identified.
The jet energy resolution is measured using data at the Z peak and parametrised with a noise term N (electric and pile-up), a statistical term S and a p_T independent term C

$$\frac{\sigma(p_T)}{p_T} = \frac{N}{p_T} \oplus \frac{S}{\sqrt{p_T}} \oplus C \quad ,$$

where $\oplus$ is a short notation for square root of the quadratic sum. Again the most important source of JER uncertainty is identified by diagonalising the covariance matrix. By smearing the jet momentum, the JER uncertainty is applied.

MET soft term: The uncertainties due to energy scale and resolution of the MET soft term (see section 6.5) are important for MET reconstruction. While the uncertainties regarding the reconstructed objects which enter MET calculation are already accounted for, the soft term contribution is handled separately.

	Background				Signal			
	m_{vis}		m_{MMC1}		m_{vis}		m_{MMC1}	
Systematic	up [%]	down [%]	up [%]	down [%]	up [%]	down [%]	up [%]	down [%]
Muon scale & resolution	0.2	0.6	0.0	0.6	0.5	0.5	0.2	0.3
Muon identification & reconstruction	0.4	0.4	0.4	0.4	0.5	0.5	0.5	0.5
Isolation	0.3	0.3	0.3	0.3	0.4	0.4	0.4	0.4
Trigger	3.1	3.2	3.1	3.2	3.1	3.2	3.1	0.0
MET soft term	2.4	0.5	2.2	0.5	2.5	1.6	2.7	1.7
JES & JER	3.3	3.9	3.0	3.0	0.8	1.7	1.0	1.8
τ identification & reconstruction	0.5	0.5	0.5	0.5	10.4	10.4	10.5	10.5
TES	0.0	0.1	0.1	0.1	2.8	3.6	4.1	4.7
total	5.2	5.1	4.9	4.5	11.5	11.7	12.0	12.2

Table 8.4.: Upward and downward relative systematic uncertainties of the number of simulated signal and background events in the fiducial region of the muon channel for the two mass windows defined in section 8.10.

	Background				Signal			
	m_{vis}		m_{MMC1}		m_{vis}		m_{MMC1}	
Systematic	up [%]	down [%]	up [%]	down [%]	up [%]	down [%]	up [%]	down [%]
Electron identification & reconstruction	4.2	4.2	4.2	4.2	4.5	4.5	4.5	4.5
Electron scale & resolution	0.9	1.1	1.1	0.9	0.4	0.4	0.5	0.4
Isolation	0.5	0.5	0.5	0.5	0.5	0.5	0.5	0.5
Trigger	5.0	5.0	5.0	5.0	5.0	5.0	5.0	0.0
MET soft term	0.6	1.1	0.9	1.1	3.1	1.7	3.2	1.7
JES & JER	3.4	2.3	3.7	2.2	0.7	1.6	0.7	1.8
τ identification & reconstruction	0.4	0.4	0.4	0.4	10.5	10.5	10.4	10.4
TES	0.0	0.0	0.0	0.0	2.1	2.9	2.1	2.9
total	7.4	7.1	7.6	7.0	13.0	13.0	13.0	13.0

Table 8.5.: Upward and downward relative systematic uncertainties of the number of simulated signal and background events in the fiducial region of the electron channel for the two mass windows defined in section 8.10.

8.8.2. Other uncertainties

Luminosity uncertainty: The uncertainty of the luminosity (9 %) gives rise to an overall normalization uncertainty on backgrounds estimated by MC samples, which are not normalized against control regions in data. The luminosity uncertainty is calculated in a way similar to the procedure in [40].

Theoretical uncertainties: The MC is scaled according to the production cross section given in B.1. These cross sections suffer from uncertainties due to the QCD scale, the PDF set uncertainties and the uncertainties of the hadronisation and shower modelling. The uncertainties are found to be 6 % for the top samples and 5 % for the other samples [41].

Fake estimate: The statistical uncertainties that propagate into the multi-jet estimate are included in the error bands as well. In order to account for the non-closure[1] in the SS region, an additional systematic error of the multi-jet estimate is estimated in the SS region. In the case of closure, the quantity

$$\frac{\chi^2}{N_{bins}} = \frac{1}{N_{bins}} \sum_{i=1}^{N_{bins}} \frac{(N_{D,i} - N_{MC,i} - N_{F,i})^2}{\sigma_{D,i}^2 + \sigma_{MC,i}^2 + \sigma_{F,i}^2}$$

[1]Observation and prediction not compatible within the uncertainties

with the number of data $N_{D,i}$, MC $N_{MC,i}$, fake events $N_{F,i}$ and the statistical errors of data $\sigma_{D,i}$, MC $\sigma_{MC,i}$ and fake estimate $\sigma_{F,i}$ in the i-th bin is expected to be one or smaller. A simple approach to estimate the error in the non-closure case, is the addition of a relative error σ_{rel} to every bin such that the quantity

$$\frac{\chi^2}{N_{bins}} = \frac{1}{N_{bins}} \sum_{i=1}^{N_{bins}} \frac{(N_{D,i} - N_{MC,i} - N_{F,i})^2}{\sigma_{D,i}^2 + \sigma_{MC,i}^2 + \sigma_{F,i}^2 + \sigma_{rel}^2 N_{F,i}^2} \tag{8.1}$$

is equal to one. A disadvantage of this method is the dependence on the binning of the histogram. To account for this issue, the error estimation is performed for exactly the binning which is used for the plots. However, bins which neither contain data events nor predicted (MC and fake) events are neglected since they would artificially increase N_{bins}. Furthermore, σ_{rel} and σ_F might be correlated if the non-closure is caused by statistical fluctuations. In this simple approach the correlation cannot be determined since the constraint $1 = \frac{\chi^2}{N_{bins}}$ is used to determine σ_{rel}. The results of this method are given in Table 8.6.

Muon channel

Variable	Number of bins	Range	σ_{rel}
$p_T(\mu)$	15	[25 GeV , 100 GeV]	0.323
$p_T(\tau)$	16	[20 GeV , 100 GeV]	0.000
m_{vis}	20	[40 GeV , 140 GeV]	0.160
MET	30	[0 GeV , 150 GeV]	0.020
$\sum_{i=\tau,\mu} \cos\Delta\phi(i, \vec{p}_T^{\,miss})$	40	[-0.2, 2]	0.103
$\Delta\phi(\mu, \tau)$	40	[1.5, 3.2]	0.139
m_T	10	[0 GeV , 50 GeV]	0.000
m_{MMC1}	20	[40 GeV , 140 GeV]	0.000
m_{MMC1}	1	[60 GeV , 140 GeV]	0.000
m_{vis}	1	[40 GeV , 80 GeV]	0.000

Electron channel

Variable	Number of bins	Range	σ_{rel}
$p_T(e)$	15	[25 GeV , 100 GeV]	0.324
$p_T(\tau)$	16	[20 GeV , 100 GeV]	0.000
m_{vis}	20	[40 GeV , 140 GeV]	0.167
MET	30	[0 GeV , 150 GeV]	0.397
$\sum_{i=\tau,e} \cos\Delta\phi(i, \vec{p}_T^{\,miss})$	40	[-0.2, 2]	0.588
$\Delta\phi(e, \tau)$	40	[1.5, 3.2]	0.000
m_T	10	[0 GeV , 50 GeV]	0.369
m_{MMC1}	20	[40 GeV , 140 GeV]	0.000
m_{MMC1}	1	[60 GeV , 140 GeV]	0.260
m_{vis}	1	[40 GeV , 80 GeV]	0.257

Table 8.6.: Additional relative uncertainty σ_{rel} of the fake estimate to account for the non-closure. σ_{rel} is given for all binnings used in the plots in section 8.9 and the calculations in section 8.10. The final uncertainty is then the combination of statistical uncertainty and this additional uncertainty σ_{rel}.

8.9. Variable distributions

Figures 8.17 to 8.24 show distributions of important variables in the signal region with all errors described in section 8.8.1 included in the error band.

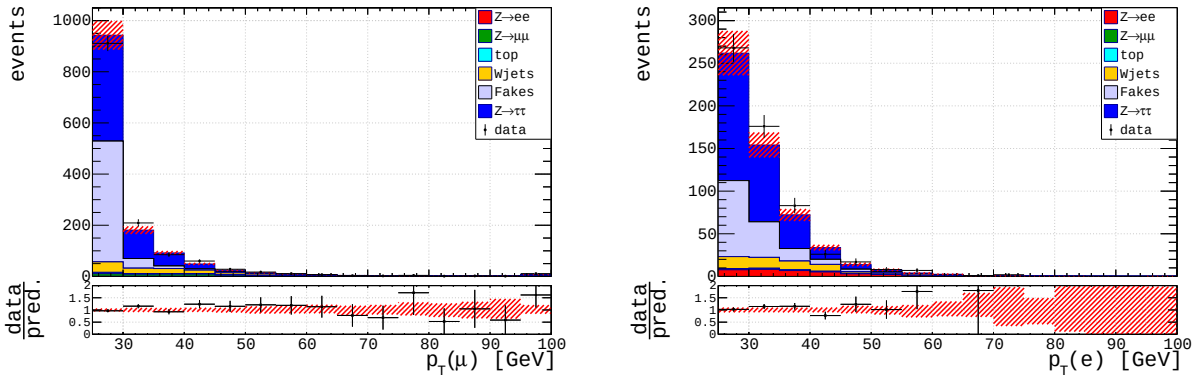

(a) Muon channel *(b)* Electron channel

Figure 8.17.: Lepton p_T distribution in the signal region. The first and the last bin contain the under- and overflow. The dots correspond to data, the histograms represent the prediction, of which the MC estimation is simulated with PowHeg and Pythia. The fake estimate is constructed using OS fake factors. While the statistical uncertainty on the data is indicated by error bars, the systematic, statistical and luminosity related uncertainties of the prediction are added in quadrature and visualized by the hatched error band.

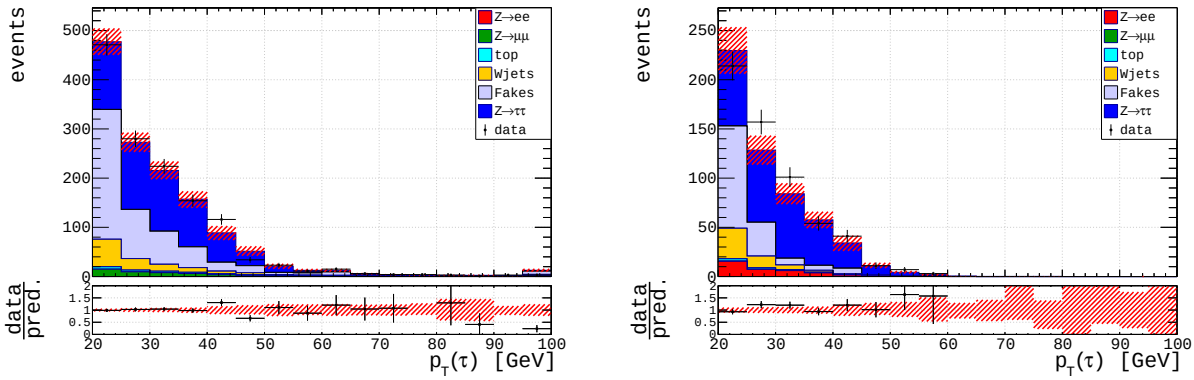

(a) Muon channel *(b)* Electron channel

Figure 8.18.: τ p_T distribution in the signal region. The details are the same as in Figure 8.17.

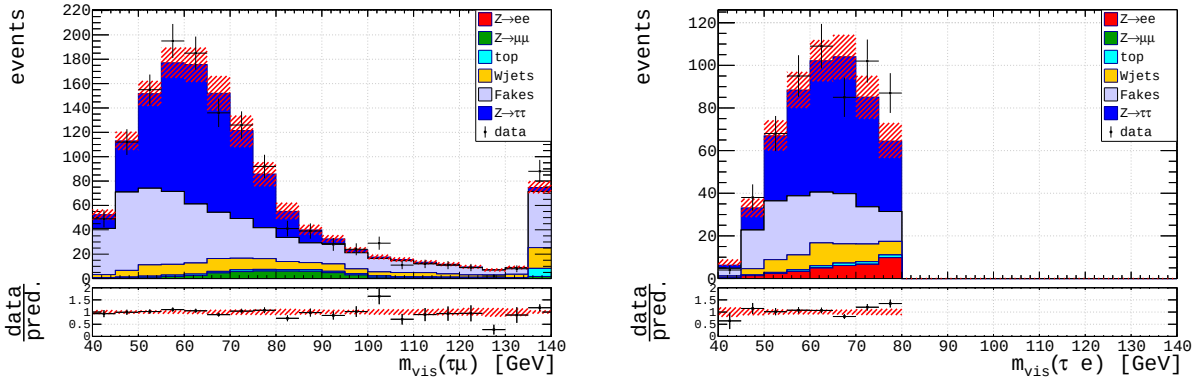

(a) Muon channel *(b)* Electron channel

Figure 8.19.: Visible mass distribution in the signal region. The first and the last bin contain the under- and overflow. The details are the same as in Figure 8.17.

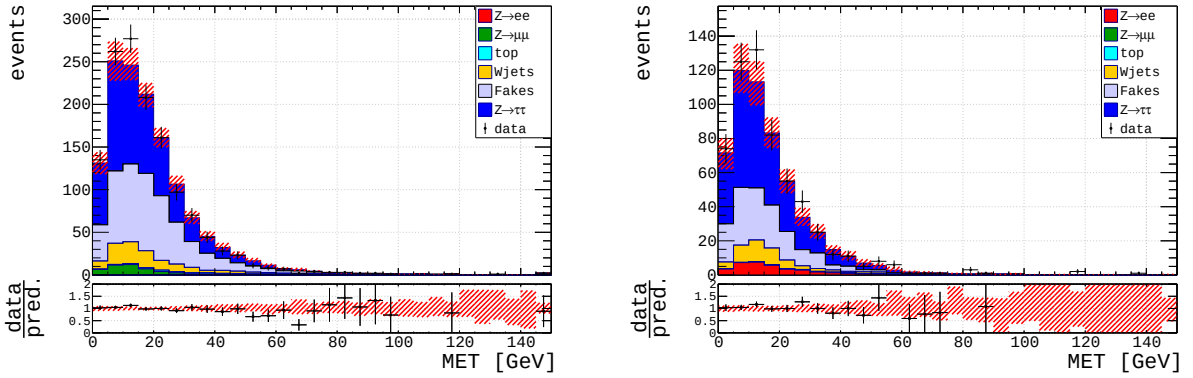

(a) Muon channel *(b)* Electron channel

Figure 8.20.: MET distribution in the signal region. The details are the same as in Figure 8.17.

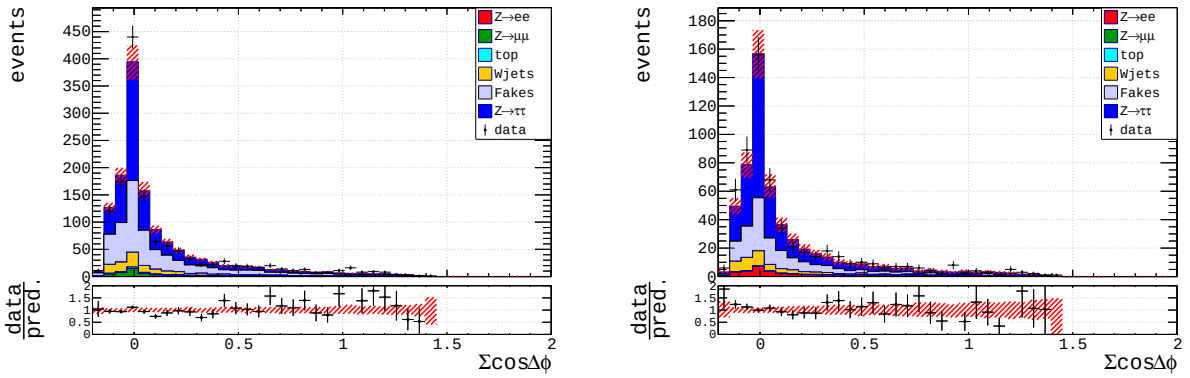

(a) Muon channel *(b)* Electron channel

Figure 8.21.: $\sum_{i=\tau,\ell} \cos\Delta\phi(i, \not{p}_T)$ distribution in the OS control region. The details are the same as in Figure 8.17.

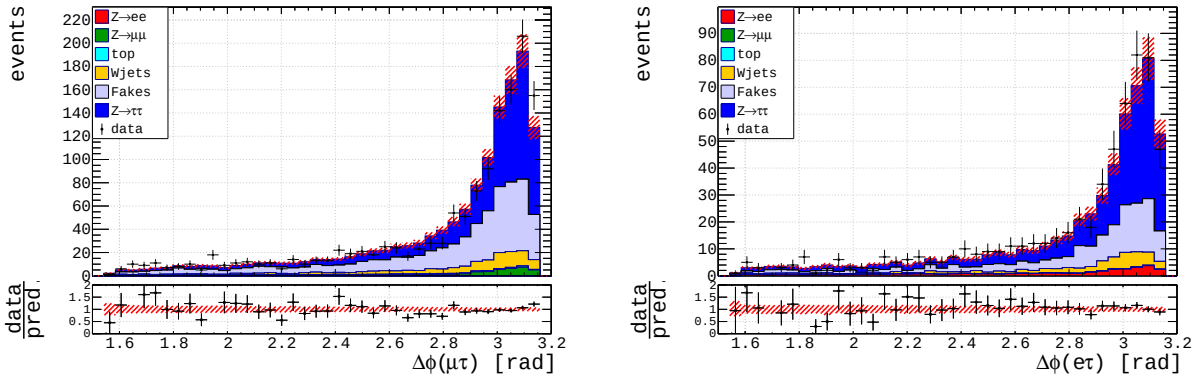

(a) Muon channel *(b)* Electron channel

Figure 8.22.: $\Delta\phi(\ell, \tau)$ distribution in the signal region. The details are the same as in Figure 8.17.

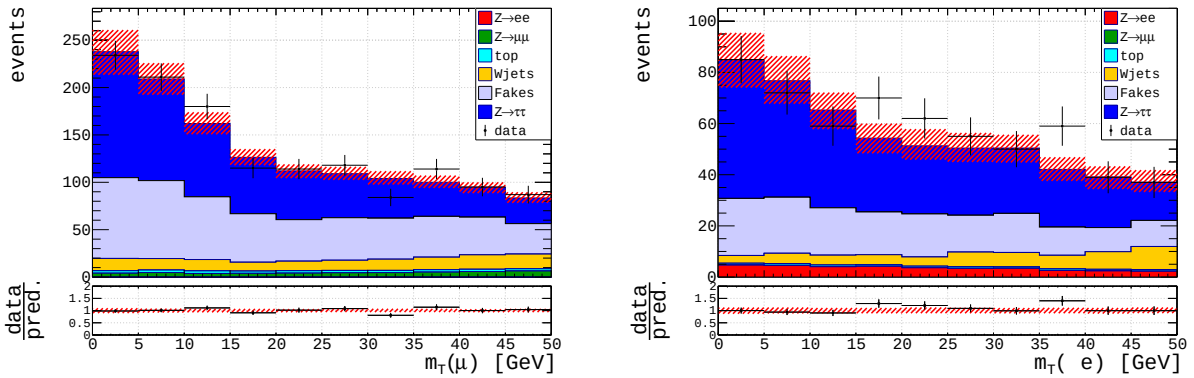

(a) Muon channel *(b)* Electron channel

Figure 8.23.: Transverse mass distribution in the signal region. The details are the same as in Figure 8.17.

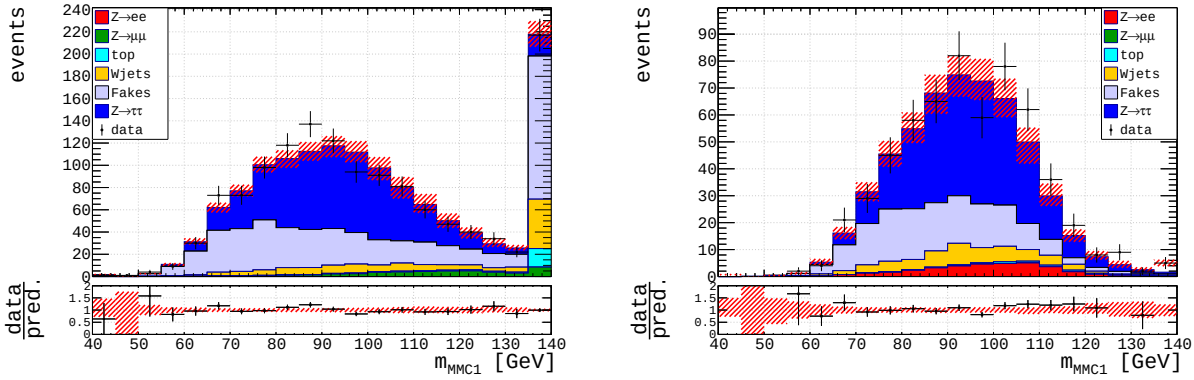

(a) Muon channel ***(b)*** Electron channel

Figure 8.24.: MMC mass distribution in the signal region. The first and the last bin contain the under- and overflow. While the distribution in the muon channel shows a large overflow bin, the distribution in the electron does not since the visible mass cut suppresses higher MMC masses as well. The other details are the same as in Figure 8.17.

8.10. Fiducial cross section

A fiducial cross section σ_{fid} is obtained if only events from the signal (fiducial) region are taken into account. The number of expected background events N_{bkg} in the signal region is subtracted from the number N_{obs} of data events. The cross section is then the ratio of this difference and the integrated luminosity

$$\sigma_{fid} = \frac{N_{obs} - N_{bkg}}{\mathcal{L}_{int} C} \quad . \tag{8.2}$$

In order to account for detector effects and infer a cross section on truth (particle) level, a correction factor C is needed. It is defined as the ratio of truth N^{sig}_{truth} and reconstructed N^{sig}_{reco} signal events passing the signal region cuts

$$C = \frac{N^{sig}_{reco}}{N^{sig}_{truth}} \quad .$$

For this analysis the fiducial region is defined as follows:

- $Z \to \tau_{lep}\tau_{had}$ topology, includes di-lepton Veto, OS criterion and object definition cuts (p_T and η)
- $\sum_{i=\tau,\ell} \cos\Delta\phi(i, \not{p}_T) > -0.15$
- $m_T < 50$ GeV
- $\Delta\phi(\ell, \tau) > 1.57$

Additionally, the reconstructed invariant Z mass is constrained to a window around the true Z mass. One calculation is performed using the MMC1 mass within the window [60 GeV , 140 GeV]. The interval is chosen, such that the truth MMC1 mass distribution is contained in it. An alternative cross section using a visible mass window [40, GeV , 80 GeV] is calculated as a cross check.
The determination of the correction factor C needs a selection based on truth events. On truth level the signal region cuts have to be applied. Nevertheless, online and offline identification requirements are not necessary (and not available) since the particles are truth particles. Because the truth τ leptons are assigned a (full) truth four-momentum p^{μ}_{τ}, the truth visible momenta are constructed by subtracting the neutrino component $p^{\mu}_{\nu_i}$ of neutrino i

$$p^{\mu}_{vis} = p^{\mu}_{\tau} - \sum_{i} p^{\mu}_{\nu_i} \quad .$$

The results of the calculations using the MMC mass window in the muon channel are given in Table 8.7.

$$\begin{aligned}
N_{obs} &= 1140 \pm 40 \text{ (stat.)} \\
N_{bkg} &= 533 \pm 24 \text{ (stat.)} \, ^{+10}_{-9} \text{ (sys.)} \, \pm 50 \text{ (lumi.)} \\
N_{obs} - N_{bkg} &= 607 \pm 50 \text{ (stat.)} \, ^{+10}_{-9} \text{ (sys.)} \, \pm 50 \text{ (lumi.)} \\
N^{sig}_{reco} &= 594 \pm 4 \text{ (stat.)} \, ^{+80}_{-80} \text{ (sys.)} \, \pm 60 \text{ (lumi.)} \\
N^{sig}_{truth} &= 2324 \pm 5 \text{ (stat.)} \, \pm 120 \text{ (sys.)} \, \pm 210 \text{ (lumi.)} \\
C &= 0.2556 \pm 0.0019 \text{ (stat.)} \, ^{+0.04}_{-0.04} \text{ (sys.)} \\
\sigma_{fid} &= 28.1 \pm 2.4 \text{ (stat.)} \, ^{+5}_{-5} \text{ (sys.)} \, \pm 4 \text{ (lumi.)} \text{ pb}
\end{aligned}$$

Table 8.7.: Fiducial cross section results in the muon channel for the MMC mass window.

The statistical error of the fake estimate is independent from the one on the data in the signal region since an orthogonal region is used to construct the fake estimate. Consequently, the errors can be summed in quadrature. This leads to a substantial rise of the relative statistic error of the difference $N_{obs} - N_{bkg}$ because the errors are summed, but the values are subtracted. When the ratio of $N_{obs} - N_{bkg}$ over the luminosity $\mathcal{L}_{int}$ is calculated, the MC component of the background is luminosity-independent because it was scaled according to the luminosity. This has to be taken into account. Similarly the luminosity error does not affect C. In the ratio C the cross section the MC is scaled to is canceled. Therefore, C is not affected by the cross section uncertainty.
The sources of systematic uncertainty of the simulated background and signal events are listed in the Tables 8.4 and 8.5 and affect the systematic uncertainties of $N_{obs} - N_{bkg}$ and C. The uncertainties related to τ lepton identification and reconstruction dominate for the signal sample, while trigger, electron identification and jet uncertainties constitute the largest uncertainty for the background samples. Since the τ lepton identification uncertainty is by far dominant for the signal sample and has almost no impact on the background samples, the correlation of the systematics of C and $N_{obs} - N_{bkg}$ are neglected. According to the error propagation formula for the error σ_f of a variable $f(x, y)$

with correlated variables x and y and uncertainties σ_x and σ_x[42]

$$\sigma_f^2 = (\sigma_x \partial_x f)^2 + (\sigma_y \partial_y f)^2 + 2\rho\sigma_x \partial_x f \sigma_y \partial_y f \quad , \tag{8.3}$$

neglecting the correlation ρ will increase the systematic uncertainty on the cross section. The acceptance $A = {}^{N^{sig}_{truth}}/_{N^{tot}_{truth}}$, which is the fraction of truth events passing the selection cuts, relates the fiducial cross section to the total one σ_{tot} as follows

$$\sigma_{tot} = \frac{\sigma_{fid}}{A} \quad .$$

Since the number of events passing the selection cuts N^{sig}_{truth} is a subset of the total number of truth events, a binomial error σ_A is assigned to A

$$\sigma_A = \sqrt{\frac{A(1-A)}{N^{tot}_{truth}}} \quad .$$

N^{sig}_{truth} drops out in the product CA such that CA inherits errors only from N^{sig}_{reco} because N^{tot}_{truth} as the number of generated events is known without any error. Hence, one yields for the acceptance and the total cross section the results given in Table 8.8

$$\begin{aligned} A &= 0.01407 \pm 0.00029 \text{ (stat.)} \\ \sigma_{tot} &= 1990 \pm 170 \text{ (stat.)} \, {}^{+280}_{-280} \text{ (sys.)} \, \pm 220 \text{ (lumi.) pb} \quad . \end{aligned}$$

Table 8.8.: Total cross section results in the muon channel for the MMC mass window.

Table 8.9 presents the results for the visible mass window in the muon channel.

$$
\begin{aligned}
N_{obs} &= 1040 \pm 40 \text{ (stat.)} \\
N_{bkg} &= 456 \pm 22 \text{ (stat.)} \, ^{+7}_{-7} \text{ (sys.)} \pm 50 \text{ (lumi.)} \\
N_{obs} - N_{bkg} &= 584 \pm 50 \text{ (stat.)} \, ^{+7}_{-7} \text{ (sys.)} \pm 50 \text{ (lumi.)} \\
N^{sig}_{reco} &= 564 \pm 4 \text{ (stat.)} \, ^{+80}_{-80} \text{ (sys.)} \pm 60 \text{ (lumi.)} \\
N^{sig}_{truth} &= 2195 \pm 5 \text{ (stat.)} \pm 110 \text{ (lumi.)} \pm 210 \text{ (lumi.)} \\
C &= 0.2569 \pm 0.0020 \text{ (stat.)} \, ^{+0.04}_{-0.04} \text{ (sys.)} \\
\sigma_{fid} &= 26.9 \pm 2.4 \text{ (stat.)} \, ^{+5}_{-5} \text{ (sys.)} \pm 2.9 \text{ (lumi.) pb} \\
A &= 0.01329 \pm 0.00029 \text{ (stat.)} \\
\sigma_{tot} &= 2020 \pm 170 \text{ (stat.)} \, ^{+240}_{-240} \text{ (sys.)} \pm 210 \text{ (lumi.) pb}
\end{aligned}
$$

Table 8.9.: Cross section results in the muon channel for the visible mass window.

The visible mass cut introduced to suppress the $Z \to ee$ contribution hinders the comparison of electron and muon channel in the case of the MMC1 mass window. Therefore, one extrapolates back to the full visible mass space using the correction factor C. The results are given in Table 8.10.

$$
\begin{aligned}
N_{obs} &= 582 \pm 25 \text{ (stat.)} \\
N_{bkg} &= 245 \pm 26 \text{ (stat.)} \, ^{+60}_{-60} \text{ (sys.)} \pm 23 \text{ (lumi.)} \\
N_{obs} - N_{bkg} &= 337 \pm 40 \text{ (stat.)} \, ^{+60}_{-60} \text{ (sys.)} \pm 23 \text{ (lumi.)} \\
N^{sig}_{reco} &= 301.4 \pm 2.5 \text{ (stat.)} \, ^{+50}_{-50} \text{ (sys.)} \pm 28 \text{ (lumi.)} \\
N^{sig}_{truth} &= 1421 \pm 4 \text{ (stat.)} \pm 80 \text{ (sys.)} \pm 130 \text{ (lumi.)} \\
C &= 0.2121 \pm 0.0019 \text{ (stat.)} \, ^{+0.03}_{-0.03} \text{ (sys.)} \\
\sigma_{fid} &= 18.8 \pm 2.3 \text{ (stat.)} \, ^{+5}_{-5} \text{ (sys.)} \pm 2.2 \text{ (lumi.) pb} \\
A &= 0.00861 \pm 0.00023 \text{ (stat.)} \\
\sigma_{tot} &= 2180 \pm 260 \text{ (stat.)} \, ^{+500}_{-500} \text{ (sys.)} \pm 250 \text{ (lumi.) pb}
\end{aligned}
$$

Table 8.10.: Cross section results in the electron channel for the MMC mass window.

This extrapolation is not necessary for the visible mass window. The results can be found

in Table 8.11.

$$
\begin{aligned}
N_{obs} &= 588 \pm 25 \text{ (stat.)} \\
N_{bkg} &= 248 \pm 26 \text{ (stat.)} \, ^{+60}_{-60} \text{ (sys.)} \, \pm 23 \text{ (lumi.)} \\
N_{obs} - N_{bkg} &= 340 \pm 40 \text{ (stat.)} \, ^{+60}_{-60} \text{ (sys.)} \, \pm 23 \text{ (lumi.)} \\
N^{sig}_{reco} &= 302.5 \pm 2.5 \text{ (stat.)} \, ^{+50}_{-50} \text{ (sys.)} \, \pm 28 \text{ (lumi.)} \\
N^{sig}_{truth} &= 1310 \pm 4 \text{ (stat.)} \, \pm 70 \text{ (sys.)} \, \pm 120 \text{ (lumi.)} \\
C &= 0.2309 \pm 0.0021 \text{ (stat.)} \, ^{+0.04}_{-0.04} \text{ (sys.)} \\
\sigma_{fid} &= 17.4 \pm 2.1 \text{ (stat.)} \, ^{+5}_{-5} \text{ (sys.)} \, \pm 2.0 \text{ (lumi.)} \text{ pb} \\
A &= 0.01329 \pm 0.00029 \text{ (stat.)} \\
\sigma_{tot} &= 2190 \pm 260 \text{ (stat.)} \, ^{+500}_{-500} \text{ (sys.)} \, \pm 260 \text{ (lumi.)} \text{ pb}
\end{aligned}
$$

Table 8.11.: Cross section results in the electron channel for the visible mass window.

The theoretical prediction 1930 ± 97 pb [41] is consistent with the measurements. Nevertheless, the systematic uncertainties in the electron channel are due to the additional uncertainty on the fake estimate relatively large.

8.10.1. Compatibility test of cross sections with different mass windows

If the resulting cross sections in the different mass windows are tested for compatibility, then the strong correlation of the two masses and accordingly the correlation of the cross sections has to be taken into account. The error propagation formula (8.3) yields the error $\sigma_{\Delta\sigma}$ for the difference $\Delta\sigma = \sigma_{m_{vis}} - \sigma_{m_{MMC}}$

$$\sigma^2_{\Delta\sigma} = (\sigma_{m_{vis}})^2 + (\sigma_{m_{MMC}})^2 - 2\rho\sigma_{m_{vis}}\sigma_{m_{MMC}} \quad .$$

The correlation can be easily determined in 2d plots for the masses itself, but for the cross sections this is more difficult. The cross section calculation is repeated for ten subsets of the data (see Figure 8.25 for the results). The correlation factor can now be determined using the expression for the correlation factor of two variables x and y

$$\rho = \frac{1}{N\sigma_x\sigma_y} \sum_i (x - \overline{x})(y - \overline{y}) \quad ,$$

where N is the number of points, $\overline{x}$ is the mean value of x and σ_x its standard deviation. With a correlation factor of 0.7670 in the muon channel and 0.9978 in the electron channel the compatibility test of the cross sections using a MMC mass window (Tables 8.10 and 8.8) and a visible mass window (Tables 8.11 and 8.9) yields

$$\text{Muon channel: } |\sigma_{m_{vis}} - \sigma_{m_{MMC1}}| = 30 \pm 120 \text{ (stat.)} \, ^{+190}_{-190} \text{ (sys.)} \pm 150 \text{ (lumi.) pb}$$
$$\text{Electron channel: } |\sigma_{m_{vis}} - \sigma_{m_{MMC1}}| = 10 \pm 18 \text{ (stat.)} \, ^{+40}_{-40} \text{ (sys.)} \pm 20 \text{ (lumi.) pb}$$

.

Hence, the two approaches are compatible for both channels.

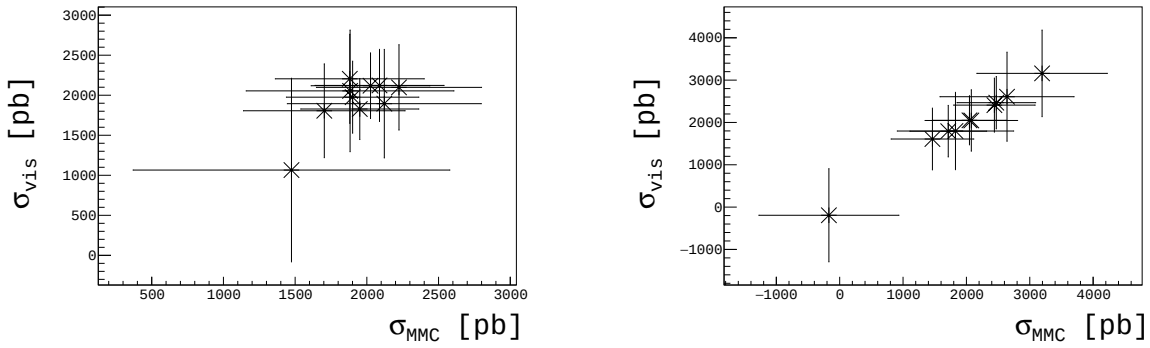

(a) Muon channel ***(b)*** Electron channel

Figure 8.25.: Correlation of the cross sections with MMC and visible mass window.

9. Conclusion

In this thesis two studies preparing Run II $H \to \tau\tau$ analyses were presented. Firstly, one key component of the di-τ mass reconstruction algorithm MMC, the angular distributions, were reparametrised using a more advanced approach than in Run I. Secondly, the cross section of the irreducible background $Z \to \tau\tau$ was measured in the semi-leptonic channel. The results are summarised in the following sections.

9.1. MMC parametrisation

The angular distributions needed for the MMC were parametrised for the truth decay modes 1p0n, 1p1n, 1p2n, 3p0n and 3p1n separately. Unfortunately, the desired improvement of the MMC mass distribution was not observed. The effects of the MET resolution and decay mode misclassification were studied but no link between them and the absence of an improvement in MMC resolution could be established. Tests with a random parametrisation revealed a small impact of the parametrisation on the mass resolution. Hence, differences between the decay modes are probably not large enough to significantly improve the mass resolution.
One advantage of the new parametrisation is the more accurate peak position, while the mass reconstruction efficiency remains the same.

9.2. Cross section measurement

The first data of LHC Run II with 50 ns bunch spacing, corresponding to an integrated luminosity of $\mathcal{L}_{int} = 85$ pb^{-1}, was analysed with the aim to measure the cross section of the $Z \to \tau\tau$ process in the semi-leptonic channel. For this purpose, a signal region was defined and a multi-jet fake estimate was constructed using a data-driven fake factor method. This method needs to be revisited because closure tests in a validation region exhibit a disagreement for the electron channel. This non-closure was treated as an additional error of the fake estimate.
In the signal region a fiducial cross section was measured and a total cross section was de-

rived. Using the MMC a mass window of [60 GeV , 140 GeV] for these cross section measurements was defined. The final cross section results are $\sigma_{tot} = 2180 \pm 260$ (stat.) $^{+500}_{-500}$ (sys.) ± 250 (lumi.) pb in the electron channel and $\sigma_{tot} = 1990 \pm 170$ (stat.) $^{+280}_{-280}$ (sys.) ± 220 (lumi.) pb in the muon channel. The theoretical prediction of 1930 ± 97 pb is found to be consistent with both measurements.
While the $Z \to \tau\tau$ cross section was measured at a center-of-mass energy of $\sqrt{s} = 7, 8$ TeV [43, 44], up to now only the cross sections of $Z \to \mu\mu$ and $Z \to ee$ were measured at $\sqrt{s} = 13$ TeV [41]. The presented cross section measurement is therefore the first measurement of the $Z \to \tau\tau$ cross section at $\sqrt{s} = 13$ TeV .
In order to refine the analysis and thus improve the cross section measurement, the uncertainties have to be reduced. The statistical error will become smaller as more data is added. Also the uncertainty on the luminosity is expected to become smaller. Further studies are required to reduce the systematic uncertainties, of which the τ lepton identification is the largest (up to 10 %).
Furthermore, electrons faking τ leptons have to be further investigated since this thesis revealed a large contribution of $Z \to ee$ to a $\tau_{lep}\tau_{had}$ selection, even after applying the full set of recommendations provided by the Tau Working Group for early Run II analyses.

A. Figures

A.1. Additional momentum dependence plots

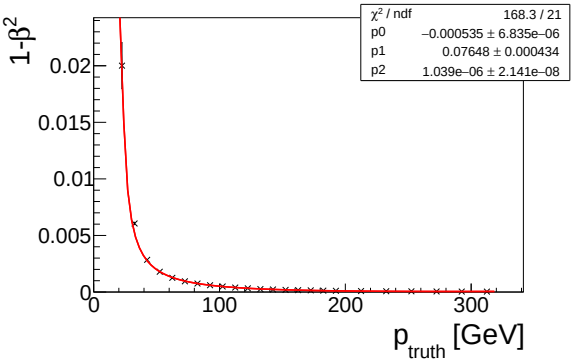

(a) $1-\beta^2$, fit function $p_0 + \frac{p_1}{x-19\ \mathrm{GeV}} + p_2 x$

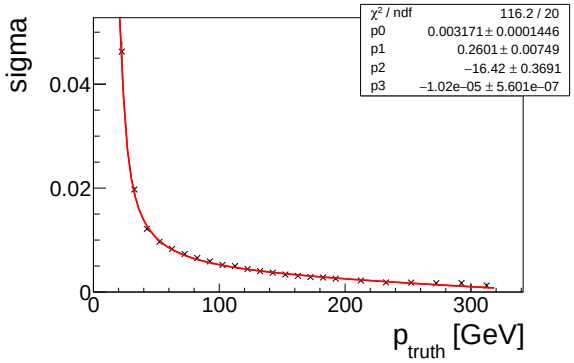

(b) Sigma, fit function $p_0 + \frac{p_1}{x+p_2} + p_3 x$

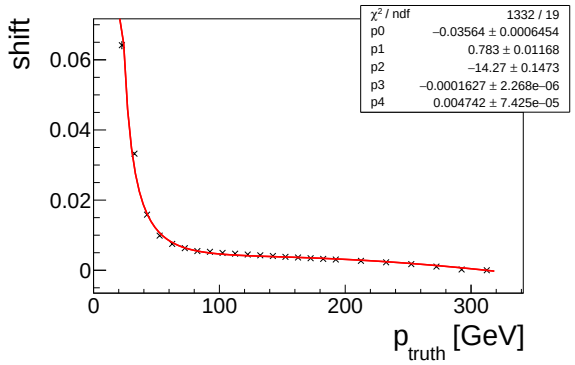

(c) Shift, fit function $p_0 + \frac{p_1}{x+p_2} + p_3 x + p_4\sqrt{x}$

Figure A.1.: Momentum dependence of the fit parameters for the α distributions (1p1n). The underlying $Z \to \tau\tau$ sample is generated with PowHeg and Pythia at $\sqrt{s} = 13$ TeV with 50 ns bunch spacing.

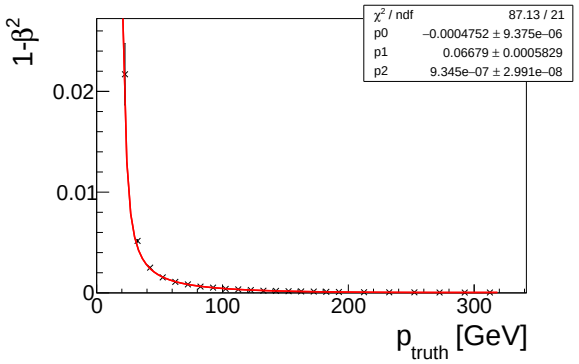

(a) $1-\beta^2$, fit function $p_0 + \frac{p_1}{x-19\ \mathrm{GeV}} + p_2 x$

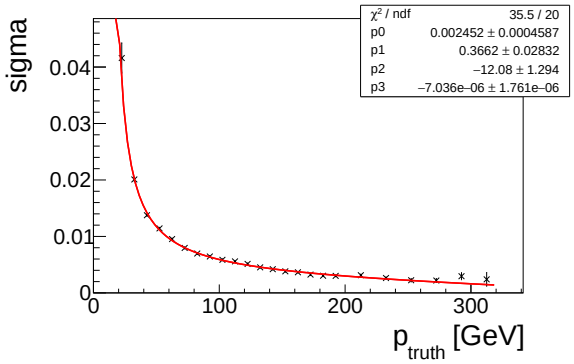

(b) Sigma, fit function $p_0 + \frac{p_1}{x+p_2} + p_3 x$

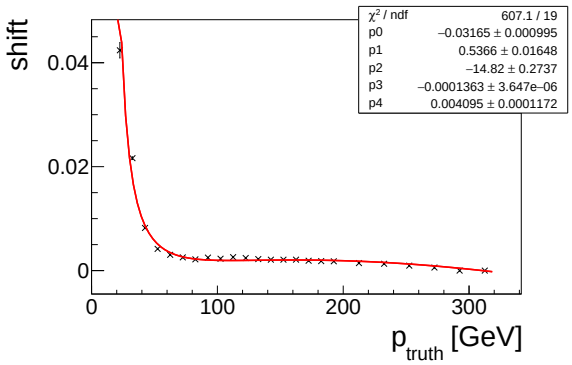

(c) Shift, fit function $p_0 + \frac{p_1}{x+p_2} + p_3 x + p_4\sqrt{x}$

Figure A.2.: Momentum dependence of the fit parameters for the α distributions (1p2n). The underlying $Z \to \tau\tau$ sample is generated with POWHEG and PYTHIA at $\sqrt{s} = 13$ TeV with 50 ns bunch spacing.

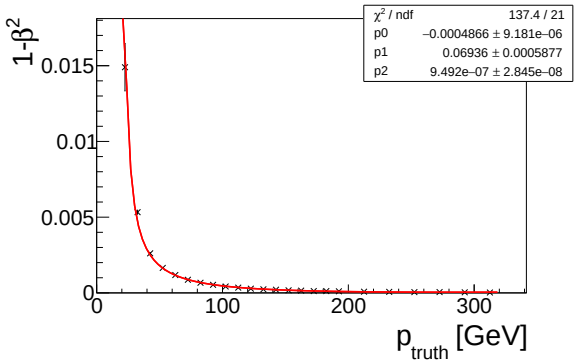

(a) $1-\beta^2$, fit function $p_0 + \frac{p_1}{x-19\ \mathrm{GeV}} + p_2 x$

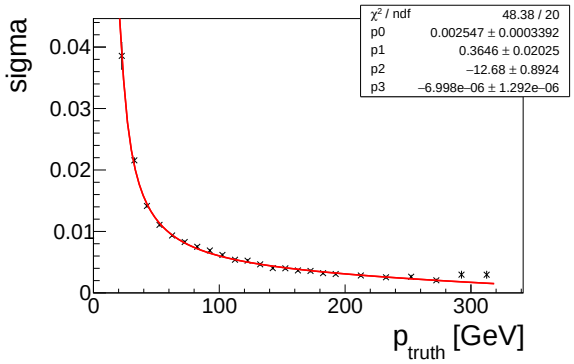

(b) Sigma, fit function $p_0 + \frac{p_1}{x+p_2} + p_3 x$

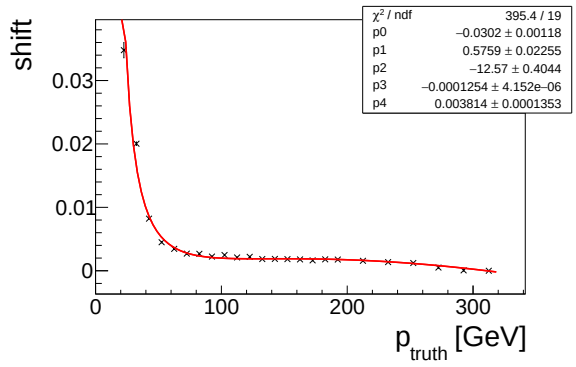

(c) Shift, fit function $p_0 + \frac{p_1}{x+p_2} + p_3 x + p_4\sqrt{x}$

Figure A.3.: Momentum dependence of the fit parameters for the α distributions (3p0n). The underlying $Z \to \tau\tau$ sample is generated with POWHEG and PYTHIA at $\sqrt{s} = 13$ TeV with 50 ns bunch spacing.

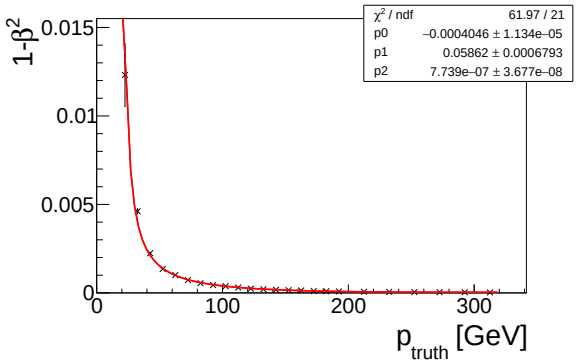

(a) $1-\beta^2$, fit function $p_0 + \frac{p_1}{x-19\ \mathrm{GeV}} + p_2 x$

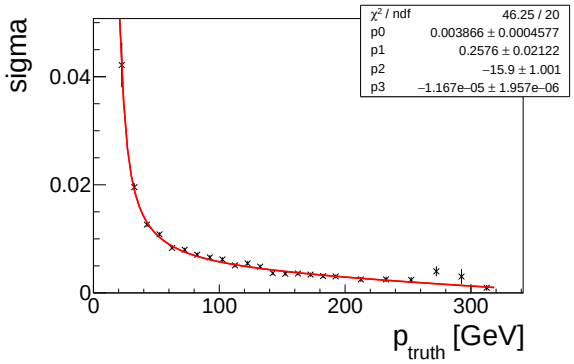

(b) Sigma, fit function $p_0 + \frac{p_1}{x+p_2} + p_3 x$

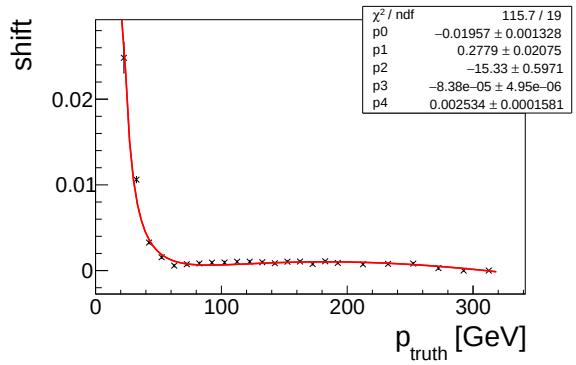

(c) Shift, fit function $p_0 + \frac{p_1}{x+p_2} + p_3 x + p_4\sqrt{x}$

Figure A.4.: Momentum dependence of the fit parameters for the α distributions (3p1n). The underlying $Z \to \tau\tau$ sample is generated with POWHEG and PYTHIA at $\sqrt{s} = 13$ TeV with 50 ns bunch spacing.

A.2. Additional variable distributions in the fake estimate validation region

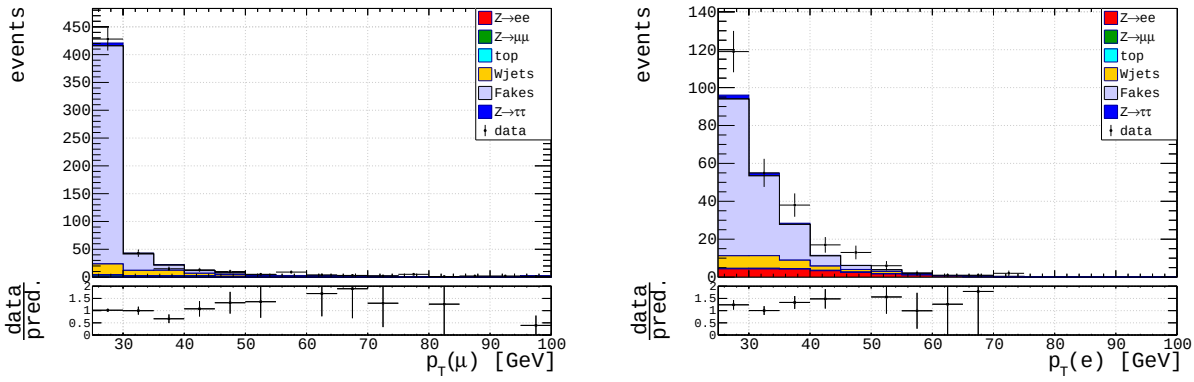

(a) Muon channel *(b)* Electron channel

Figure A.5.: Lepton p_T distribution in the fake estimate validation region (SS). The details are the same as in Figure 8.16.

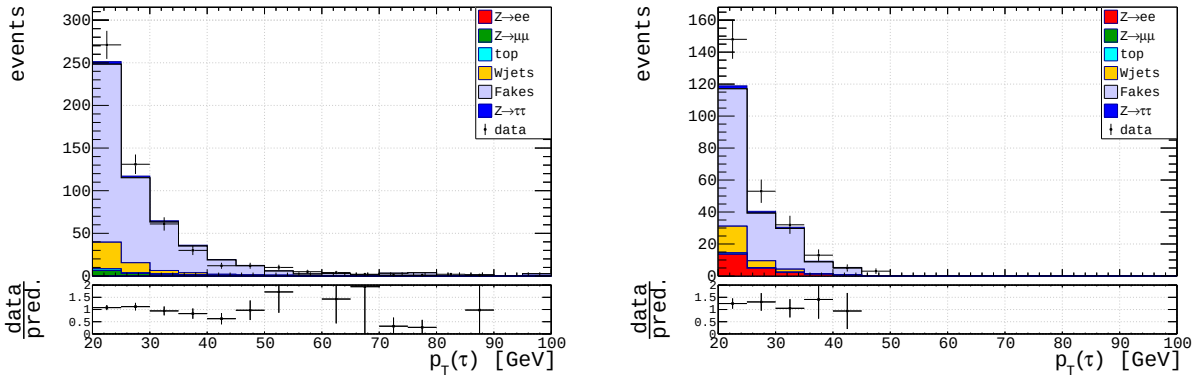

(a) Muon channel *(b)* Electron channel

Figure A.6.: τ p_T distribution in the fake estimate validation region (SS). The details are the same as in Figure 8.16.

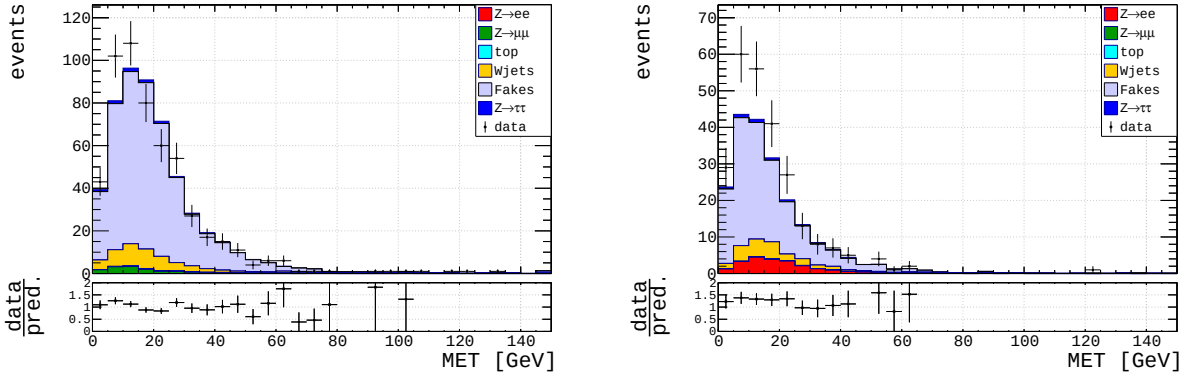

(a) Muon channel *(b)* Electron channel

Figure A.7.: MET distribution in the fake estimate validation region (SS). The details are the same as in Figure 8.16.

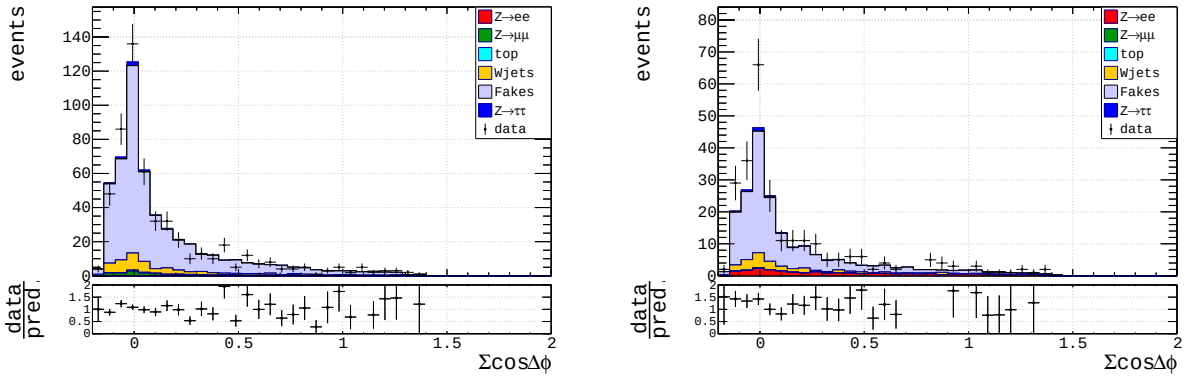

(a) Muon channel *(b)* Electron channel

Figure A.8.: $\sum_{i=\tau,\ell} \cos\Delta\phi(i, \vec{p}_T^{\,miss})$ distribution in the fake estimate validation region (SS). The details are the same as in Figure 8.16.

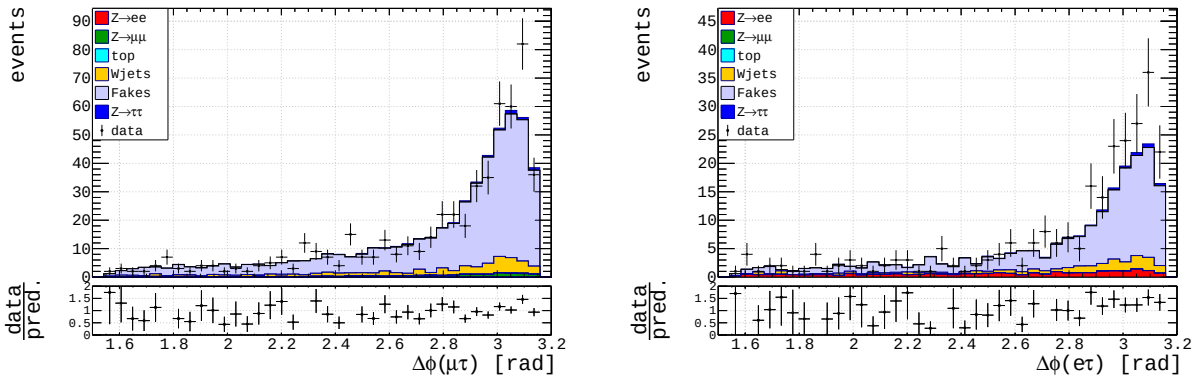

(a) Muon channel *(b)* Electron channel

Figure A.9.: $\Delta\phi(\ell, \tau)$ distribution in the fake estimate validation region (SS). The details are the same as in Figure 8.16.

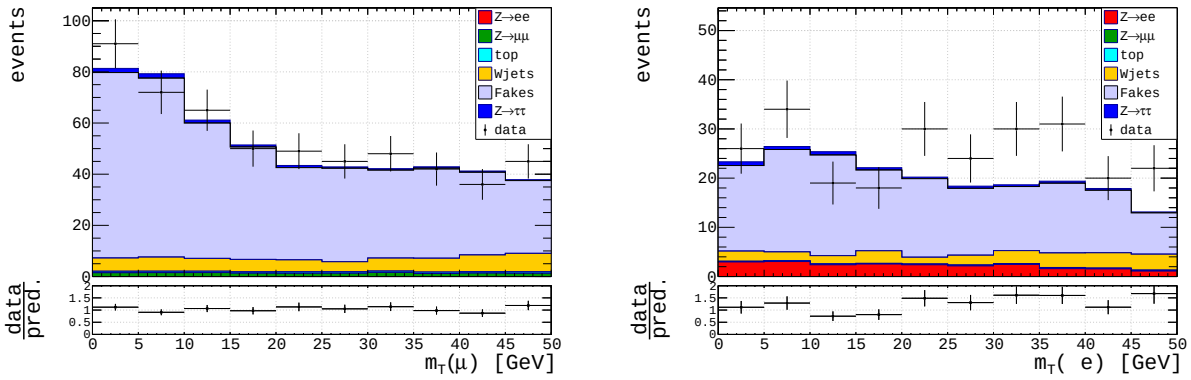

(a) Muon channel *(b)* Electron channel

Figure A.10.: Transverse mass distribution in the fake estimate validation region (SS). The details are the same as in Figure 8.16.

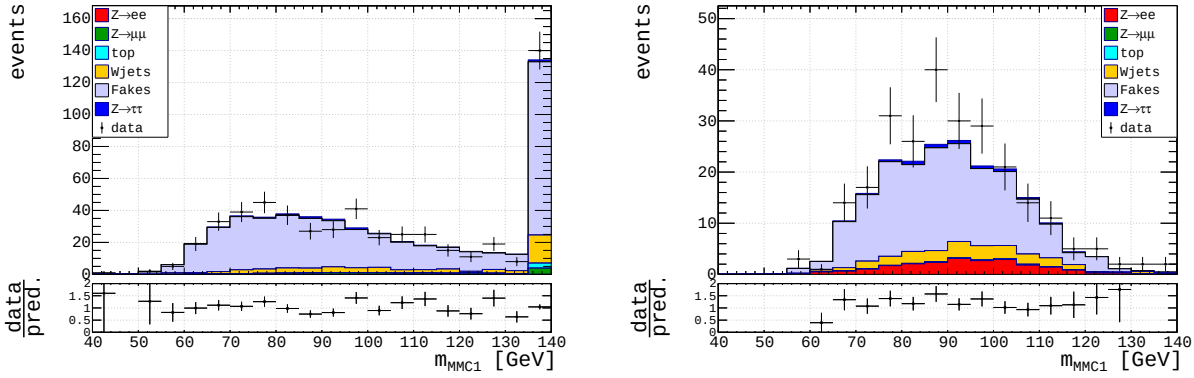

(a) Muon channel *(b)* Electron channel

Figure A.11.: MMC mass distribution in the fake estimate validation region (SS). The details are the same as in Figure 8.16.

B. Tables

Process	Cross section [pb]	k-factor	Filter efficiency
$Z \to \tau\tau$	1901.2	1.026	1.0
$Z \to \mu\mu$	1901.2	1.026	1.0
$Z \to ee$	1901.2	1.026	1.0
$W^- \to e^-\nu$	8282.6	1.0358	1.0
$W^- \to \mu^-\nu$	8282.6	1.0358	1.0
$W^- \to \tau^-\nu$	8282.6	1.0358	1.0
$W^+ \to e^+\nu$	11306	1.0172	1.0
$W^+ \to \mu^+\nu$	11306	1.0172	1.0
$W^+ \to \tau^+\nu$	11306	1.0172	1.0
single top $W\bar{t}$	33.9890	1.0	1.0
single antitop Wt	34.009	1.0	1.0
single top (s-channel)	2.0517	1.0	1.0
single antitop (s-channel)	1.2615	1.0	1.0
single top (t-channel)	43.739	1.0	1.0
single antitop (t-channel)	25.778	1.0	1.0
$t\bar{t}$	696.12	1.1949	0.543

Table B.1.: Cross section and k-factor for the MC background processes. The k-factor scales to NNLO. During the generation of the $t\bar{t}$ sample a lepton filter is applied. The efficiency of such a filter has to be taken into account.

Process	Sample name
$t\bar{t}$	mc15_13TeV.410000.PowhegPythiaEvtGen_P2012_ttbar_hdamp172p5_nonallhad.merge. DAOD_HIGG4D2.e3698_s2608_s2183_r6630_r6264_p2375
single antitop $W\bar{t}$	mc15_13TeV.410014.PowhegPythiaEvtGen_P2012_Wt_inclusive_antitop.merge. DAOD_HIGG4D2.e3753_s2608_s2183_r6630_r6264_p2375
single top Wt	mc15_13TeV.410013.PowhegPythiaEvtGen_P2012_Wt_inclusive_top.merge. DAOD_HIGG4D2.e3753_s2608_s2183_r6630_r6264_p2375
single antitop (t-channel)	mc15_13TeV.410012.PowhegPythiaEvtGen_P2012_singletop_tchan_lept_antitop.merge. DAOD_HIGG4D2.e3824_s2608_s2183_r6630_r6264_p2375
single top (t-channel)	mc15_13TeV.410011.PowhegPythiaEvtGen_P2012_singletop_tchan_lept_top.merge. DAOD_HIGG4D2.e3824_s2608_s2183_r6630_r6264_p2375
single antitop (s-channel)	mc15_13TeV.410026.PowhegPythiaEvtGen_P2012_SingleTopSchan_noAllHad_antitop.merge. DAOD_HIGG4D2.e3998_s2608_s2183_r6630_r6264_p2375
single top (s-channel)	mc15_13TeV.410025.PowhegPythiaEvtGen_P2012_SingleTopSchan_noAllHad_top.merge. DAOD_HIGG4D2.e3998_s2608_s2183_r6630_r6264_p2375
$W^- \to e^-\nu$	mc15_13TeV.361103.PowhegPythia8EvtGen_AZNLOCTEQ6L1_Wminusenu.merge. DAOD_HIGG4D2.e3601_s2576_s2132_r6630_r6264_p2375
$W^- \to \mu^-\nu$	mc15_13TeV.361104.PowhegPythia8EvtGen_AZNLOCTEQ6L1_Wminusmunu.merge. DAOD_HIGG4D2.e3601_s2576_s2132_r6630_r6264_p2375
$W^- \to \tau^-\nu$	mc15_13TeV.361105.PowhegPythia8EvtGen_AZNLOCTEQ6L1_Wminustaunu.merge. DAOD_HIGG4D2.e3601_s2576_s2132_r6630_r6264_p2375
$W^+ \to e^+\nu$	mc15_13TeV.361100.PowhegPythia8EvtGen_AZNLOCTEQ6L1_Wplusenu.merge. DAOD_HIGG4D2.e3601_s2576_s2132_r6630_r6264_p2375
$W^+ \to \mu^+\nu$	mc15_13TeV.361101.PowhegPythia8EvtGen_AZNLOCTEQ6L1_Wplusmunu.merge. DAOD_HIGG4D2.e3601_s2576_s2132_r6630_r6264_p2375
$W^+ \to \tau^+\nu$	mc15_13TeV.361102.PowhegPythia8EvtGen_AZNLOCTEQ6L1_Wplustaunu.merge. DAOD_HIGG4D2.e3601_s2576_s2132_r6630_r6264_p2375
$Z \to ee$	mc15_13TeV.361106.PowhegPythia8EvtGen_AZNLOCTEQ6L1_Zee.merge. DAOD_HIGG4D2.e3601_s2576_s2132_r6630_r6264_p2375
$Z \to \mu\mu$	mc15_13TeV.361107.PowhegPythia8EvtGen_AZNLOCTEQ6L1_Zmumu.merge. DAOD_HIGG4D2.e3601_s2576_s2132_r6630_r6264_p2375
$Z \to \tau\tau$	mc15_13TeV.361108.PowhegPythia8EvtGen_AZNLOCTEQ6L1_Ztautau.merge. DAOD_HIGG4D2.e3601_s2576_s2132_r6630_r6264_p2375

Table B.2.: MC input samples generated with PowHeg and Pythia at $\sqrt{s} = 13\,\text{TeV}$ with 50 ns bunch spacing. The corresponding cross sections and k-factors can be found in Table B.1. For the $t\bar{t}$ and the single top samples the CT10 PDF set [38] and the Perugia2012 tune [45] are used. For the other samples the AZLNO tune [34] and the CTEQ6L1 PDF set [35] are applied.

Bibliography

[1] ATLAS collaboration, *Observation of a new particle in the search for the Standard Model Higgs boson with the ATLAS detector at the LHC*, Phys.Lett. **B716**, 1 (2012)

[2] CMS collaboration, *Observation of a new boson at a mass of 125 GeV with the CMS experiment at the LHC*, Phys.Lett. **B716**, 30 (2012)

[3] ATLAS collaboration, *Evidence for the Higgs-boson Yukawa coupling to tau leptons with the ATLAS detector*, JHEP **04**, 117 (2015)

[4] M. E. Peskin, D. V. Schroeder, *An Introduction to Quantum Field Theory*, Addison-Wesley Publishing Company, Reading (1995)

[5] A. Salam, *Weak and Electromagnetic Interactions*, ed. Nobel Symposium No. 8 (Almqvist & Wiksell, Stockholm, 1968)

[6] P. W. Higgs, *Broken Symmetries, Massless Particles and Gauge Fields*, Phys. Lett. **12**, 132 (1964)

[7] A. Djouadi, *The Anatomy of electro-weak symmetry breaking. I: The Higgs boson in the standard model*, Phys.Rept. **457**, 1 (2008)

[8] C. Adloff, et al. (H1), *Deep inelastic inclusive e p scattering at low x and a determination of* α_s, Eur. Phys. J. **C21**, 33 (2001)

[9] A. Abulencia, et al. (CDF), *Measurement of the Inclusive Jet Cross Section using the* $\boldsymbol{k_T}$ *algorithm in* $\boldsymbol{p\overline{p}}$ *Collisions at* $\boldsymbol{\sqrt{s}}$ *= 1.96 TeV with the CDF II Detector*, Phys. Rev. **D75**, 092006 (2007)

[10] M. L. Perl, et al., *Evidence for Anomalous Lepton Production in* e^+e^- *Annihilation*, Phys. Rev. Lett. **35**, 1489 (1975)

[11] K. Olive, et al. (Particle Data Group), *Review of Particle Physics*, Chin.Phys. **C38**, 090001 (2014)

[12] J. R. Andersen, et al. (LHC Higgs Cross Section Working Group), *Handbook of LHC Higgs Cross Sections: 3. Higgs Properties* (2013), 1307.1347

[13] S. Dittmaier, et al., *Handbook of LHC Higgs Cross Sections: 2. Differential Distributions* (2012), 1201.3084

[14] G. Arnison, et al. (UA1), *Experimental observation of lepton pairs of invariant mass around 95 GeV/c^2 at the CERN SPS Collider*, Phys. Lett. **B126**, 398 (1983)

[15] M. Thomson, *Modern Particle Physics*, Cambridge University Press, 1 edition (2013)

[16] L. Evans, P. Bryant, *LHC Machine*, JINST **3**, S08001 (2008)

[17] ATLAS collaboration, *The ATLAS Experiment at the CERN Large Hadron Collider*, JINST **3**, S08003 (2008)

[18] S. Agostinelli, et al. (GEANT4), *GEANT4: A Simulation toolkit*, Nucl.Instrum.Meth. **A506**, 250 (2003)

[19] T. Sjostrand, S. Mrenna, P. Z. Skands, *PYTHIA 6.4 Physics and Manual*, JHEP **05**, 026 (2006)

[20] T. Sjostrand, S. Mrenna, P. Z. Skands, *A Brief Introduction to PYTHIA 8.1*, Comput. Phys. Commun. **178**, 852 (2008)

[21] S. Frixione, P. Nason, C. Oleari, *Matching NLO QCD computations with Parton Shower simulations: the POWHEG method*, JHEP **11**, 070 (2007)

[22] M. Cacciari, G. P. Salam, G. Soyez, *The Anti-k(t) jet clustering algorithm*, JHEP **0804**, 063 (2008)

[23] ATLAS collaboration, *Jet energy measurement and its systematic uncertainty in proton-proton collisions at $\sqrt{s} = 7$ TeV with the ATLAS detector*, Eur. Phys. J. **C75**, 17 (2015)

[24] ATLAS Collaboration, *Jet Calibration and Systematic Uncertainties for Jets Reconstructed in the ATLAS Detector at $\sqrt{s} = 13$ TeV*, ATL-PHYS-PUB-2015-015 (2015)

[25] ATLAS collaboration, *Electron reconstruction and identification efficiency measurements with the ATLAS detector using the 2011 LHC proton-proton collision data*, Eur.Phys.J. **C74(7)**, 2941 (2014)

[26] ATLAS Collaboration, *Electron efficiency measurements with the ATLAS detector using the 2012 LHC proton-proton collision data*, ATLAS-CONF-2014-032 (2014)

[27] ATLAS collaboration, *Measurement of the muon reconstruction performance of the ATLAS detector using 2011 and 2012 LHC proton-proton collision data*, Eur.Phys.J. **C74(11)**, 3130 (2014)

[28] ATLAS Collaboration, *Muon reconstruction performance in early* $\sqrt{s} = 13$ *TeV data*, ATL-PHYS-PUB-2015-037 (2015)

[29] ATLAS collaboration, *Identification and energy calibration of hadronically decaying tau leptons with the ATLAS experiment in pp collisions at* $\sqrt{s}$*=8 TeV* (2014), 1412.7086

[30] D. Duschinger, et al., *Reconstruction, Energy Calibration, and Identification of Hadronically Decaying Tau Leptons in the ATLAS Experiment for Run 2 of the LHC*, ATL-COM-PHYS-2015-927 (2015)

[31] P. Bechtle, et al., *Reconstruction of hadronic decay products of tau leptons with the ATLAS experiment*, ATL-COM-PHYS-2015-214 (2015)

[32] T. J. Khoo, et al., *Reconstruction and Performance of Missing Transverse Momentum in the ATLAS Detector using Proton-Proton Collisions at* $\sqrt{s} = 8$ *TeV*, ATL-COM-PHYS-2015-341 (2015)

[33] A. Elagin, et al., *A new mass reconstruction technique for resonances decaying to di-tau*, Nucl.Instrum.Meth. **A654**, 481 (2011)

[34] ATLAS collaboration, *Measurement of the* Z/γ^* *boson transverse momentum distribution in pp collisions at* $\sqrt{s} = 7$ *TeV with the ATLAS detector*, JHEP **09**, 145 (2014)

[35] J. Pumplin, et al., *New generation of parton distributions with uncertainties from global QCD analysis*, JHEP **07**, 012 (2002)

[36] S. Jadach, et al., *The tau decay library TAUOLA: Version 2.4*, Comput.Phys.Commun. **76**, 361 (1993)

[37] D. W. Stroock, *An Introduction to Markov Processes (Graduate Texts in Mathematics)*, Springer, Berlin (2013)

[38] M. Guzzi, et al., *CT10 parton distributions and other developments in the global QCD analysis* (2011), 1101.0561

[39] (20.09.2015), URL https://twiki.cern.ch/twiki/bin/view/AtlasPublic/LuminosityPublicResultsRun2

[40] ATLAS collaboration, *Improved luminosity determination in pp collisions at* $\sqrt{s} = 7$ *TeV using the ATLAS detector at the LHC*, Eur. Phys. J. **C73(8)**, 2518 (2013)

[41] ATLAS collaboration, *Measurement of W and Z Boson Production Cross Sections in pp Collisions at* $\sqrt{s} = 13$ *TeV in the ATLAS Detector*, ATLAS-CONF-2015-039 (2015)

[42] O. Behnke, et al., *Data Analysis in High Energy Physics: A Practical Guide to Statistical Methods*, Wiley-VCH, Weinheim (2013)

[43] ATLAS collaboration, *Measurement of the inclusive* $W^{\pm}$ *and Z/gamma cross sections in the electron and muon decay channels in pp collisions at* $\sqrt{s} = 7$ *TeV with the ATLAS detector*, Phys. Rev. **D85**, 072004 (2012)

[44] CMS collaboration, *Measurement of inclusive W and Z boson production cross sections in pp collisions at* $\sqrt{s} = 8$ *TeV*, Phys. Rev. Lett. **112**, 191802 (2014)

[45] P. Z. Skands, *Tuning Monte Carlo Generators: The Perugia Tunes*, Phys. Rev. **D82**, 074018 (2010)

Acknowledgement

First of all, I want to thank Prof. Dr. Arnulf Quadt for the unique opportunity to write this thesis in his working group. Moreover, I want to thank him for his professional supervision.
Secondly, I thank Ulla Blumenschein and Zinonas Zinonos for the daily supervision. You answered almost infinitely many questions and provided a very friendly working atmosphere.
For the many useful comments on this thesis I owe thanks to Ulla Blumenschein, Zinonas Zinonos, Michel Janus and Antonio de Maria.
I also want to thank my second referee Prof. Dr. Stan Lai and Michel Janus for their advices as well as Zinonas Zinonos and Eric Drechsler for maintaining an awesome analysis framework.
Mein besonderer Dank gilt meiner Familie für die aufbauenden und bestärkenden Gespräche.

Erklärung nach §17(9) der Prüfungsordnung für den Bachelor-Studiengang Physik und den Master-Studiengang Physik an der Universität Göttingen:

Hiermit erkläre ich, dass ich diese Abschlussarbeit selbständig verfasst habe, keine anderen als die angegebenen Quellen und Hilfsmittel benutzt habe und alle Stellen, die wörtlich oder sinngemäß aus veröffentlichten Schriften entnommen wurden, als solche kenntlich gemacht habe.
Darüberhinaus erkläre ich, dass diese Abschlussarbeit nicht, auch nicht auszugsweise, im Rahmen einer nichtbestandenen Prüfung an dieser oder einer anderen Hochschule eingereicht wurde.

Göttingen, den 29. September 2015

(Lukas Weise)